Flexible pH Sensors based on Electrodeposited Iridium Oxide

Paul Marsh

A thesis

submitted in partial fulfillment of the

requirements of the degree of

Master of Science in Electrical Engineering

University of Washington
2018

Committee:

Hung Cao, Chair

Tadesse Ghirmai

Seungkeun Choi

Program Authorized to Offer Degree:

Electrical Engineering

University of Washington

Abstract

Flexible pH Sensors based on Electrodeposited Iridium Oxide

Paul Marsh

Chair of the Supervisory Committee:
Dr. Hung Cao
Department of Electrical Engineering

Due to mounting global water scarcity and source contamination concerns, significant water monitoring efforts are required, though current data suggests significant gaps in monitoring coverage and a lack of cost effective and versatile sensing devices. A complete system is proposed and demonstrated herein which monitors a water quality indicator of high importance, solution pH. Therefore, this system is also suitable for biomedical applications with minor modifications, thus it was designed and tested with both in mind. The sensors possess high pH sensitivity and stability of iridium oxide (IrOx) with the efficiency of electrodeposition and conformability and biocompatibility of polyimide substrates; additionally, the device was designed to communicate wirelessly and make use of both Bluetooth-Low-Energy (BLE) transmission and frequency-based load modulation (FM) transmission with wireless power transfer (WPT) via inductive coupling.

The probes were fabricated by traditional lithography and a cyclic voltammetry method using an Iridium-based, oxalate-containing solution. The IrOx film and surface characterization was performed by voltammogram investigation, scanning electron microscopy (SEM), profilometry, electron dispersive x-ray spectroscopy (EDS/EDX), x-ray photoelectron

spectroscopy (XPS), and optical and laser microscopy. Reference electrodes were fabricated by application of silver chloride (AgCl) ink. Gold (Au), copper (Cu), and silver (Ag) substrates were evaluated, Cu being discarded as a viable substrate.

Probe performance was characterized in terms of pH sensitivity, sensitivity with respect to surface area, linearity, response time, lower limit of detection, cationic selectivity, and response to mechanical stress. Some attempts were made to programmatically and electrically reduce noise and programmatically characterize experimental results via Matlab (*Mathworks, MA*).

Applicability is demonstrated by both a review of previous packaging work and current wireless schemes. Wireless schemes based around amplitude modulation (AM), frequency modulation (FM), and Bluetooth communication are demonstrated. FM communication associated with WPT was demonstrated as the most appropriate for the widest variety of applications.

Finally, future work is discussed in terms of a completed patch design, possible surface material modifications, packaging improvements, and monitoring vehicle concepts.

Acknowledgements

Part of this work was funded under National Science Foundation CAREER Award #1652818 under Dr. Hung Cao.

Part of this work was conducted at the Molecular Analysis Facility, a National Nanotechnology Coordinated Infrastructure site at the University of Washington which is supported in part by the National Science Foundation (grant ECC-1542101), the University of Washington, the Molecular Engineering & Sciences Institute, the Clean Energy Institute, and the National Institutes of Health.

Part of this work was conducted at the Washington Nanofabrication Facility / Molecular Analysis Facility, a National Nanotechnology Coordinated Infrastructure (NNCI) site at the University of Washington, which is supported in part by funds from the Molecular Engineering & Sciences Institute, the Clean Energy Institute, the Washington Research Foundation, the M. J. Murdock Charitable Trust, the National Science Foundation and the National Institutes of Health.

Dedication

While this work may not represent an inflection point in the science of pH sensing, it does represent the culmination of worked produced by a myriad of contributions from a myriad of people.

First I want to thank the staff at the Molecular Analysis Facility, specifically Scott Braswell, Dr. Micah Glaz, and Gerry Hammer, and staff at the Washington Nanofabrication Facility, specifically Dr. Darick Baker, Mark Brunson, and Dr. Michael Khbeis; all of you gave freely of your knowledge and tremendously improved my processes.

I need to thank a multitude of classmates and work partners: Peter Ritchie for creating the original AM scheme and planar antennas (not to mention answering all of my fabrication emails), Miguel Huerta for non-stop iterations of the FM scheme in both breadboard and protoboard, Victor Ho for getting our fabrication started and answering my analog design questions, Tai Le for being an all-around troubleshooting expert, Wyatt Moore for starting parylene and silicon fabrication, Mark Clucas and Ly Huynh for diligently testing and retesting probes, Lillian Thiel for deposition parameter investigations, Daniel Schossow for coming up with very useful fabrication tricks, and Houssem Eddine Amor for allowing me to participate in his LTCC research and being my first knowledge source on IrOx probes and fabrication. Thank you to Dr. Soyeon Yi for various publication support. Thank you to Xuesong Yang and Dr. J.-C. Chiao at University of Texas at Arlington for providing background and oscillator schemes and conducting selectivity tests. Thank you to Dr. Libu Manjakkal and Dr. Ravinder Dahiya for providing experimental feedback and bio-equivalency information.

I'd like to thank the University of Washington Bothell for providing me with lab space and technical and administrative support in the form of the School of STEM, Dr. Kyoung-Tae Kim, and Sharon Meriwether (my "it's school related" go-to person). Thank you to my advisory committee, Drs. Seungkeun Choi and Tadesse Ghirmai; your technical advice is consistently valuable.

Although not directly part of this work, I would be remiss if I did not mention the members of the LIGO Scientific Collaboration I dealt with and the staff at LIGO – Hanford Observatory that I worked with. Specifically, Drs. Joey Key and Rick Savage for providing me a rare and fantastic research experience, and Dr. Jeff Kissel for being tireless both in his supply of knowledge and enthusiasm and his vouching for a person whom he could only evaluate via the volume of his emails. Though there aren't optical resonators or neutron stars anywhere in these pages, this and future publications certainly do and will feature the dedication to knowledge and thrill of discovery I've been given.

To Dr. Cao, thank you for several years of teaching, patience, professional guidance, more patience, and many other things. I believe I'm finally starting to learn that, like Shakespeare said, "things won are done, joy's soul lies in the doing."

To my mother and father, for teaching me that quality and effort have no upper limits if in the service of others.

To Lauren: some couple of years, huh? Good thing we have so many more.

Contents

1. Introduction and Background

1.1 Motivations

Both water pollution and water scarcity have become major issues in the modern world; examples abound of the former. Minamata Disease was first discovered in Minamata city, Japan, in 1956. It was caused by the release of Methylmercury in industrial wastewater from the Chisso Corporation's chemical factory, which continued from 1932 to 1968. The long term effect was a fundamental altering of gene formation in humans and animals living near the facility [16]. In 2014, the drinking water in Flint, Michigan, was strongly contaminated when Lead from aging pipes was leached into the water supply, causing extremely elevated levels of the heavy metal neurotoxin. Some city residents were converted to a 100% supply of bottled water and disallowed from showering [4]. In 2015, thousands of tons of fish were found dead in a coastal area in central Vietnam; the contamination source was found to be Formosa, a Taiwanese steel plant, who released chemical waste directly into the sea [14].

Examples of the former are no less available. Cycles of drought in California basins have caused residents in the San Joaquin valley to resort to groundwater pumping which, in turn, has possibly caused a permanent loss of total groundwater storage of about 5% in just 3 years [17].

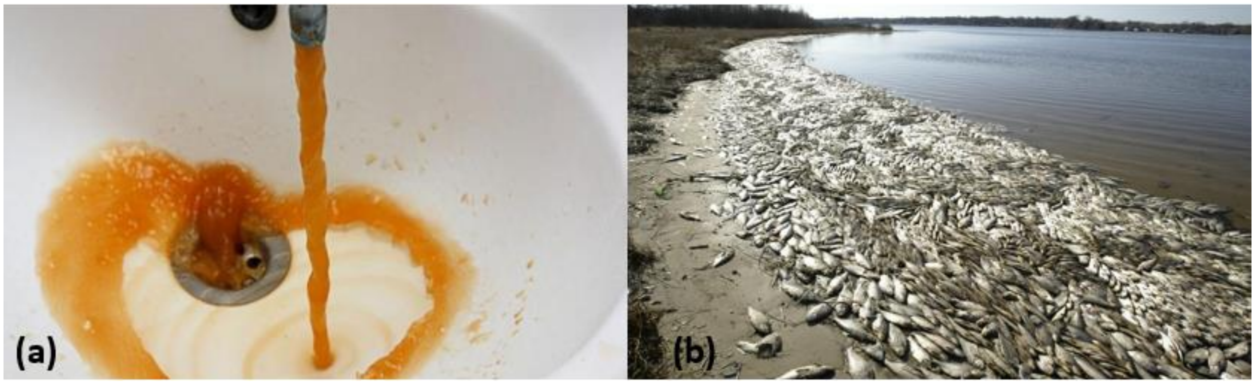

Figure 1- (a) Pb contaminated drinking water in Flint, MI [4] (b) Fish die-off near Formosa plant [14].

The South African city of Cape Town is rapidly approaching the day its residents will need to survive on 25 liters of water per day, which is equivalent to a 4-minute shower [18]. Some recent studies indicate that water scarcity isn’t resolved, but simply pushed downstream, by human intervention [19].

These enumerate only a few events out of the multitudes of severe water pollution and scarcity events which have begun to plague humans globally. In 2016, the World Bank released a statement noting there will be a 40% global shortfall between demand and supply of water by 2030. They noted that this shortfall will disproportionately affect ~1 billion low-income people susceptible to source contamination [20]. It is clear that the monitoring of drinking water will require significant innovation and investment in the near future.

Producers of sensing equipment are certainly paying attention to these trends. Global Industry Analysts Inc. reported that the water instrumentation market will expand to $3.6B by 2020 [21]. Governments are also, though are sometimes resource limited in the research that they can do. Of the $8.6B the Environmental Protection Agency (EPA) had requested from congress for FY2016, $2.3B was budgeted for Clean Water Act funds. Despite this, and the EPA’s explicit budget proposal priority towards water quality, they stated that “America’s waters remain imperiled” [22]. Even with this funding level, the agency continues to leverage 350+ volunteer groups across the U.S., which run multiple water quality research projects per group [23].

This is mainly because, despite these significant funds and efforts, sensing across water systems remain far from ubiquitous. The United States Geographic Survey (USGS) maintains a joint-department database with the EPA which contains multiple water quality parameters taken at various intervals across approximately 415,000 US lake sites [24]. However, recent estimates show that the contiguous US alone may contain over 5.8 million lakes and 1.8 million kilometers of lake shoreline [25]. Active water monitoring parameters and schedules vary by location, as well; in the area around the University of Washington, large lakes such as Lake Washington have continuous “temperature, pH, oxygen, conductivity, chlorophyll-a, and turbidity readings throughout the water column” [26] but smaller lakes see much less attention. Another local lake, Cottage Lake, saw a six year monitoring gap which the county admits made a Phosphorous reduction effort “difficult to verify” [27].

A portion of the blame here lies with monitoring hardware, as the equipment used to do this monitoring is far from inexpensive. A typical water sonde from a leading manufacturer can be in the tens of thousands of dollars, if fitted with only a few sensors. The sensors themselves can be $1,000 or more per unit. Laboratory testing is also quite expensive and can take days or weeks to get results.

To that end, this research takes aim at a single sensor among the many that are required in a holistic water sampling plan: that of the pH sensor. The target, pH, or the measure of the acidity or alkalinity of a liquid, technically defined as the measure of hydrogen ion activity, is a useful metric in water quality for a number of reasons. Drinking water is regulated within the range of 6.5 – 8.5 [28] to avoid adverse health effects in humans. Freshwater fish begin to see gill damage and reproductive failure outside of the pH 5.5 – 10.5 range [29]. Swings in pH can even affect transport rates in soil of pollutants like lead (Pb), zinc (Zn), and nickel (Ni) [13].

Measurement of pH also holds considerable usefulness in biological systems. Aside from the fish biology as described above, pH also plays an important role in plant, cellular, and human biology. It has been found for example, that soybean yields are highest when soil liquid pH is in the 4.5 – 5.5 range [30]. Cellular pH can affect everything from the rate of toxin penetration [31] to culture growth efficiency [32]. In humans, pH levels have a role in almost every process in our

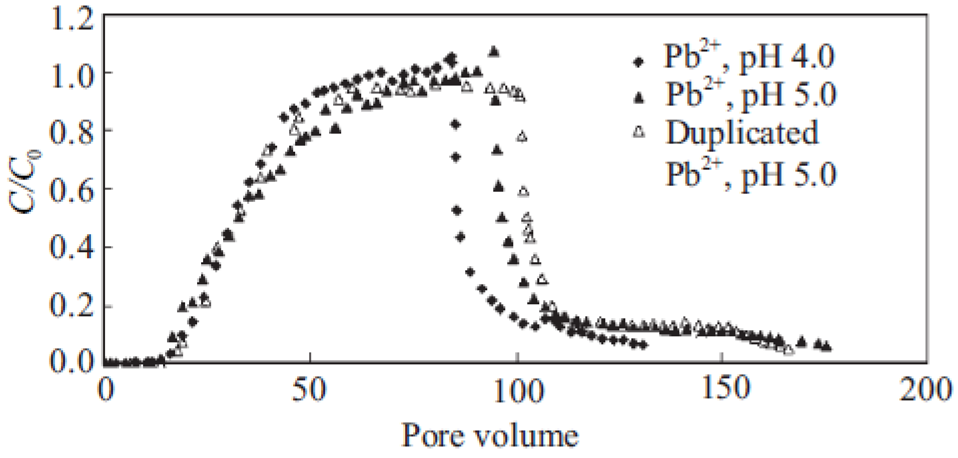

Figure 2- Lead transport rates in soil with varying liquid pH levels. Both concentration (C) and volume are shown as being relative to their initial values (C_0 and V_0, respectively). Note the marked change in pore size (i.e. transport path size) at all concentration levels with a pH change of just 1.0 [13].

bodies.

Therefore, it behooves us to attempt to build systems which can be scaled for, and used in, a wide range of applications.

1.2 Background and Proposed Device

Measurement of this factor is by no means a new idea, having been around for about 100 years [33]. These devices typically come in the form of hydron-active metals which receive ions through permeable membranes; measurement is potentiometric, and will be discussed at length later on. A solution’s pH has been measured with a myriad of methods, from paper indicating strips to laboratory titrations to the electroactive probes mentioned previously. These electroactive probes have seen widespread use because they can be reused, they can be connected to analog electronics, and their measurement rates are dictated only by their response rate and the logging rate of associated hardware. Research variants of these probes range from monolithic materials sensitive to hydrons to microelectrode arrays with various surface modifications. The most prominent type of pH meter, commercially, typically utilizes a silver (Ag) wire in chlorine-based solution and sits behind a glass encapsulating layer; it has seen extensive use over the years due to highly precise and reliable behavior. However, their integration in modern systems is typically limited by their large size and lack of conformability [5].

This thesis attempts to fills a gap in the aforementioned dearth of water sampling due to hardware expense and form factor, along with leaving room for biological and medical applications, by producing a pH monitoring device which features confirmability to various environments, is inexpensive and simple manufacture, and provides for several connectivity options, including remote communication. To that end, this thesis demonstrates proofs of concept of a wirelessly powered and communicating pH sensor, fabricated on flexible substrates, and produced with efficient and low energy deposition methods.

Beginning at the sensor level, the pH sensor itself is a hydron-active metal oxide. Since the 1980's, various thin film metal oxides for sensing pH have been widely employed. A number of literature reviews have reported IrO_2 and RuO_2 to be the most promising candidates, in terms of sensitivity and stability [34]. Iridium oxide (IrOx) has been particularly of interest, owing to its wide-ranging inertness and stability [34, 35], and is studied here. The sensing mechanism of IrOx in the presence of hydrons is assumed to be the formation of capacitive double layers around the intercalated (adsorbed) solid oxide phase near the solution interface [34]. Several authors believe this intercalation to affect the stoichiometry of the solid phase metal oxide, releasing further protons and allowing potentials higher than Nernstian theory predicts [36, 37], which will be discussed in greater detail in further categories.

Various manufacturing methodologies have been attempted by the academic community, such as thermal oxidation [37], sputtering [38], sol-gel deposition [6], and anodic electrodeposition

[39], all with differing levels of probe sensitivity and stability. Melt oxidization of IrOx was conducted by Yao et al. to obtain thick films and obtain reliable sensitivity values, which they state are not commonly achieved with other methods; when combined with Lithium Carbonate, the authors were able to achieve 58.9 mV/pH and ~0.1 mV/day drift, though the devices required the energy intensive step of having to be held at 870° C for 5 hours. Sputtering is another common method of producing research electrodes; Kreider and colleagues have produced electrodes this way, though sensitivities are typically at or below Nernstian (Kreider *et al.* achieved 54 mV/pH) and require expensive sputtering hardware and targets [40]. Sol-gel deposition, wherein a substrate is dipped into solution and cured, has received more attention recently due to it improved application onto flexible substrates, though the process has always shown promise in terms of manufacturing simplicity. Initially, Nishio *et al.* demonstrated sol-gel IrOx thin film construction on solid substrates [41], though Huang *et. al.* published several works exploring and using sol-gel deposition to place IrOx thin films on flexible substrates [1, 6, 42]. That group produced electrodes repeatedly within the ~52 mV/pH range. Anodic electrodeposition in Ir containing solutions requires highly stable power control systems but can produce electrodes quickly and at room temperature, and has produced recent sensitivities in the 78-82 mV/pH range [36, 43].

In this work, the research attempted to optimize the anodic electrodeposition method of manufacturing on top of a biomedically and environmentally relevant (i.e. biocompatible and flexible) substrate: Kapton (*DuPont, Omaha, NE*) polyimide. In this way, the scalable manufacturing and high sensitivity of the electrodeposition method is combined with the wide applicability of the biocompatible/flexible substrate. It will later be demonstrated that super-Nernstian sensitivity behavior and limit-of-detection (LOD) comparable to previous anodic electrodeposition work can be had for a fraction of typical deposition lengths, that simple paste-based reference electrodes can be fabricated easily and feature long-term stability, and that gold currently appears to be the best deposition base layer of typically available metals.

Beyond the sensor, a potentiometric measuring circuit was created to source the potential generated between the metal oxide layer and a reference electrode. This circuit was quite simple, only delivering a regulated voltage to the reference electrode to offset negative potentials, and a high impedance buffer to read the sensor's potential without allowing current to flow and redox processes to take place on the electrode surface. This will be included in the instrumentation section.

Finally, wireless power and communication systems were experimented with and are demonstrated. Wireless power transfer (WPT) was achieved using planar coil antennas, and communication was demonstrated via both oscillation-based load modulation and Bluetooth digital communication.

2. Materials Characterization

This section will discuss the physical layout of the probe (both working and reference sides), the manufacturing process for it, the performance and analysis of said materials, and some difficulties encountered along the way.

2.1 Base Fabrication

The typical fabrication process takes place as seen in Figure 3, and has remained largely unchanged since earlier work [5] and [8]. The typical end result will be a polyimide / Chromium (Cr) / Gold (Au) or Copper (Cu) / Iridium Oxide (IrOx) stack, typically in a square configuration

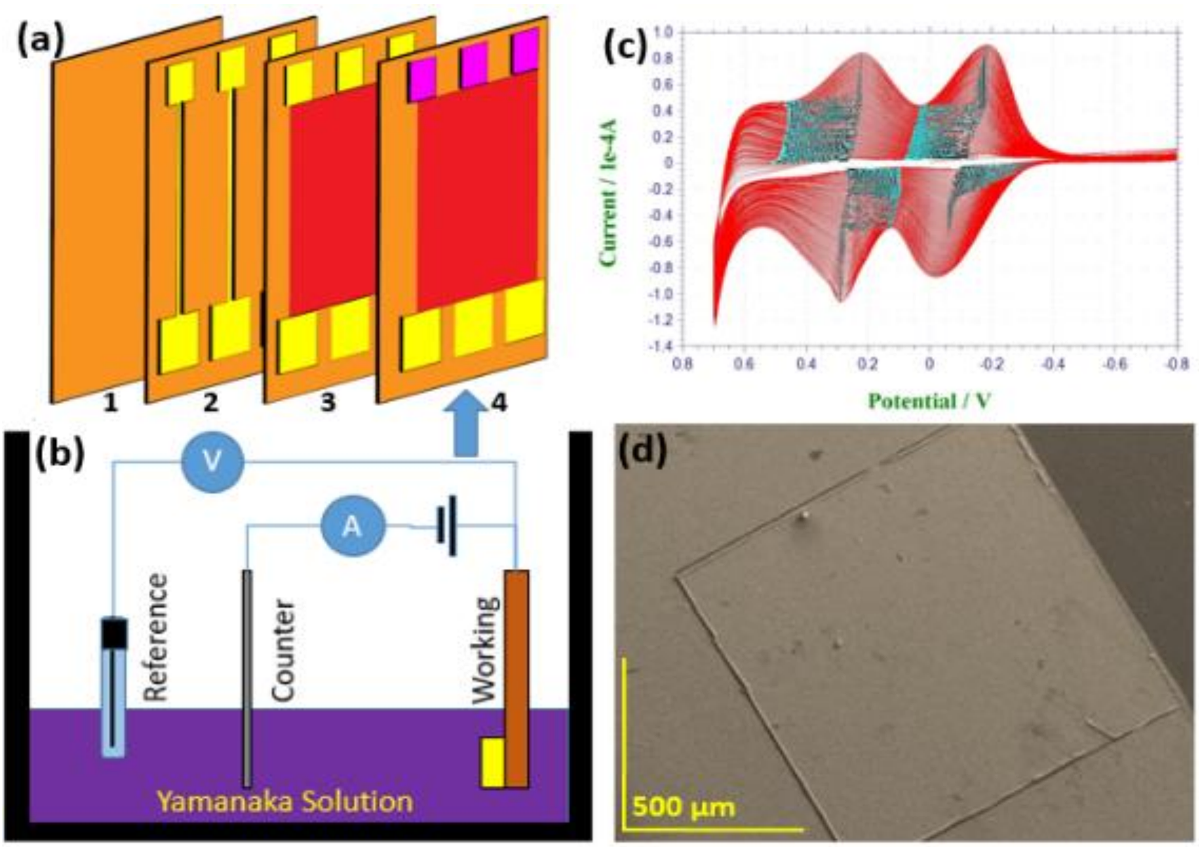

Figure 3- Fabrication process. (a) 3 stages of the lithography process, followed by IrOx deposition; 1- bare polyimide, 2- etched Au/Cr post lithography, 3- S1813 cover, 4- IrOx electrodeposited onto Au. (b) IrOx 3-electrode electrodeposition cell used to create (a)-4. (c) Typical 1 mm^2 deposition cycle, 200 sweeps at 100 mV/s. (d) SEM image showing raised edge of deposited IrOx. Figure parts (b), (c) from [8].

of 1 mm × 1 mm edge lengths. However, multiple sizes, shapes, substrates, and conductive layers were experimented with and will be discussed.

Prior to fabrication, mask designs were prepared using DipTrace software (*Novarm Ltd, Dniepropetrovsk, Ukraine*) and printed on laminated sheets by CAD/Art Services, Inc. (*Bandon, OR*). Two masks were prepared: one featuring the base probe layers in four different sizes (1 mm^2 exposed pad, 500 µm^2, 300 µm^2, and 200 µm^2), and one specifically for photoresist covering of the probe traces (in order to repeatably control the surface area of the electrodes). These masks are shown in Figure 4.

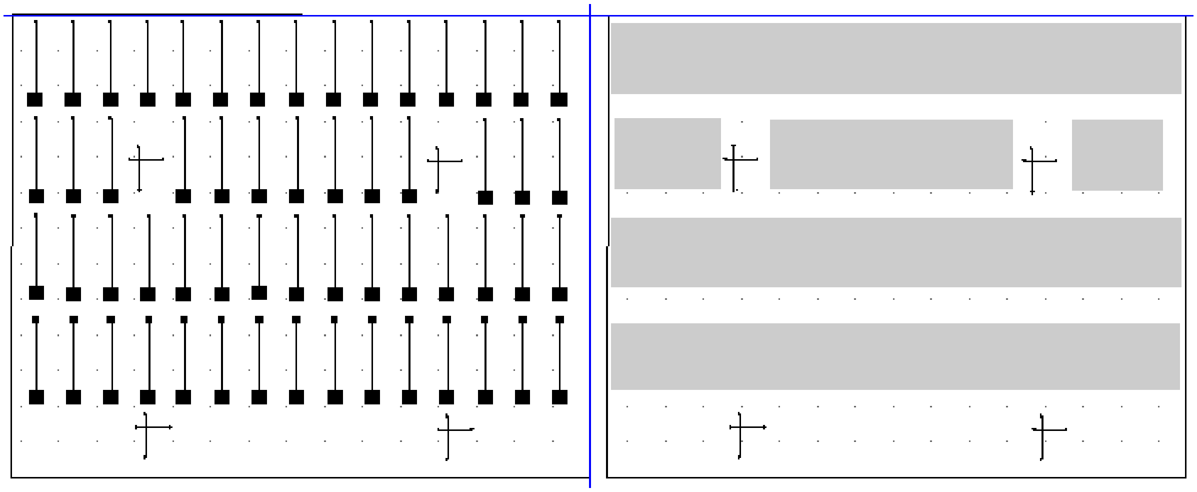

Figure 4- masks used to fabricate probes. Left - contact metallic mask, Right – protective photoresist layer mask.

Following receipt of masks, base layers for lithography were fabricated. First, a sample of 127 µm-thick polyimide film (*Kapton, DuPont, Omaha, NE*) was cleaned and dried via desiccant case and circulating oven before sputtering on a double layer of metallic substrate (Figure 3, (a), 1). Depending on the experiment, either double layers of Gold (Au) and Chromium (Cr) (~200 nm/20 nm) or Copper (Cu) and Cr (~200 nm/20 nm) were sputtered with an ion sputtering system (*Kurt J. Lesker Co., Jefferson Hills, PA*); high purity targets were used from the same manufacturer. Chromium was sputtered beneath the active layer to function as an adhesive layer to the polyimide. Interestingly, differing sputtering parameters and machines will produce altogether different morphologies of sputtered material on the nanoscale, as in Figure 5.

Next, the probes were patterned via photolithography and etched in the following order: first, a layer of photoresist (*Microposit S1813, Microchem, Seattle, WA*) was spin-coated at 3000 RPM for 30 seconds over the metallic base layers. After a 3 minute bake at 90° C, the photoresist was exposed, through the first mask (probe contact patterning), under ~14 mW/cm^2 UV light for

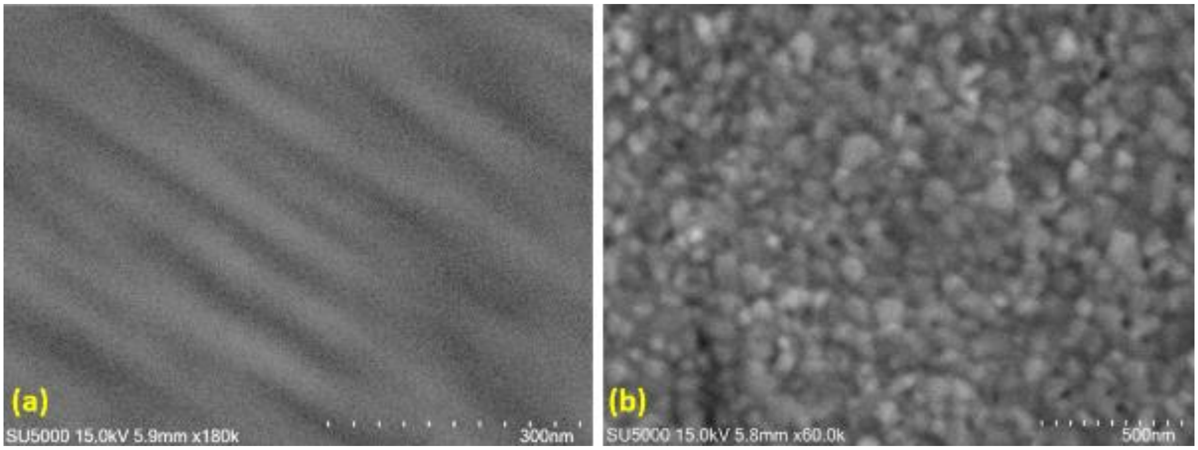

Figure 5- Nanoscale topography differences between sputtering machines and parameters. (a) Evatec plasma sputtering at the Washington Nanofabrication Facility; Cr deposited in 0.5 mTorr of Argon at 2 kW excitation, Au deposited in 5 mTorr of Argon at 1 kW excitation. Sample rotation was cylindrical. (b) Kurt J. Lesker plasma sputtering at University of Washington Bothell; both Cr and Au deposited in 5 mTorr of Argon at 100 W excitation. Sample rotation was planar. Target sizes and chamber volumes differ.

approximately 7 seconds. Following a post-bake of 90° C for 1 minute, the patterned photoresist was developed (*Microposit MF-319, Microchem, Seattle, WA*) and given a DI water rinse. With the probe patterns now exposed, they could be etched using Au/Cu/Cr etchants (#651818, *Sigma-Aldrich, St. Louis, MO* and #44583 / #44582LV, *Alfa Aesar, Haverhill, MA*, respectively), etching first the top layer and then the Cr layer (Figure 3, (a), 2). Then the film thicknesses and roughness were checked using a profilometer to ensure desired parameters. The isotropy of the etching process may also be affected by the aforementioned topography differences, as evidenced by Figure 6; while some of the 50 μm trace's width may be lost by printing imperfections and diffraction around the ink of the mask transparency, some further microns of width are almost assuredly being etched away. Crystallography of the sputtered layers has not been investigated but it is likely centered to some degree on the relatively small material source that the sputtering target represents.

After another round of photoresist spin-coating, a second mask was aligned and used to

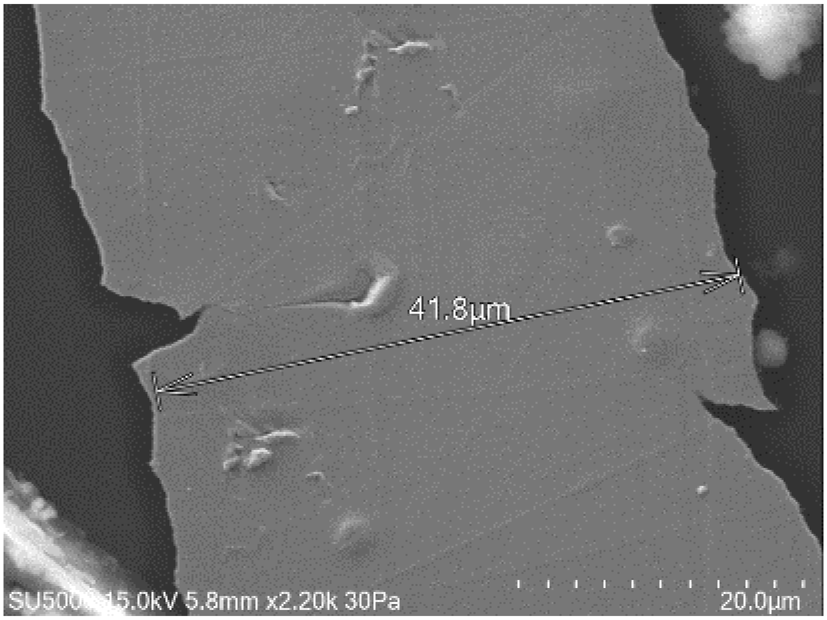

Figure 6- Au trace width of Evatec-sputtered sample after Au etching portion of lithography process.

expose covers for the probe traces. Developing this layer created an insulation layer of photoresist to leave only the electrode areas and contact pads exposed. The entire sample was baked at 90°C for 5 minutes to secure the insulation layer (Figure 3, (a), 3). Cu wires were attached using conductive epoxies which could be cured at low temperature. After probe rows were trimmed into individual probes, leads were trimmed from Cu wires and attached using Ag epoxy (#8331, *MG Chemicals, Surrey, BC, Canada*), they were cured at 70°C for 20 minutes; alternatively, the Ag epoxy could be cured for 24 hours at room temperature.

Once the base Au electrode was created, electrodeposition could take place. In brief, Figure 3 (c) shows the deposition current output shown from a single 1 mm^2 Au working electrode being coated for ~50 minutes; the increasing output current indicated IrOx film thickness growth until the current density reached its peak in the range of 85-120 mA/mm^2. A completed probe is shown in Figure 3, (d).

2.2 Electrodeposition

As mentioned previously, manufacturing methodologies such as thermal oxidation [37], sputtering [38], sol-gel deposition [6], and anodic electrodeposition [39] have been investigated and anodic electrodeposition was chosen for its efficiency and high quality output. For this reason, this thesis focused mainly on the novel combination of flexible substrates and electrodeposition.

A potentiostat (Model 700E, *CH Instruments, Austin*, *TX*) was used to form IrOx film onto the Au base electrodes using electrodeposition by cyclic voltammetry (CV) (Figure 3 (a), 4). For electrodeposition, a standard three-electrode cell was used (Figure 3 (b)). A commercial Ag/AgCl reference electrode (RE) (MW-2021, *Bioanalytical Systems Inc, West Lafayette, IN*) and Platinum (Pt) wire counter electrode (CE) (MW-4130, *Bioanalytical Systems Inc, West Lafayette*, *IN*) were deployed to perform the CV process. Cell potential was varied between the working electrode (WE), i.e. the probes, and the CE; this change caused current to pass between them, thus initiating the iridium redox processes (Figure 3, (c)).

The probes to be plated were placed in “Yamanaka solution,” named after a Japanese physicist who came up with the solution in development of electrochromic displays [39]. The IrOx coating solution was mixed in a simple four-step process as described in [39, 44]. First, 0.07 g of anhydrous IrCl4 (#334480, Sigma-Aldrich, St. Louis, MO) was stirred into 50 ml of water for 30 minutes. Next, 0.5 ml of aqueous 30% hydrogen peroxide (#H323-500, *Fisher Scientific, Hampton*, *NH*) was stirred into solution for 10 minutes. Following that, 250 mg of oxalic acid dehydrate (*Caledon Laboratories Ltd., Georgetown, ON, Canada*) was stirred into the solution for another 10 minutes. Finally, potassium carbonate (#P4379, *Sigma-Aldrich, St. Louis, MO*) was added to adjust the solution pH to 10.5 before resting it for 4 days.

Each chemical in this mixed serves a specific purpose. The iridium tetrachloride is the most important ingredient, supplying the Ir to be formed into ligands and later oxides; the oxalic acid serves to stabilize the Ir-containing complexes which will be formed [12], the hydrogen peroxide supplies the oxygen necessary in several stages of the reaction, and the potassium carbonate is used to set the pH level of the bath. This pH level is a key factor in deposition efficiency [39].

Elsen *et al.* stated that the currently understood mechanism of the formation of the stable oxide form, IrO_2, is that of the oxalate ligand's C-C bond being oxidized (water coordinated to Ir(IV)); a byproduct of this would be CO_2 [12], though it was beyond the scope of this work to confirm that. That group goes further to state that the solid form creation, then, comes from "formation of oxy and hydroxy bridges between iridium complexes, resulting in a loose polymeric network that precipitates at the electrode." They have shown that different solution types and voltammetric methods produce almost no change in sensitivity; therefore, this solution could be swapped for another if deposition parameters were updated.

Hu et al delved deeply into the physical processes occurring during deposition. In their work, they show that the various "activation peaks" observed during voltammetric swings

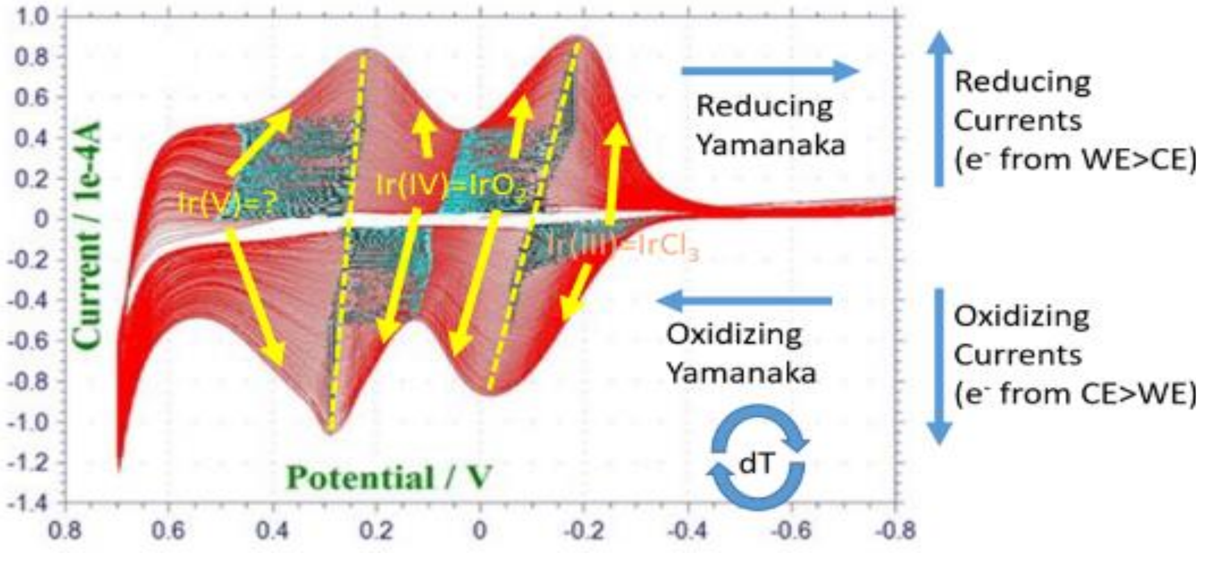

Figure 7- Reaction chain during Ir solution electrodeposition.

correspond to different redox species of iridium being formed. For example, the negative current peak seen between -0.1V and -0.2V vs a silver chloride (AgCl) reference indicate the Ir-Cl complex being oxidized into IrO_2. The oxidation and reduction current peaks are roughly symmetric because the film bulk is reversibly reduced and oxidized during each cycle [44].

From this and other work, then, the output of the cyclic voltammetry process, known as a voltammogram, presents a reaction chain as demonstrated in Figure 7. In the figure, Ir(V) is listed as an unknown because it is unclear what complex is formed at that redox potential; most stable forms of Ir at that redox potential involve elements not present in Yamanaka solution. Regardless,

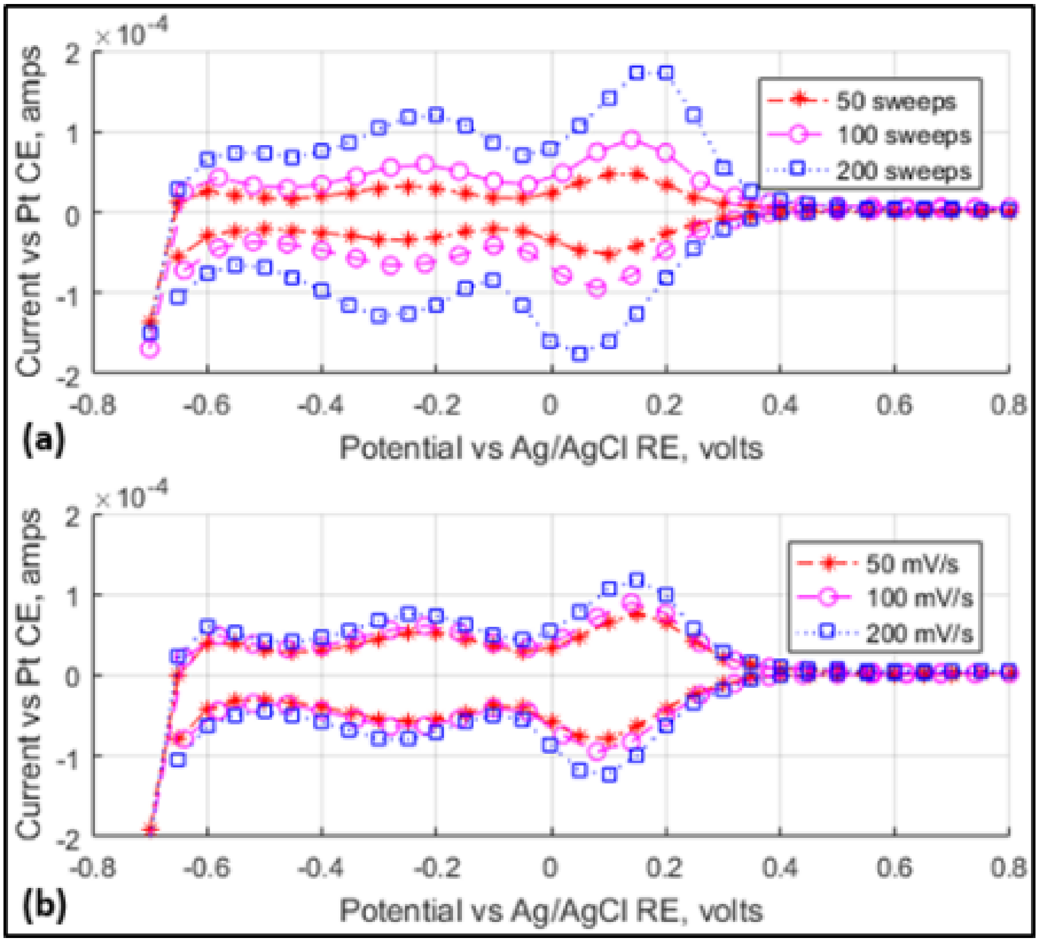

Figure 8- Final CV sweep envelope, multiple deposition parameters. (a) final sweep envelopes for different number of sweeps, run at 100 mV/s. (b) final sweep envelopes for different sweep rates, run for 100 sweeps each. Current maximums from each test are in tabular form in Table I.

TABLE I
AVERAGE CURRENT MAXIMUM CHANGES WITH TEST PARAMETERS

Parameter Change	Anodic Current @ Activation Voltage	Cathodic Current @ Activation Voltage
mV/s – 50	-79.7 µA @ 0.080 V	75.5 µA @ 0.152 V
mV/s - 100	-94.8 µA @ 0.088 V	90.1 µA @ 0.148 V
mV/s – 200	-125.1 µA @ 0.082 V	118.3 µA @ 0.144 V
	Avg = -303 µA/mV/s	**Avg = 287 µA/mV/s**
Sweeps - 50	-51.5 µA @ 0.087 V	48.3 µA @ 0.122 V
Sweeps – 100	-93.9 µA @ 0.079 V	90.4 µA @ 0.141 V
Sweeps – 200	-174.4 µA @ 0.047 V	177.5 µA @ 0.178 V
	Avg = -827 µA/sweep	**Avg = 856 µA/sweep**

the Ir(III)↔Ir(IV) transitions were deemed of highest import for this work, so Ir(IV)↔Ir(V) transitions were not heavily studied.

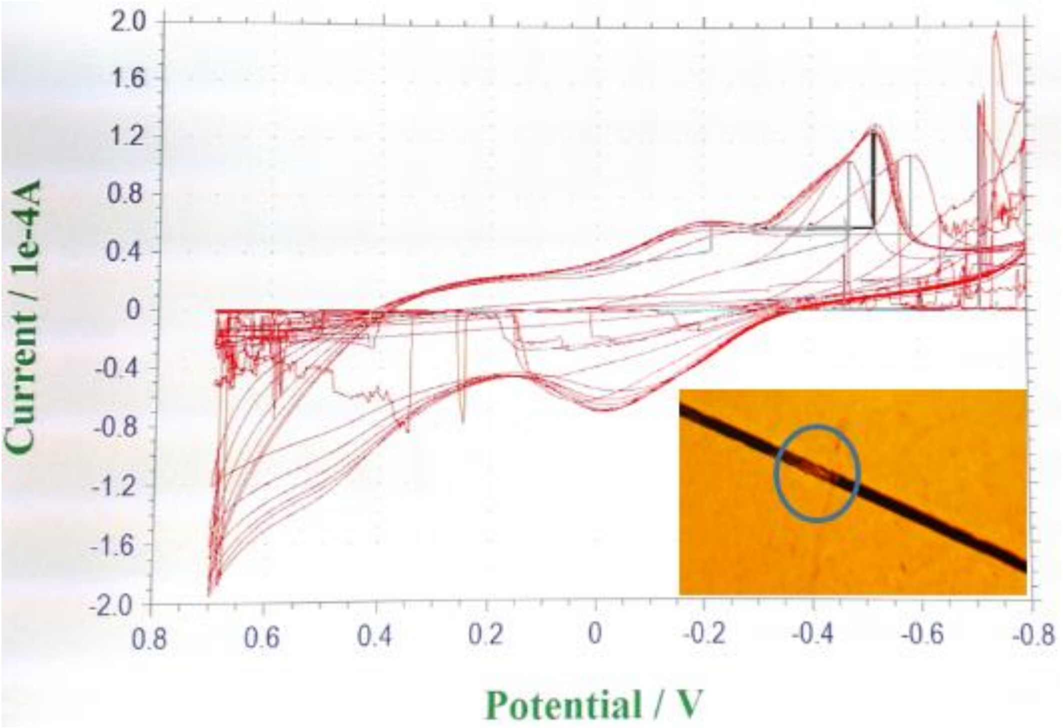

Figure 9- Voltammogram of probe run at 300 mV/s; inset- 50 µm trace damaged.

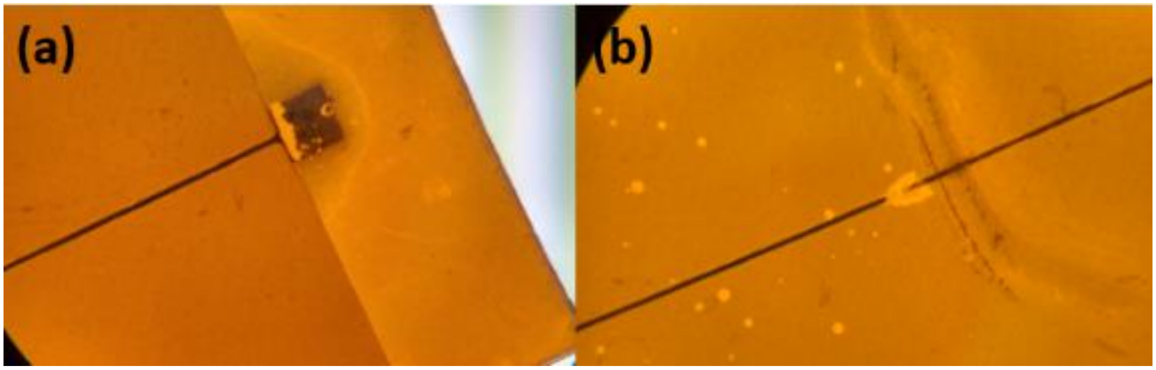

Figure 11- Extended voltage probe failures. (a) sensing pad failure. (b) trace failure.

Deposition parameters for the first electrodes were 100 mV/s ramps between 0.7 and -0.8V for 200 cycles, similar to those in [44]. Some experimentation was done with these parameters in order to take advantage of growth factors in the films and try to reduce coating time. As shown in Figure 8 and Table I, the number of sweeps performed and rate of those sweeps was varied between 50 – 200 sweeps and 50 – 200 mV/s, respectively. As will be noted, sweep count had a more pronounced effect on peak deposition current than sweep rate; this is likely because deposition current is directly related to total oxide thickness. Sweep rate, then, has a marginal effect because

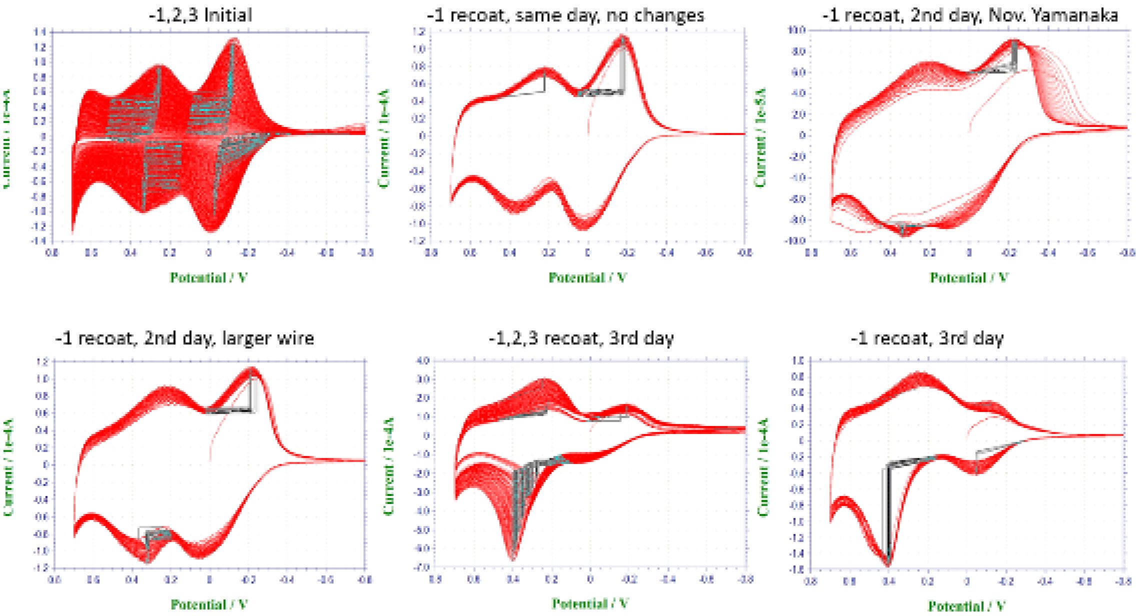

Figure 10- Examples of variability in the CV process. -1,2,3 indicate probe labels.

reactions may be mass transport limited and there is not, therefore, a linear change in oxide thickness with sweep rate. Effect of these parameter changes on probe performance will be discussed in the next chapter.

However, upper limits were quickly found in the sweep rates and maximum voltages possible. At 300 mV/s, for example, destruction of the probe occurred at various defect locations, as shown in Figure 9; these locations are assumed to be defects because the high melting temperatures of both Au and Cr would have thoroughly destroyed the surrounding polyimide, which did not seem to occur. Instead, it is likely that a deposit of some kind, or highly localized polyimide failure, caused this material removal.

A higher voltage range of ±2V was attempted but also regularly resulted in the destruction of the probe surface, as shown in Figure 11.

At certain points in time, the CV process is also prone to variability. An extreme example is shown in Figure 10, where the same three probes exhibited different redox processes and current

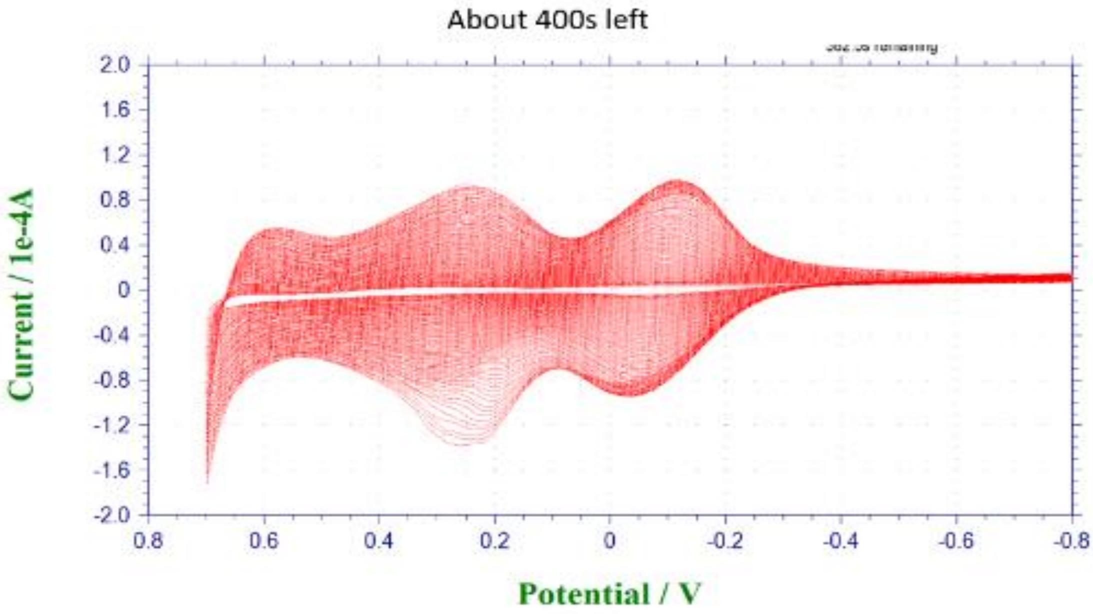

Figure 12- CV for "reversing" deposition. Note current peaks dropping in later sweeps.

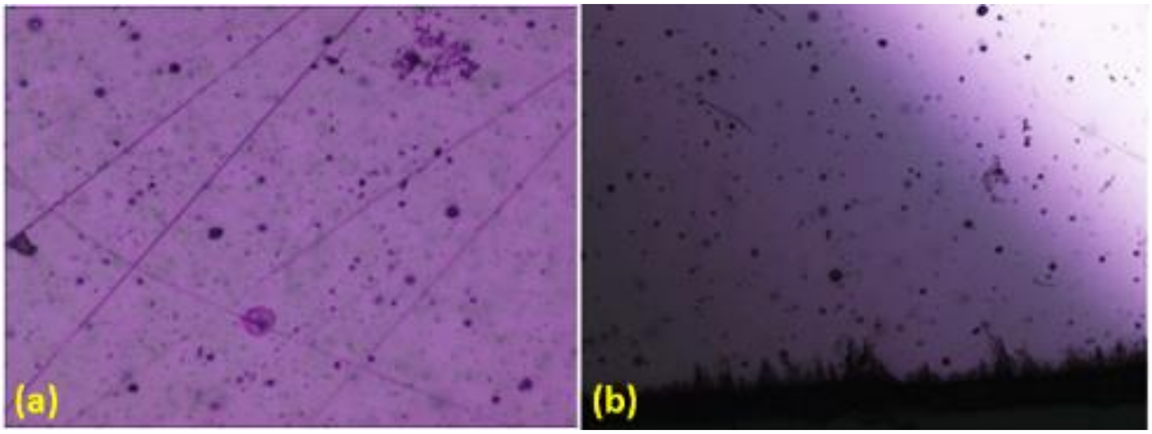

Figure 13- Optical microscope images of (a) typical bare polyimide sheet and (b) sputtered Au on polyimide sheet prior to any additional work.

densities when coated separately, with different Yamanaka solutions, or on different days. It is unclear what the predominant Ir(IV)→Ir(V) activation peak indicates.

When the CV process is behaving exceedingly poorly, the current peaks have been known to begin dropping towards the end of deposition. In Figure 12's CV, there were no redox reactions for almost 20 minutes, then normal coating took place, then current values started to drop again. The cause of this is unknown but one possible option is that there are side reactions occurring at the Au surface and possibly within the bulk as capacitance builds. Alternatively, target molecules in the deposition solution may be being depleted to the point of altering a reaction direction. As long as even a thin IrOx layer was deposited, however, probes were still typically able to have sensitivities above 65 mV/pH.

Some variation in CV performance from batch to batch is likely due to variability in the base polyimide (see Figure 13) or sputtered layers (see Figure 14 and Figure 15). Not only does the base material carry surface defects and roughness but every conformal layer after, including

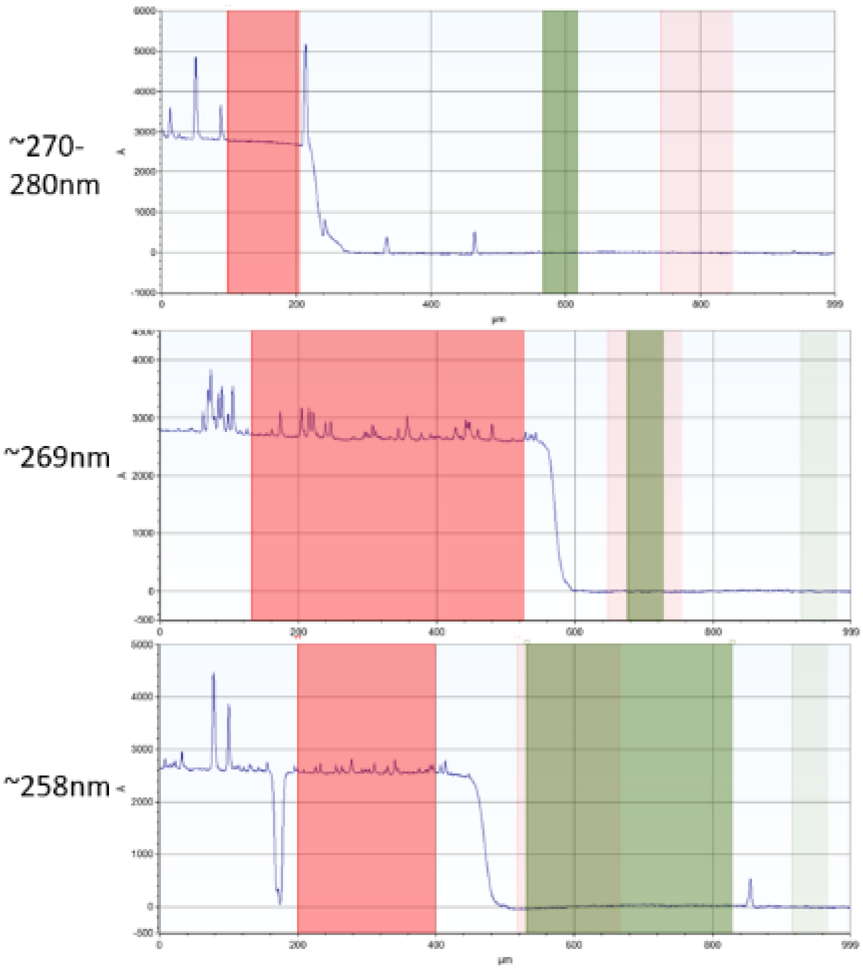

Figure 15- Variations in Au/Cr thickness and roughness at multiple locations across a sputtered glass slide.

sputtering, carries those defects and adds their own.

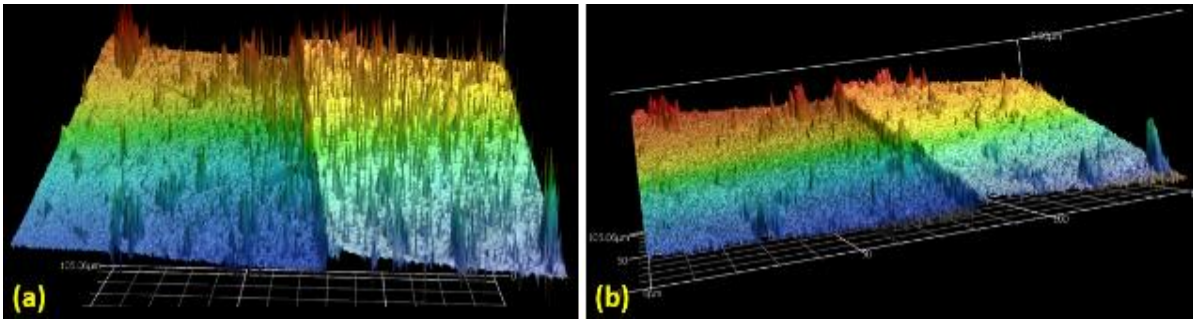

Figure 14- Laser confocal microscope readout of Au/Cr on kapton (a) without and (b) with averaging enabled. For reference, the average step height between the planes is calculated as roughly 260 nm.

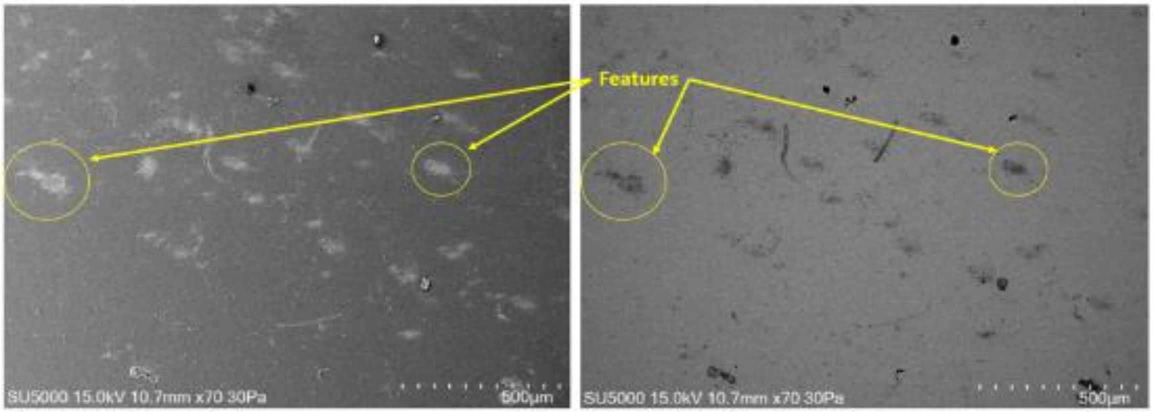

Figure 16- SEM images of suspect topography in deposited IrOx. Left - secondary electron detection. Right – backscattered electron detection.

Although they often do not, these surface features may sometimes manifest themselves in the finished product in highly visible ways. The sites shown in Figure 16 will typically be the origin of IrOx peeling and flaking.

As seen in Figure 17's inset, a fully formed iridium oxide film shows to be purple or deep blue in color, similar to the solution from which it was produced. As the main portion of the figure

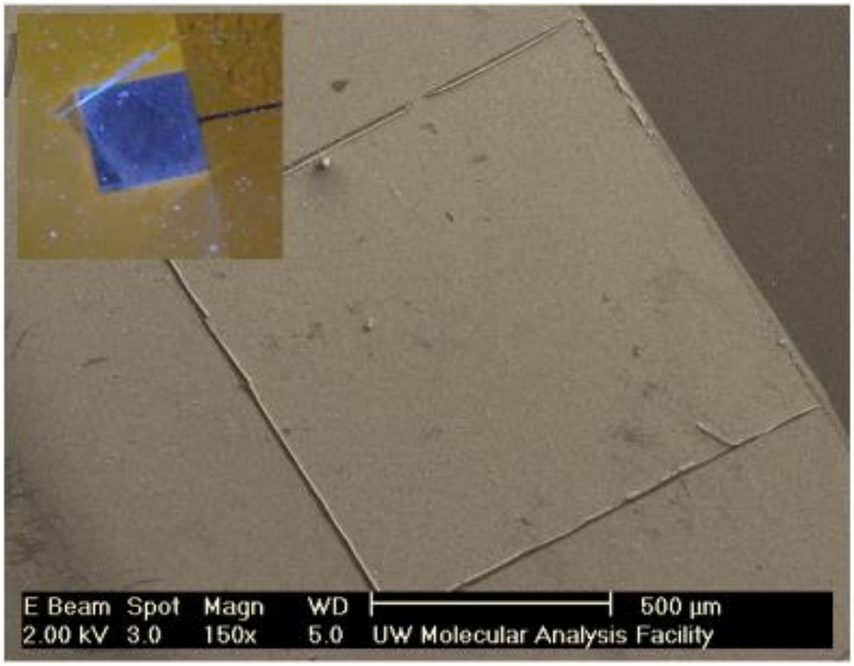

Figure 17- views of deposited IrOx layer on Au. Main - SEM view. Inset - optical microscope view.

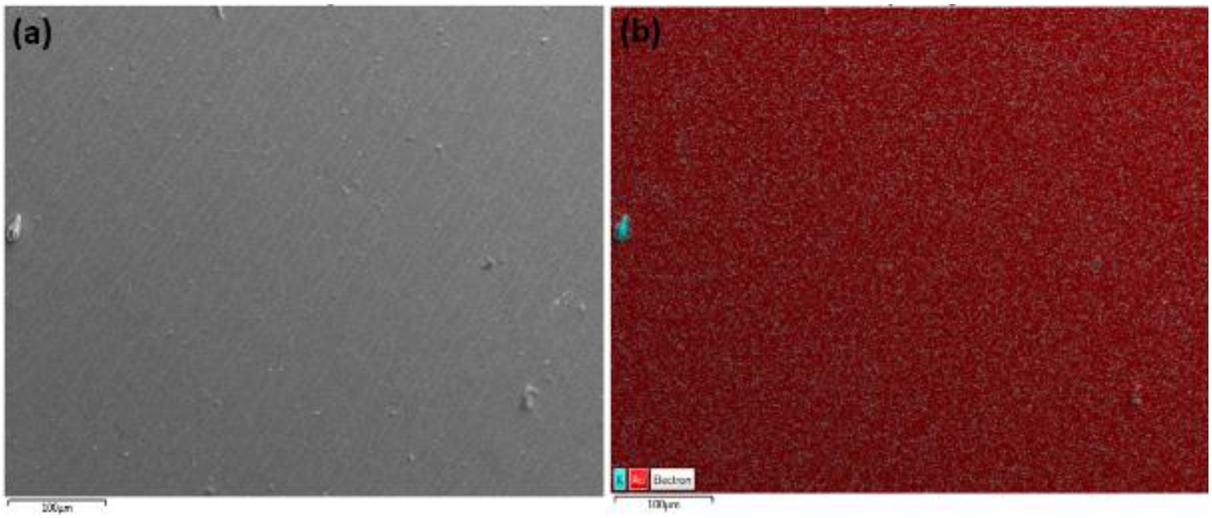

Figure 18- further morphology of deposited IrOx. (a) uniaxial IrOx grains as shown in EDS electron image. (b) highly uniform EDS elemental distribution of Au, indicating that grains are only present in the top layer.

demonstrates, the macro morphology of the surface produced by this method is quite smooth, confirming the findings of Elsen et al and others. Although hydration of the film affect this

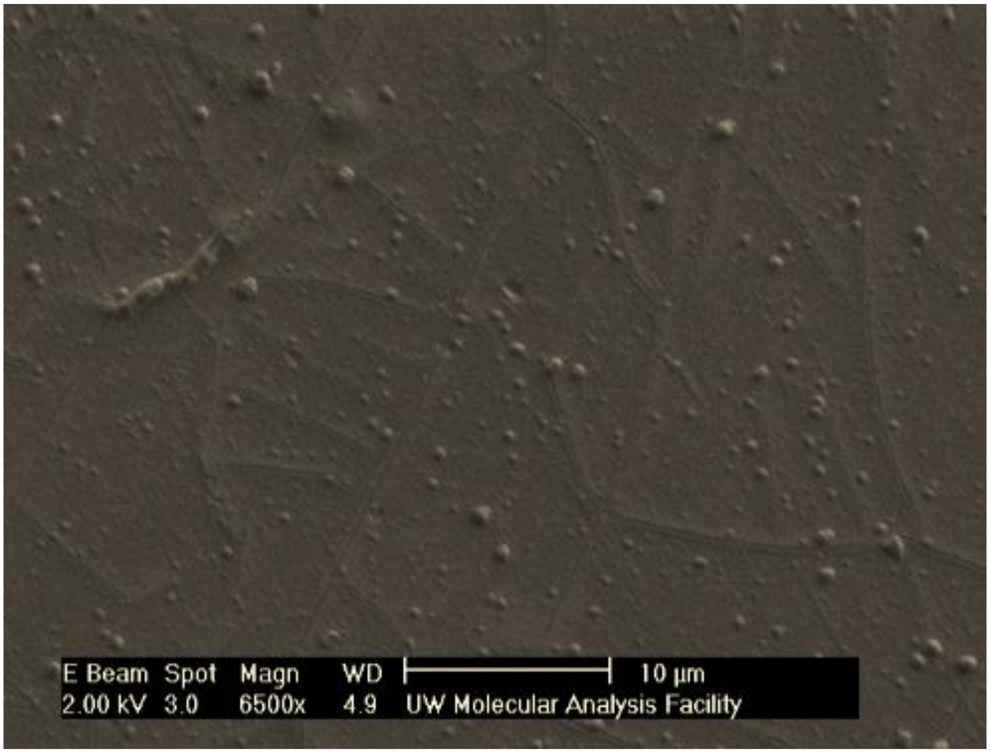

Figure 19- Further detail, IrOx grain structure. Spherical structures typically carbon contamination from poorly controlled specimen coating process.

morphology, the surface at this scale appeared to be largely similar.

Typically, single micrometer scale is quite different. The IrOx tends to form a grain structure typical to many metals; this is shown in Figure 18 (a). The associated panel (b) helps to illustrate that the grain structure appears to be present in only the IrOx, not the Au below it.

2.3 Reference Electrodes

In order to achieve complete pH microprobes, micro REs were developed on Au base electrodes (as will be discussed later, Cu base probes were not viable in this work). The AgCl paste (AGCL-675, *Applied Ink Solutions*, *Hudson*, *NH*) was manually secured over the electrode area through a guide template, and then cured on a hotplate at 130°C for 5 minutes. This work was only done for 1 mm^2 probes, due to hand fabrication difficulties at lower scales. Hand templates for smaller scale electrodes were attempted but are not discussed here extensively due to their low success rate.

Initial RE's were templated via translucent tape and trimmed with a hand tool under a microscope, as shown in Figure 20. As should be obvious, this method produced highly variable results. Multiple attempts were made to improve the guide template. Typical 3D printing technologies could not produce features small enough; SLA, for example, could only reliably produce features down to 500 µm, whereas 200 µm templates were required. Attempts were made

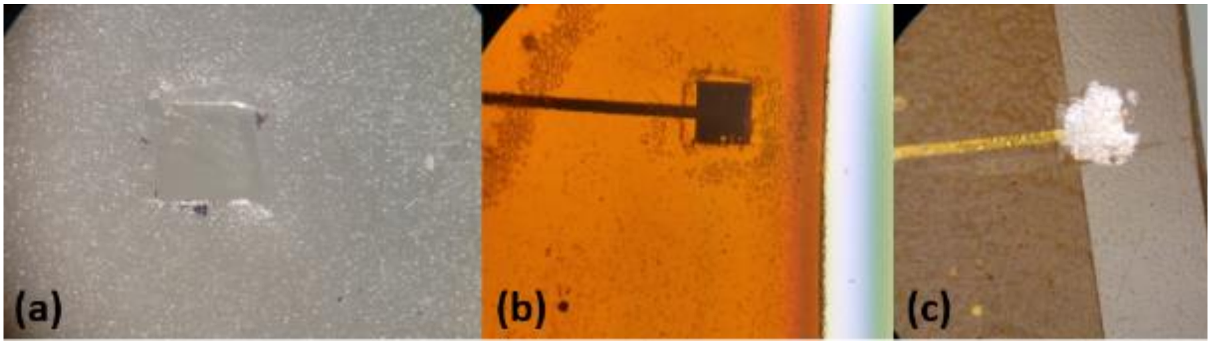

Figure 20- RE fabrication process. (a) templated translucent tape. (b) template applied. (c) AgCl applied and tape lifted.

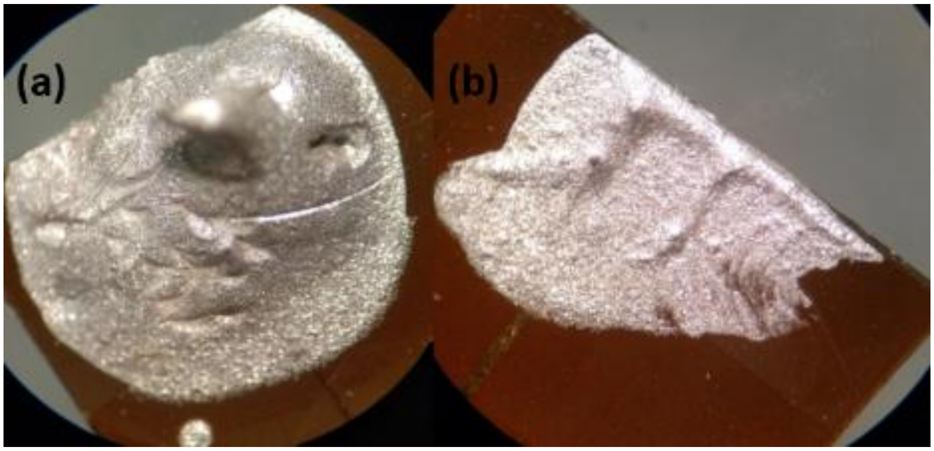

Figure 21- Variations in AgCl thickness cause curing issues. (a) Even at 130°C and a 1 day rest, thick deposits are still soft (note indentations. (b) more uniform, thinner deposits cure easily.

to etch glass slides using hydrofluoric acid (HF), similar to [45]; however, photoresists available did not withstand the HF.

The curing profile also required a uniform thickness of the AgCl paste to be applied. As shown in Figure 21, highly non-uniform and thick films would not cure, even at higher temperatures and longer delay times.

Interestingly, the materials inherent to the paste tended to phase separate and form different morphologies, as demonstrated in Figure 22.

2.4 Probe Degradation

This section begins with a discussion of means, from a materials point of view, of characterizing the degradation of IrOx over time and with use. One obvious solution may be deriving thickness loss from EDS elemental percentages.

By the Kanaya-Okayama formula, electron range into sample materials for SEM/EDS (in µm) is found as

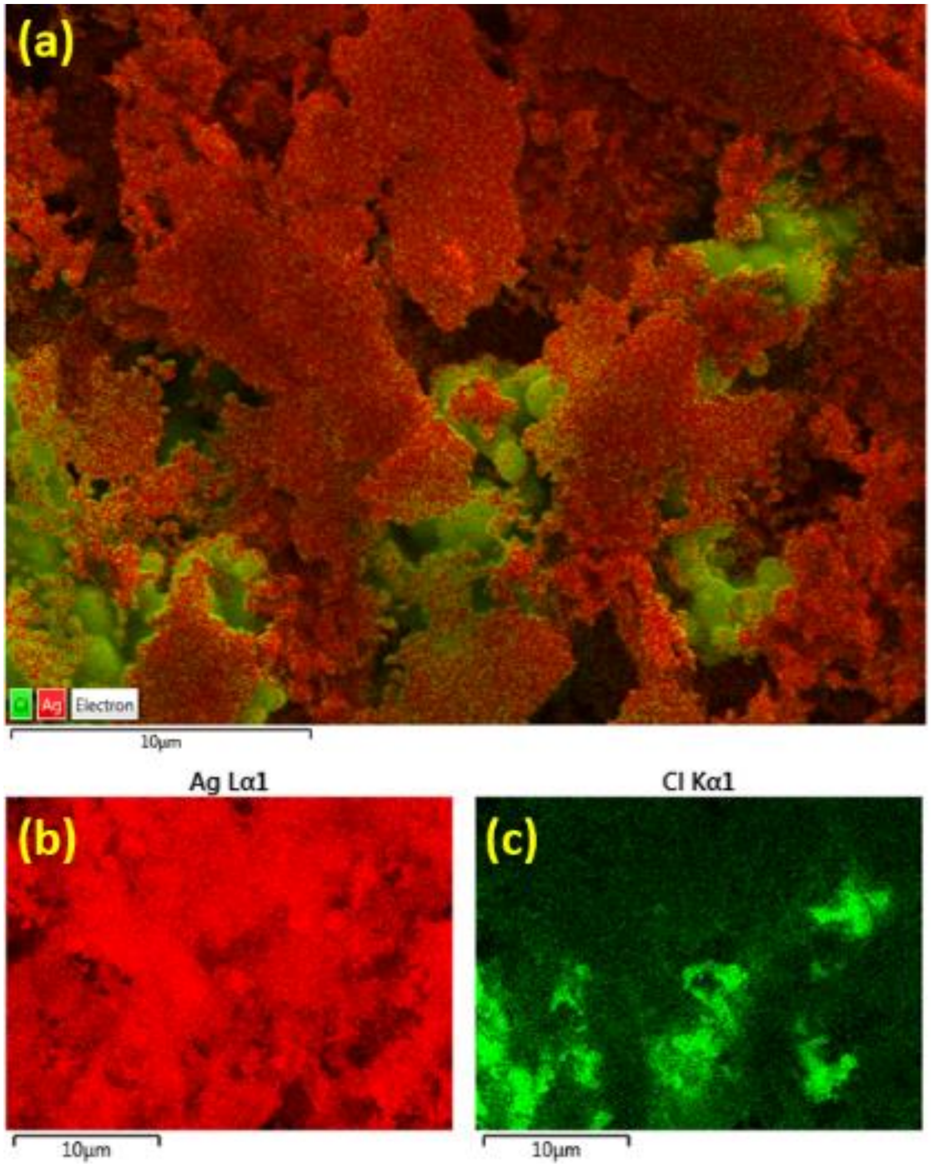

Figure 22- EDS imaging of AgCl paste, post application. (a) layered map demonstrating nearly phase separated Ag and Cl. (b) Ag map derived from L-orbital, α-level X-ray peak; note flake morphology. (c) Cl map derived from K-orbital, α-level X-ray peak; note globular structures.

$$R_{KO} = \frac{KE_0{}^n}{\rho} \qquad \text{Eq. 1}$$

Where $K = \frac{0.0276*A}{Z^{0.889}}$, A is the atomic weight in g/mole, Z is the atomic number, ρ is the density in g/cm^3, E_0 is the incident beam energy in keV, and n = 1.67 [46]. Based on this calculation, and the assumed factors in Table II, it would seem that imaging and elemental analysis,

TABLE II
MATERIAL PARAMETERS FOR KANAYA-OKAYAMA CALCULATIONS

Material	Atomic Weight (g/mol)	Atomic Number	Density (g/cm^3)
Au	197.0	79	19.32
Ir	192.2	77	22.65

at 5 keV, of pure Ir and Au could be no deeper than 85 nm and 72 nm, respectively.

Not only will this vary when IrO_2 structure and size is taken into account, but it is assumed that film uniformity affects it and Monte Carlo simulation of electron trajectories has shown that the majority of backscattered electrons from limited upper volumes anyways [46]. This indicates that relative EDS elemental percentages are a poor proxy for oxide thickness.

Profilometer measurements were also highly variable, even in slow scans and high scanning resolution with low probe forces, due to both a) the polyimide flexing slightly under the force of the profilometer, and b) any non-uniformity of the polyimide being carried over into the sputtered Cr/Au or Cr/Cu and then into the IrOx, due to its conformal nature. Therefore, degradation was generally analyzed qualitatively through SEM imaging and EDS elemental distributions, not percentages.

As will be discussed in the next chapter, some of the pH buffers used for calibration are highly acidic (down to pH 2) and contain hydrochloric acid (HCl), both of which are known to degrade Ir. Combined with a virtual ground voltage supplied to the reference electrode, the IrOx films regularly saw distinct degradation on the microscale. Figure 23 shows one such surface after only a few rounds of testing. As can be seen, the IrOx film begins to separate at its grain boundaries

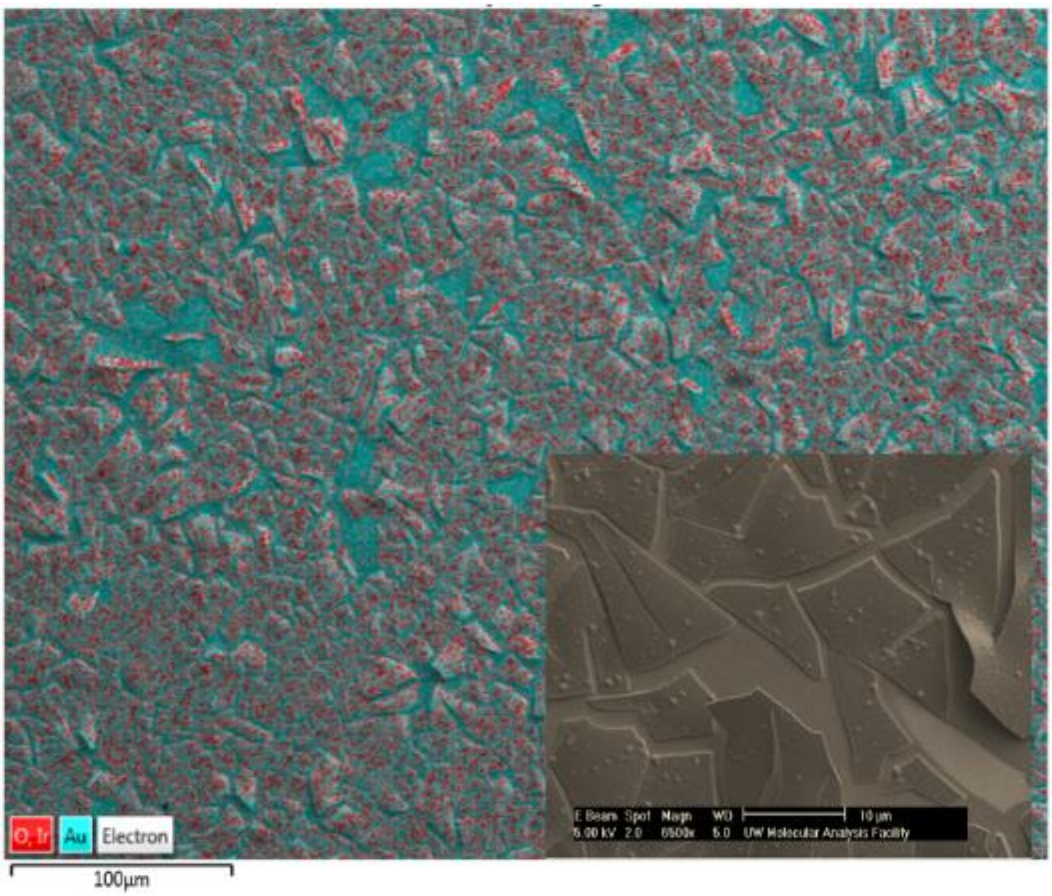

Figure 23- IrOx surface post testing cycles. Inset - electron image of IrOx grains at higher zoom level.

until it starts to "peel" and, ultimately, lifts off of the Au surface entirely.

To alleviate this to some degree, hydration (constant immersion in DI water) of the IrOx films and creation of non-HCl acidic buffers were created. Also, per earlier sources, thinner films (i.e. lower CV deposition currents via shorter runs) were sometimes used. Explicit longevity characterization was not performed but qualitative SEM imaging suggested that some combination of these improved the number of tests over which similar sensitivities could be recorded. One such

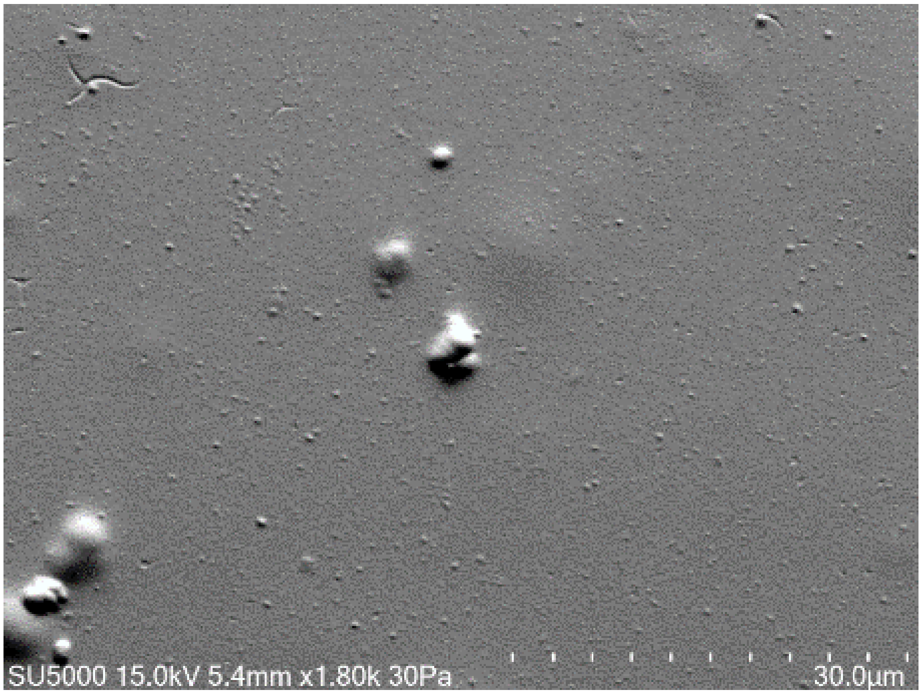

Figure 24- SEM imaging on reduced current IrOx film after buffer testing in non-HCl buffers.

probe surface is shown in Figure 24.

Despite the morphology differences, AgCl paste experienced similar degradation. Specifically, both Ag flakes and Cl globs lifted off together. This is shown in Figure 25.

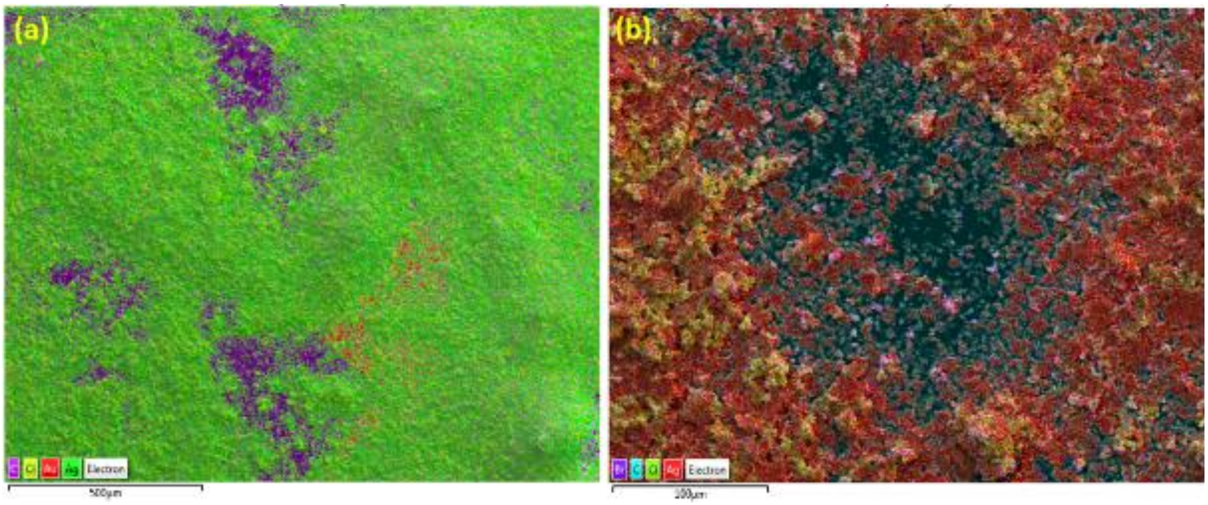

Figure 25- Loss of AgCl paste post testing. (a) layered EDS elemental map showing regions of AgCl replaced by carbon contamination or bare Au. (b) Similar EDS layer map at a higher zoom level, confirming that both Ag and Cl were removed together.

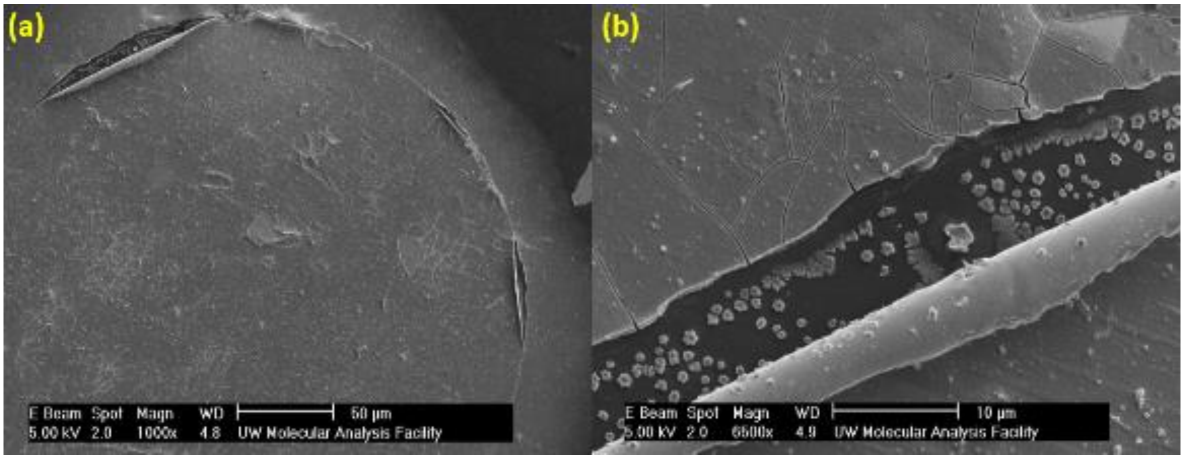

Figure 26- "Peeling" failure of coating and substrate, shown at (a) low and (b) high magnifications.

The combination of both types of degradation would seem to indicate that Au-M adhesion is weak in relation to the top layer's adhesion between its phases (in AgCl's case) or other deposited sites (in IrOx's case).

On occasion, the Au/IrOx layer has peeled up entirely. It is assumed that this is due to

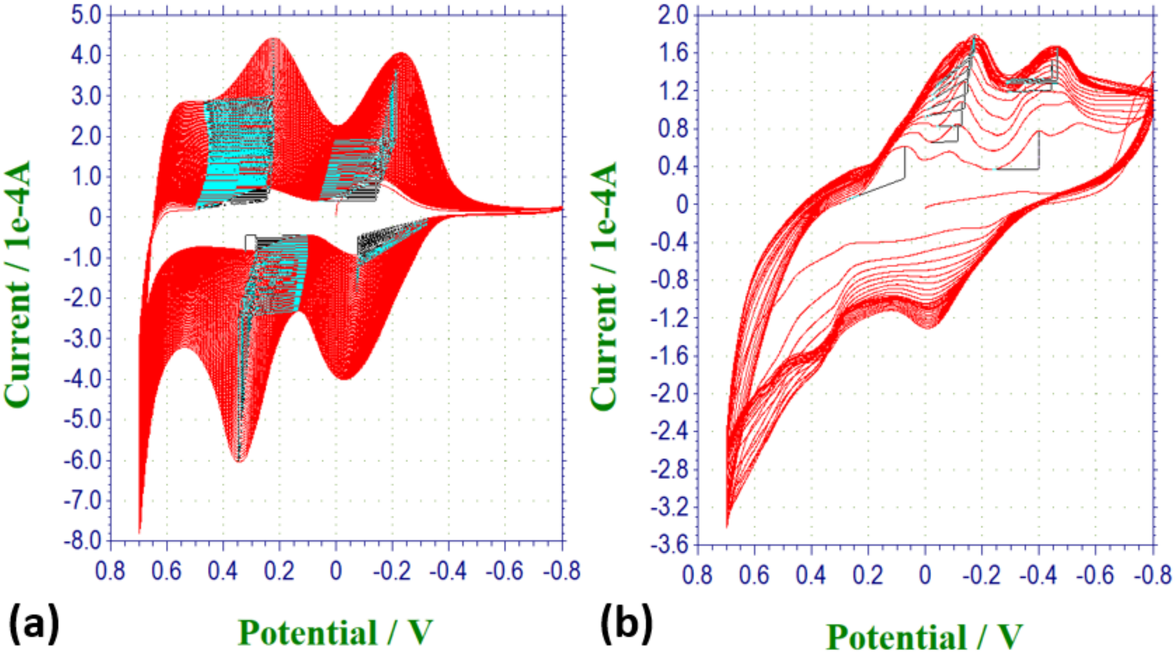

Figure 27- Au vs Cu in IrOx CV. (a) typical Au CV, four 1 mm^2 probes. (b) typical Cu CV, four 1 mm^2 probes.

internal stresses in the IrOx layer and mechanical coefficient-of-thermal-expansion (CTE) differences between the metals; though use temperatures are low, short duration “events” of high current could be an issue. This failure mechanism is shown in Figure 26.

2.5 IrOx and Conductive Layer Substrates

Due to the higher expense and lower availability of Au with respect to Cu, copper was attempted as a substrate for the IrOx. In general, Cu was a much more difficult material to achieve a proper coating on. The first indication of this came in the form of significantly reduced deposition currents, as well as vague redox activation peaks, across the voltage range. An example of this is shown in Figure 27.

Even with varied deposition parameters and alcohol cleaning of the substrate prior to deposition, adhesion of the IrOx to the Cu was extremely poor. Even if long deposition runs were able to produce small patches of deposited surface (see Figure 30(c)), the IrOx would almost

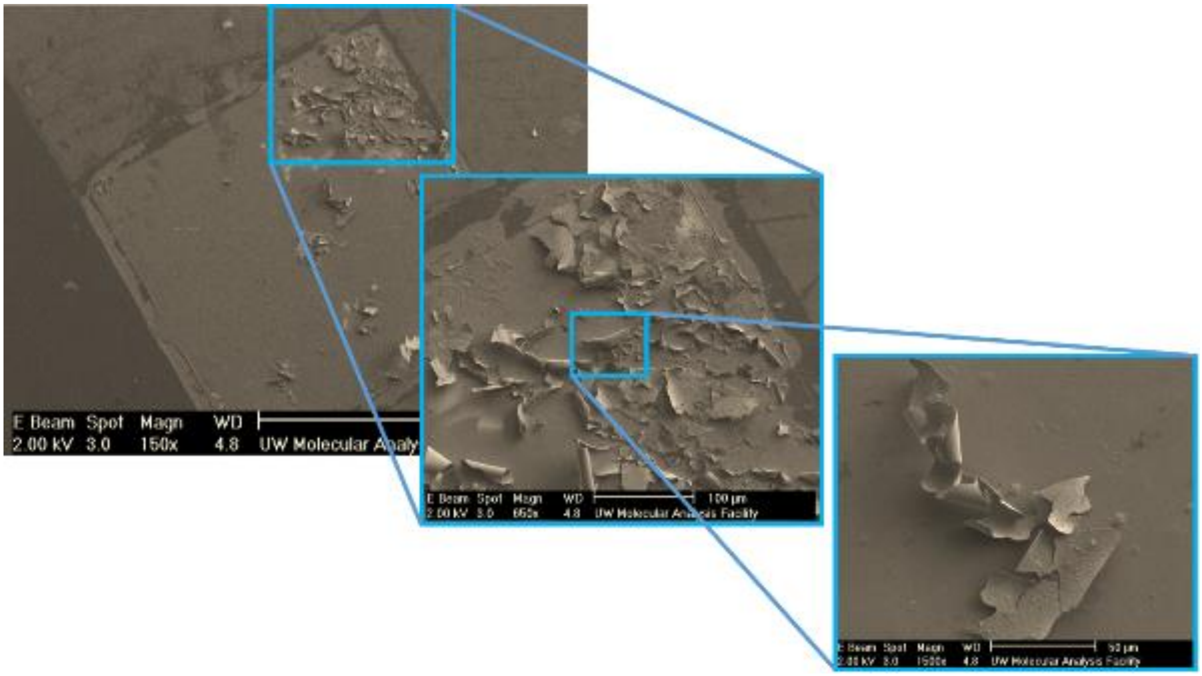

Figure 28- IrOx flaking on Cu at multiple zoom levels.

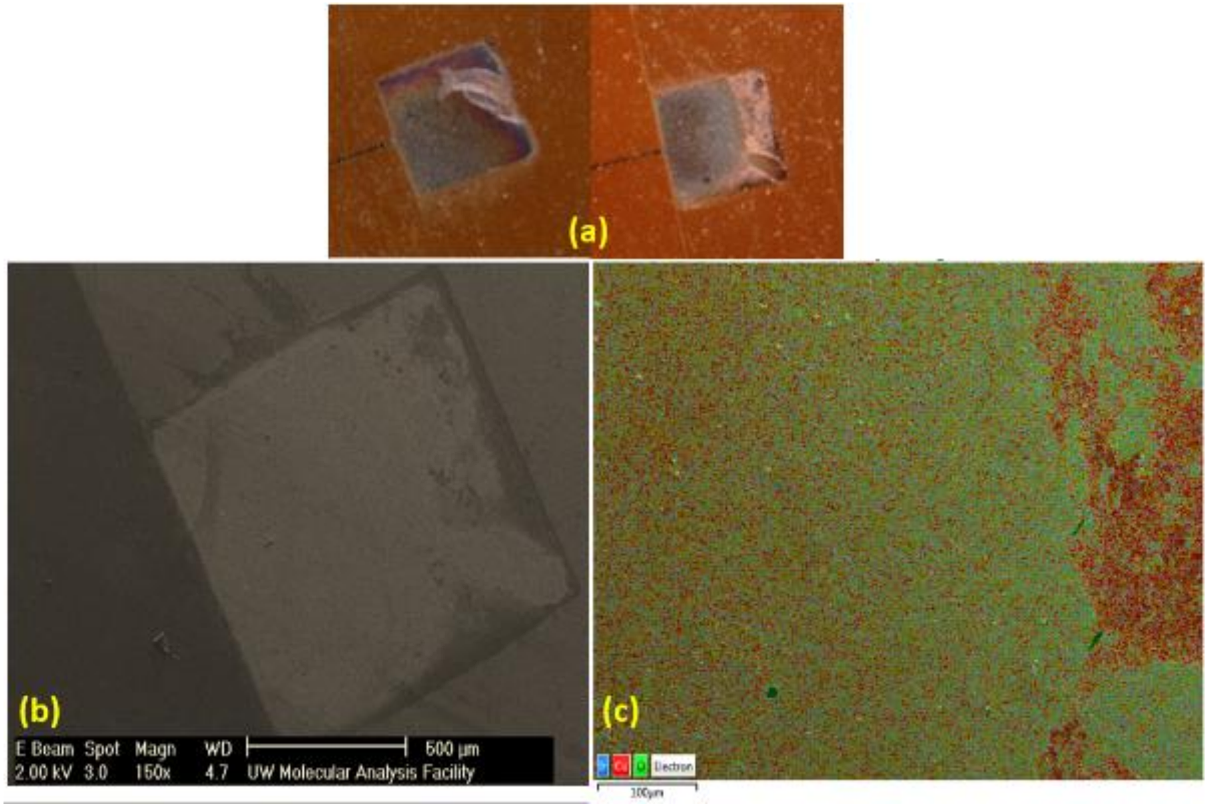

Figure 30- Evidence of poor IrOx coating on Cu; all images taken prior to buffer testing. (a) microscope images of two IrOx/Cu probes. (b) SEM image of IrOx/Cu probe. (c) EDS layered map showed regions of zero IrOx adhesion.

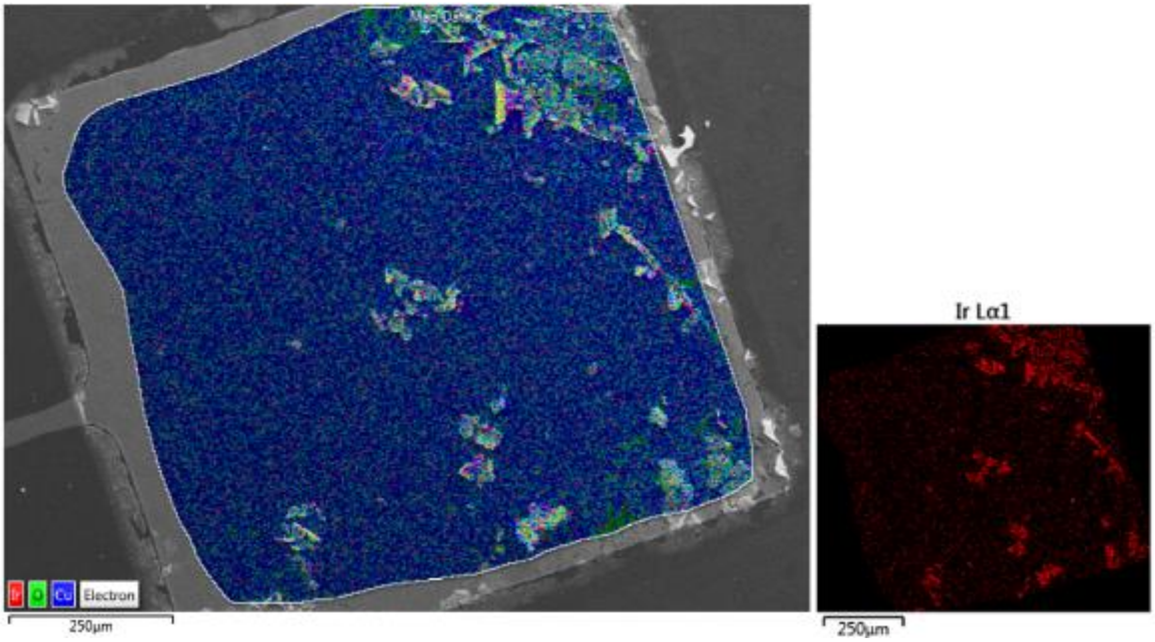

Figure 29- EDS mapping of IrOx on Cu. Left - layered map. Right - Ir only.

immediately flake and lift off in the presence of HCl. This severe flaking, after only initial testing, is shown in Figure 28. The lack of IrOx post buffer testing may be more apparent in Figure 29.

For this reason, Cu probes were focused on in x-ray photoelectron spectroscopy (XPS) studies of the probes. . shows the Cu and Ir oxidation state percentages before and after testing in pH baths. The names include fractional values indicating spin-orbital coupling. As evident, the substrate was heavily reduced from a majority of Cu^{2+} to a majority of $Cu^{0,1+}$ when tested in pH buffers. The little Ir deposited and maintained on it saw a binding energy shift of ~0.1 eV (Ir $4f_{7/2}$) but indication of an oxidation state change was difficult to declare, due to a lack of Iridium Oxide NIST traces (used as references in XPS studies), aside from IrO_2.

The actual emissions peaks before and after pH bath testing can be seen in Figure 32.

The indications of Cu oxidation perhaps leave open the possibility of attempting a surface reduction in the future before IrOx coatings.

Table III
XPS Parameters for IrOx on Cu [7]

Name	Position (eV)	State Assignment	Group %
Before pH bath testing			
Cu 2p$_{3/2}$	932.2	$Cu^{0,1}$	21.3
Cu 2p$_{3/2}$	934.5	Cu^{2}	78.7
Ir 4f$_{7/2}$	62.2	IrO_2	100
Ir 4f$_{5/2}$	65.1		
After pH bath testing			
Cu 2p$_{3/2}$	932.4	$Cu^{0,1}$	53.9
Cu 2p$_{3/2}$	933.8	Cu^{2}	46.1
Ir 4f$_{7/2}$	62.1	IrO_2	100
Ir 4f$_{5/2}$	65.1		

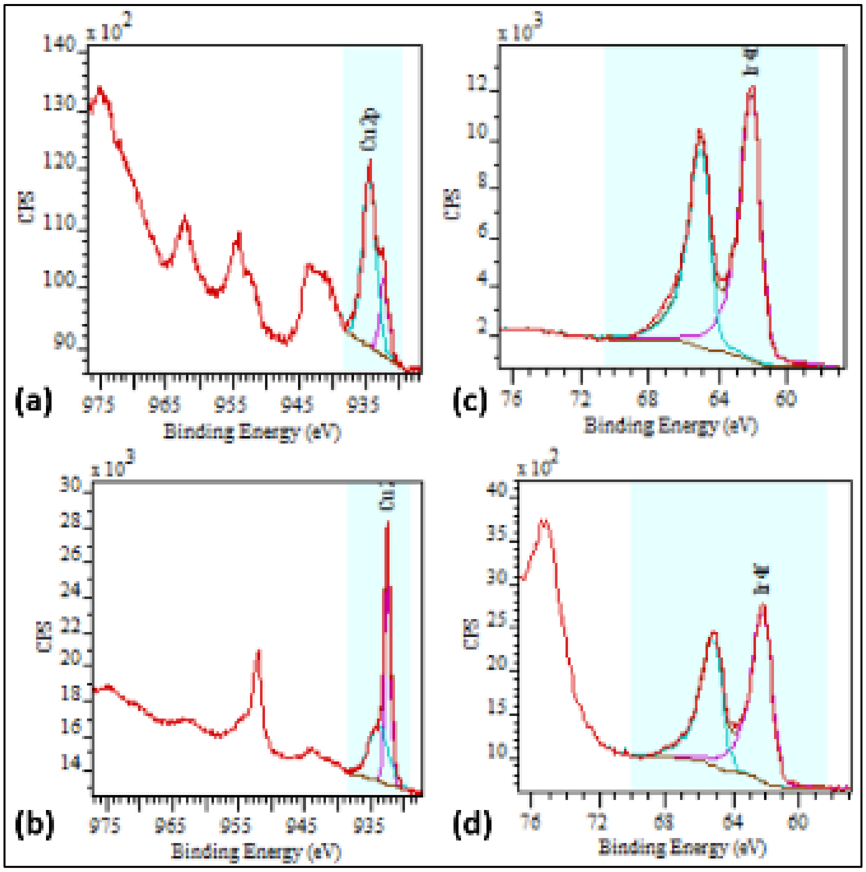

Figure 32- Localized XPS curves for Ir and Cu states. (a) Cu peaks before testing and (b) after testing. (c) Ir peaks before testing and (d) after testing.

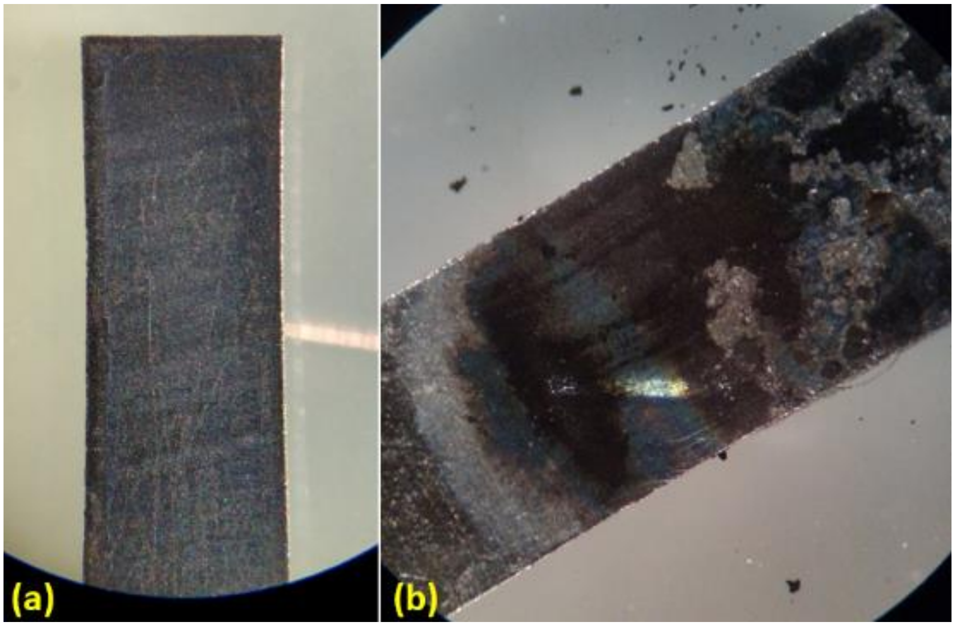

Figure 31- Variable Ag wire coating. (a) positive result. (b) negative result.

An attempt was also made to coat directly onto a small piece of Silver wire, with variable

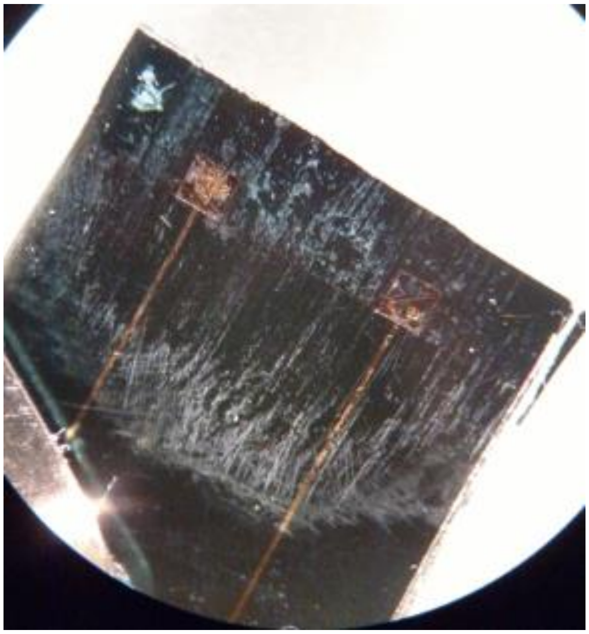

Figure 33- IrOx deposition on Au/Cr/Si.

results. This may have been due to improper cleaning practices but this was not explored further. An example is shown in Figure 31.

Lastly, attempts were made to coat on Au/Cr which had been deposited on Si substrates. Limited success was seen here and this substrate was shelved for future work. IrOx surfaces are shown in Figure 33.

3. Probe Characterization

This chapter will describe the operation of the IrOx sensing surface, the resulting characterization and calibration steps resulting from the knowledge of that mechanism, the setup used to perform characterization and calibration, and those characterization results. Additional steps to improve test results and efficiency will be discussed at the end.

3.1 Transducer Mechanism

The sensing mechanism of IrOx in the presence of hydrons is assumed to be the formation of capacitive double layers around the intercalated (adsorbed) solid oxide phase near the solution interface [34]. Several authors believe this intercalation to affect the stoichiometry of the solid phase metal oxide, releasing further protons and allowing potentials higher than Nernstian theory predicts [36, 37].

Fog and Buck's 1983 paper on oxide-based pH sensors [34] provides much of the necessary background. In their opinion, there is intercalation happening at the oxide surface by oxygen, which creates an electrical potential due to hydrogen ion and oxygen activity. As an aside, "activity" is roughly synonymous with concentration in this context; that being said, activity can be affected by concentration, pressure, temperature, species interaction, electromagnetic force interactions, and other factors. They surmised that the intercalation reaction occurring at the electrode surface could be represented as

$$MO_x + 2\delta H^+ + 2\delta e^- \rightleftarrows MO_{x-\delta} + \delta H_2O \qquad \text{Eq. 2}$$

In Eq. 1, M represents a metal (such as Ir) and δ represents partial atomic charge. In other words, the metal oxide alters its potential in the presence of free electrons and protons. In the intervening years, the redox equilibrium of IrOx under acidic or basic conditions was found to belong to one of three possible states [5]:

$$2Ir + 3H_2O \rightleftarrows Ir_2O_3 + 6H^+ + 6e^- \qquad \text{Eq. 3}$$

$$Ir + 2H_2O \rightleftarrows IrO_2 + 4H^+ + 4e^- \qquad \text{Eq. 4}$$

$$2IrO_2 + 2H^+ + 2e^- \rightleftarrows Ir_2O_3 + H_2O \qquad \text{Eq. 5}$$

Therefore, we would expect to see one or both of the oxide states mentioned, Ir_2O_3 and IrO_2, in solution during the reaction. Although solution spectroscopy was not run during probe testing, earlier reading and experimentation (see previous chapter) indicated that IrO_2 is indeed consistently present and.

Essentially, the resulting hypothesis was that electrode potential depends on both the concentration of the hydron in liquid (typical pH definition) and of oxygen in the solid phase (so the stoichiometry of the metal oxide). If we are to believe that there is some stoichiometry change of the metal oxide in different pH baths due to oxidation state change, then we might theorize that electrode size can affect the rate of oxide stoichiometry change due to pH, at least in the probe configurations shown. This will be of interest later on.

The potential generated at such a solid metal oxide and ionic liquid interface was described by Fog and Buck using a variation of the Nernst equation, as

$$\varphi^s - \varphi^l = 'constant' + \frac{RT}{F}\ln a^l{}_{H^+} + \frac{RT}{2F}\ln a^s{}_O \qquad \textit{Eq. 6}$$

In Eq. 6, φ^s and φ^l are the galvanic potentials of the solid and liquid phases, respectively, the constant is not named but is assumed to be the standard electrode potential as describe elsewhere, R is the universal gas constant, T is the temperature (in Kelvin), F is Faraday's constant, and $a^l{}_{H^+}$ and $a^s{}_O$ are the liquid hydrogen ion activity and solid oxygen activity, respectively [34].

This potential equation had also been updated. The basic Nernst equation can be described as:

$$E = E_0 + \frac{RT}{nF}\ln\frac{a_r}{a_o} \qquad \textit{Eq. 7}$$

Where E is the cell potential, E_0 is the standard electrode potential, R/T/F are the givens from above, n is the number of electrons being transferred by the element of interest, and a_r and a_o correspond to the activities of the reduced and oxidized chemical species, respectively. In the measurement of pH, hydrons are the element of interest, so n = 1. Typically, pH is defined as

$$pH = -\log_{10} a_{H^+} \qquad \textit{Eq. 8}$$

and thus the natural log term in Eq. 7 will need to be converted to $\log_{10}$ and the activities replaced by hydron activity; this base e to base 10 conversion will add a multiple of 2.303, and the sign inversion will need to be taken into account. Finally, test conditions will be considered standard for the purposes of this thesis (25°C), which will reduce the RT/F term to a constant. Considering all these factors, Eq. 7 can be converted to:

$$E = E_0 + 0.05916 * pH \qquad \text{Eq. 9}$$

This is where the term "Nernstian sensitivity" comes from; an electrode meeting roughly 59.2 mV/pH is considered to be near this ideal. Many electrodes have been shown to be "super-Nernstian," meaning that they exceed this sensitivity level. In Eq. 9, E_0 will be replaced by the standard electrode potential of whatever stable reference electrode is being used. In this case, an Ag/AgCl RE will be used exclusively, which has a known standard potential of 0.577 V [6].

As briefly mentioned above, there has been discussion in the literature about how sensitivity levels above the Nernstian limit might occur. Besides Fog and Buck, Burke and Whelan [35] speculated that sensitivities exceeding the Nernstian limit may be a result of oxide stoichiometry change and activity reduction in presence of ions. Hidalgo-Acosta et al [36] went further in saying that the proton release from certain Ir-OH complexes causes further proton release from the films when the acid-base equilibrium is thrown off, thereby improving electron ratios during Ir redox state transformation.

Elsen et al [12] extensively studied various other factors influencing probe behavior. Many were discussed in the "Materials Characterization" chapter but some are relevant in the context of this discussion. First, they conclude that thinner oxide films yield faster response when subjected to pH changes; as discussed previously, IrOx film thickness could not generally be characterized due to substrate difficulties, but CV current maximums can be treated as a proxy for thickness, in

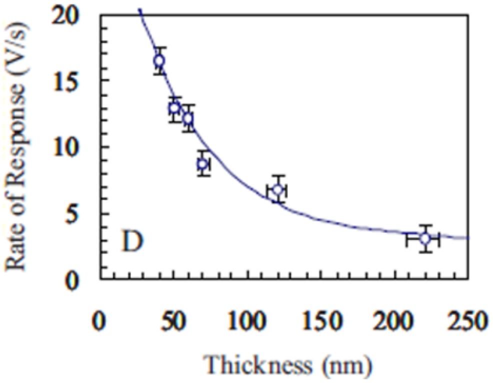

Figure 34- Example of batch max response rate of thin films versus film thickness, produced by cyclic voltammetry growth. Adapted from [12].

a relative and qualitative sense. Response rates demonstrating a notable plateau above a certain film thickness, however, are shown in Figure 34.

They also noted that increasing film thickness had the added effect of increasing film capacitance. The reason for this is that the adsorbed ion layer and charge-restrained ion layers at the surface of the electrode do not dramatically change in thickness (on the order of angstroms and nm, respectively) with respect to the film bulk thickness, as shown in the solution-electrode interface in Figure 35 [2]. Therefore, the authors recommended that both film thickness and surface area (due to proton diffusion area, which also affects capacitance) be minimized to reduce capacitance and, therefore, response time. There is a compromise, then, between the response time, sensitivity, and probe longevity that comes into play with probe surface area and film thickness.

3.2 Testing Regime

Given the mechanisms as described previously, both in this chapter and the previous, there are multiple tests of probe performance necessary: first and most importantly, determining the

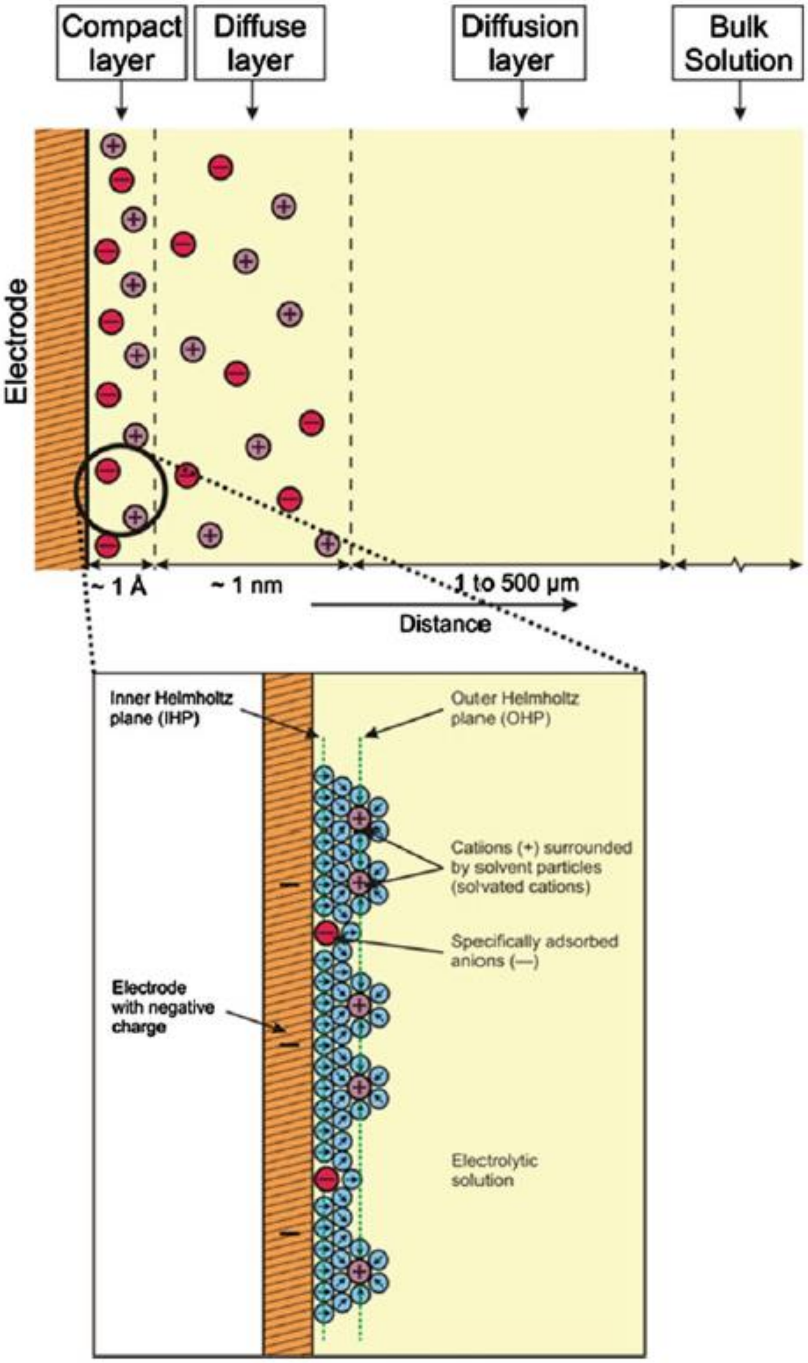

Figure 35- Typical interface potential regions when an electrode is in contact with ionic solution. Taken from [2].

relationship between potential developed by the probe and various pH levels (i.e. determining the scaling factor in the modified Nernst equation). Second, determining the response time of the probe. Third, determining the lower limit of detection (LOD) of the probe to quantify its step sensitivity and short term stability. Fourth, determining its repeatability, also known as hysteresis, over a long testing period. Finally, real world viability was tested by finding the probe's selectivity to hydrons in the presence of cations typically present in water, such as salts, and actually proving that sensor performance is not degraded when the probes are conformed to curved surfaces (i.e. is the flexible sensor actually flexible).

For sensitivity determination, probes were calibrated by passing them through multiple pH buffers while monitoring the resultant potential (through hardware discussed in the next section) between the fabricated working electrode and a fabricated or commercial reference electrode, depending on the test. During testing, probe spacing was maintained using a holding

TABLE IV
PH BUFFER CONSTITUENT CHEMICAL SPECIES

pH	Chemicals	Manufacturer / Model
2	Hydrochloric acid, potassium chloride, formaldehyde, methyl alcohol	Fisher Scientific / SB96-1
4	Potassium acid phthalate, sorbic acid	Fisher Science Education / S25849A
7	Potassium phosphate, sorbic acid	Fisher Science Education / S25849B
9	Potassium chloride, boric acid, sodium hydroxide, tetrasodium EDTA	Fisher Scientific / SB114-1
10	Ethylenediaminetetraacetic acid, potassium carbonate, boron potassium oxide, potassium hydroxide	Fisher Scientific / 13636AR10

fixture. The buffers used are shown in Table IV. If a result has 5 points, these buffers were used as is; if a result shows 6 points, this indicates that buffers of pH 2 and 10 were excluded and diluted buffers of pH 5, 6, and 8 were included with standard buffers of pH 4, 7, and 9.

For each individual measurement, the probe and reference were placed into a commercial buffer and the potential was allowed to fully settle; for a typical electrode, this period may last 30 to 60 seconds. Next, the electrode pair was dipped into a DI water bath to clear the prior pH solution from it, and it was gently dabbed dry with a thin cellulosic wipe (Kimwipe, Kimberly Clark, Irving, TX) before immersion in the next bath.

Response time does not have a standardized definition but was tested in a manner similar to other researchers: the time taken between probe immersion in a buffer solution until it has reached 90% of its stabilized potential [6]. To simplify and expedite testing, the neutral pH 7 buffer was used in between dips into deionized water.

One method of defining limit of detection is as follows [8]:

$$LOD = 3 * \frac{\sigma}{sensitivity} \qquad \text{Eq. 10}$$

Where σ is the standard deviation of a fully settled pH 7 baseline value and sensitivity is the calibrated sensitivity value as taken from the slope a least squares linear regression performed on the data outputs from the sensitivity test; the intercept of this regression will also provide some information later. In other words, the limit of detection is the ratio of the probe's 3σ noise level to its sensitivity, thereby being the smallest change recognizable in signal output assuming mean-centered Gaussian noise.

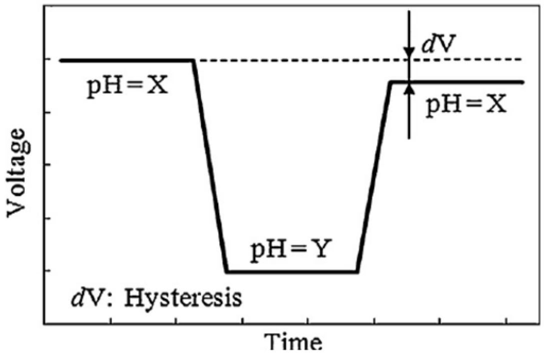

Figure 36- Schematic definition of hysteresis [6]

Hysteresis is most easily described as the difference between readings stemming from the same buffer after the probe has been subjected to an intervening buffer test of a different pH level. This is illustrated schematically in Figure 36. Some authors also term this “reversibility,” as it describes some of the differences in alternating pH levels in an increasing or decreasing fashion [6].

Selectivity can be described as the offset of probe potential in the potential of interfering ions. Ideally, the probe would be sensitive to only hydrogen ions; in practice, however, a number of cationic species can induce a potential in these films. Outside of the obvious salts, metal species such as iron (Fe) and lead (Pb) can also affect output, and those readings can be further affected by solution temperature [38]. In fact, even parameters such as dissolved oxygen can have an effect on output potential [47].

While parameters such as Nikolskii-Eisenman coefficients for relative selectivity are useful, testing for this particular dataset simply compared molarity of cationic salts, in solutions of identical pH level (as measured by a commercial glassy probe), to deltas in output potential. Two different solutions were chosen: one composed mainly of NaCl, and one composed of a number of chemicals representing human sweat. The NaCl bath was chosen to examine a neutral salt with cationic effects in the middle of the range; Na has a higher effect than K but lower than

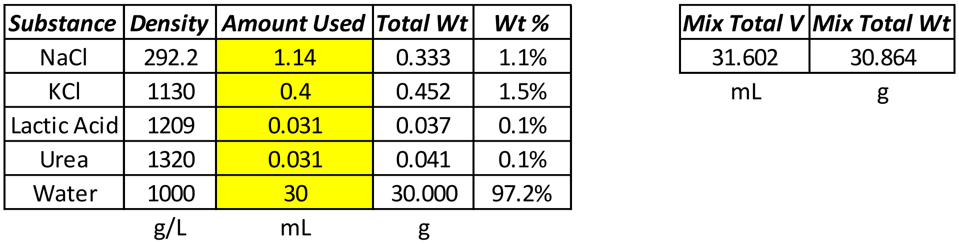

Substance	Density	Amount Used	Total Wt	Wt %
NaCl	292.2	1.14	0.333	1.1%
KCl	1130	0.4	0.452	1.5%
Lactic Acid	1209	0.031	0.037	0.1%
Urea	1320	0.031	0.041	0.1%
Water	1000	30	30.000	97.2%
	g/L	mL	g	

Mix Total V	Mix Total Wt
31.602	30.864
mL	g

Figure 37- "Sweat" solution mix, adapted from [10]

Li [48]. A "human sweat" solution was chosen to demonstrate the probe's potential usefulness as a biomedical wearable, outside of its original intention as a water quality device.

Based on [10], the "sweat" solution was mixed in ratios as shown in Figure 37. The urea and lactic acid used were both commercial solutions (#17-1319-01, *GE Healthcare Bio-Sciences, Pittsburgh, PA* and #334380, *Sigma-Aldrich, St. Louis, MO*, respectively). Once the solution was mixed, small amounts of NaOH were added with a micropipette to set the solution pH to 6.5.

Flexibility was tested by running the sensitivity tests as described above while the probes were secured to fixtures of varying radii. Parametric 3D modeling software FreeCAD (www.freecadweb.org, published under LGPL) was used to model angled fixtures for this testing, and they were printed using 1.75 mm polylactic acid (PLA) filament (3D Solutech). The fixtures and fixturing method are shown in Figure 38. Four probes were used, all coated in the same batch;

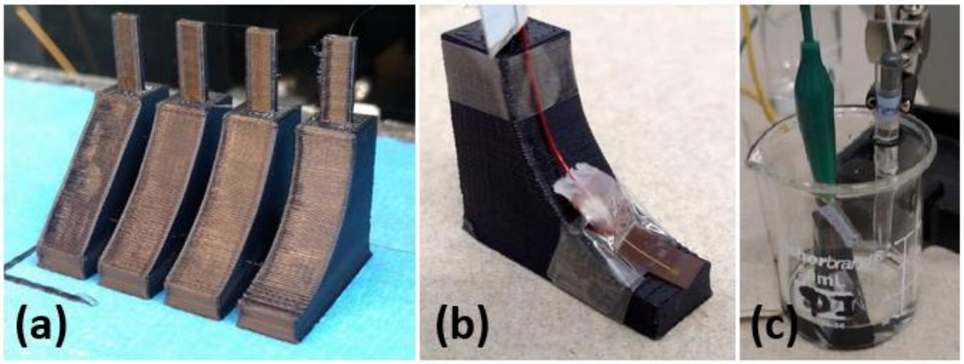

Figure 38- Flexibility testing. (a) printed PLA fixtures; L>R: 0°, 30°, 45°, 90°. (b) probe attached to 90° fixture. (c) fixture and probe in test bath.

three probes were tested in some degree of curvature as well as zero curvature, the fourth was tested with a zero curvature fixture only to act as a control.

3.3 Testing Setup

A voltage buffer with regulated input was established to amplify and measure the voltage across the WE and RE, similar to earlier layouts from [5]. A commercial ADC and logger (USB-6000, National Instruments, Austin, TX) was used to power and log the sensor output voltage to a computer, simultaneously. The diagram for this circuit is shown in Figure 39. Starting from the left, a voltage reference is used to supply an offset to the RE in the event that negative potentials are seen when the buffer solution is highly basic; in the configuration shown, the passive voltage divider supplies ~0.5 V to the RE. Next is the cell itself; in simplest form, this can be modeled as a simple voltage supply, shown in (a). To be more precise, however, the cell output should contain some ambient noise as induced into the circuit's wires and traces; this was initially modeled at 60 Hz noise but grew to encompass some high frequency noise as discussed in the chapter on integration. Also, electrochemical cell behavior contributes a number of complex impedance factors, as shown in the center of (b). What is shown is known is a Randles cell, which is a simplified representation of several of the mechanisms occurring at the electrode-solution interface [15]. These involve capacitance due to ionic layer formation (as shown in Figure 35), both resistance and capacitance due to the speed of diffusion processes, and resistance to charge transfer. Finally, the right side features a buffer and gain stage built around the LMP7721 op amp (*Texas Instruments, Dallas, TX*), which was chosen due to its extremely low bias current of 3 fA. This was chosen in order to prevent current passage through the electrochemical cell and allow Faradaic processes to take place or, in the worst case, to reduce and degrade the IrOx thin film. Based on ideal op-amp rules nodal voltage analysis, it's easily found that the buffer gain is $G =$

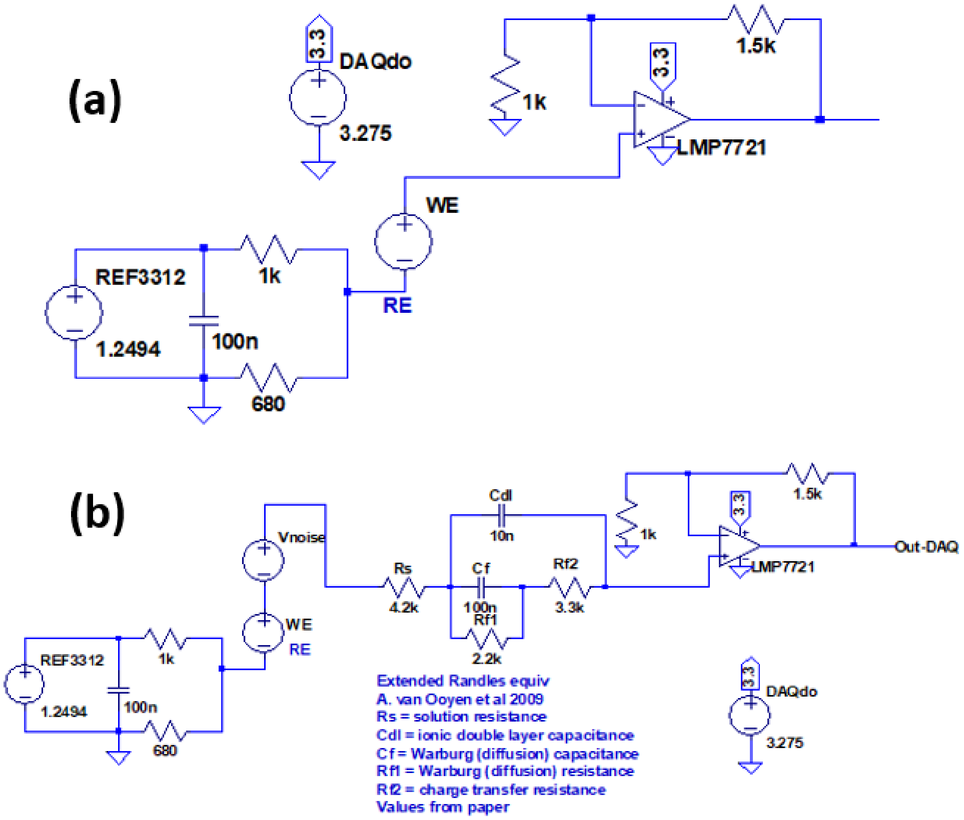

Figure 39- Buffer and amplifier circuit with voltage offset to RE. Modified from [5]. (a) cell modeled as simple voltage source. (b) cell modeled as complex Randles cell, using parameters from [15].

$1 + \frac{1.5\text{k}\Omega}{1\text{k}\Omega} = 2.5$. Both the gain and offset for the circuit were varied often, depending on the intercept voltage of the probe batch.

The regulator and op-amp power supplies came from the digital output of the same DAQ unit used for logging, as noted above. Despite the SOIC and SOT sizes of the regulator, the design could be easily built on a breadboard with the help of internally manufactured breakout PCB’s. This is shown in Figure 40. As a quick test, the LTSpice (Analog Devices, Norwood, MA) models shown above were simulated and compared with the breadboarded circuit being provided with an

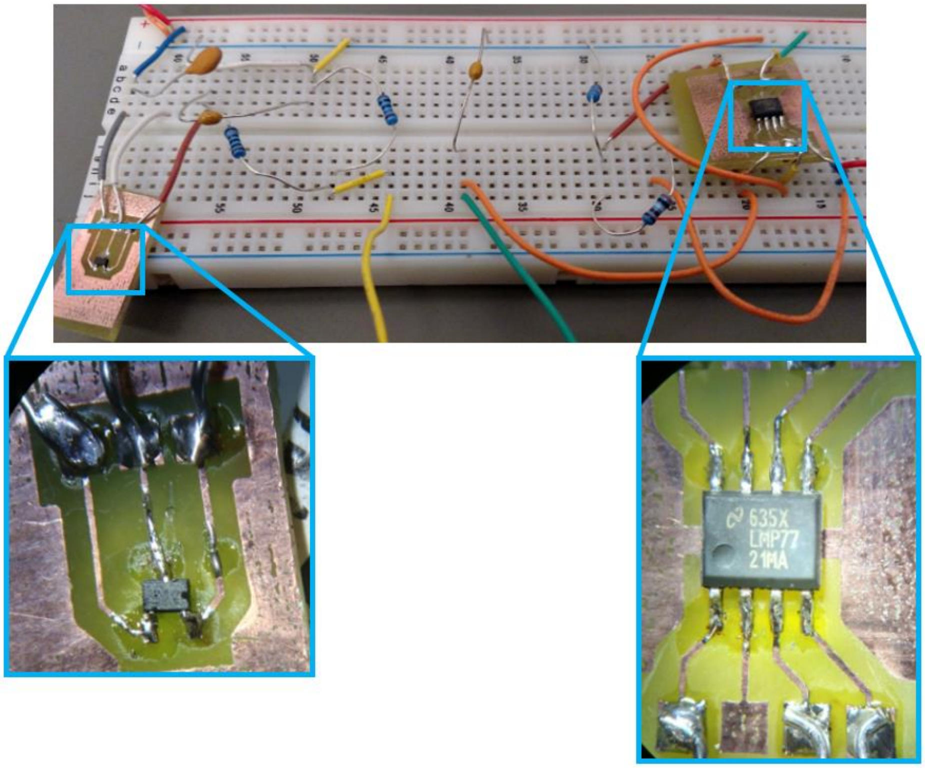

Figure 40- Breadboarded measurement circuit with custom breakout PCBs.

input voltage from a bench power supply; the result is shown in Figure 41.

Finally, the probes were attached to said circuit and cycled through baths poured into 50

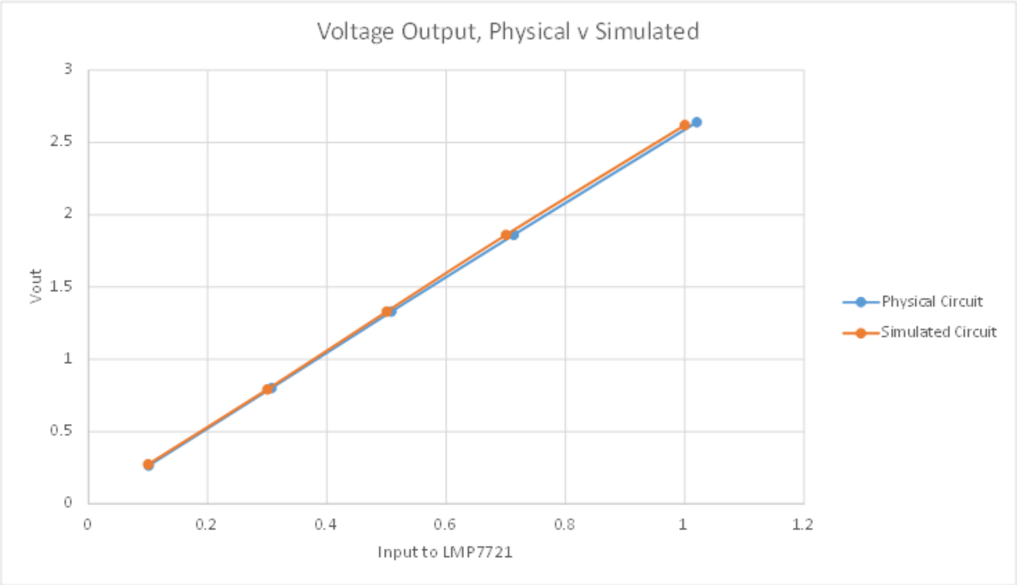

Figure 41- Circuit functionality test. LTSpice simulation versus actual circuit supplied by benchtop power supply.

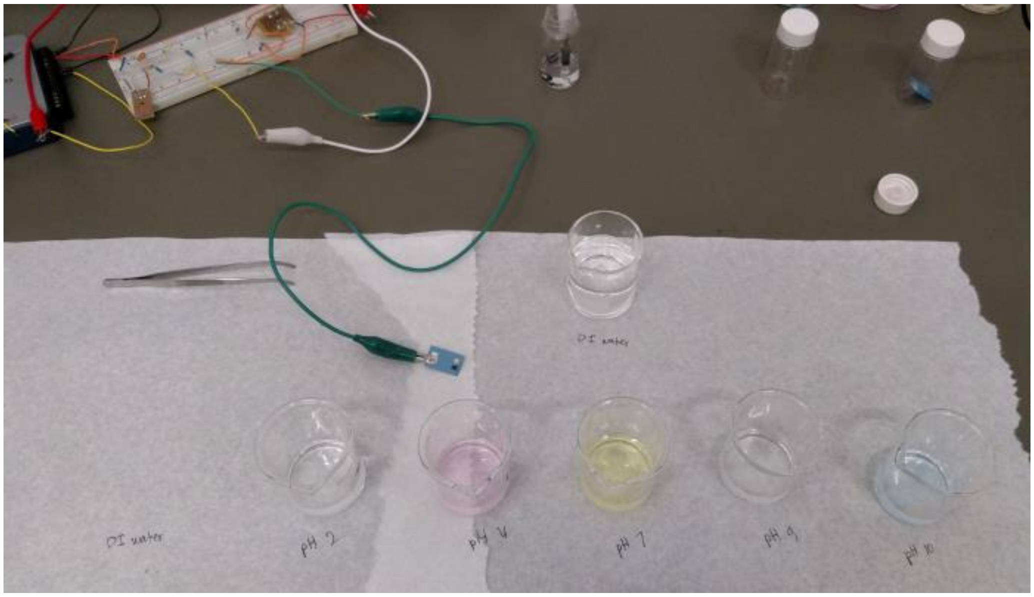

Figure 42- Example pH bath layout for testing.

mL glass beakers, as shown in and described previously.

Code for setting logging rates, buffering DAQ input, and saving to TDMS files was written in LabView (National Instruments, Austin, TX), adapted from a logging demo written by NI staff.

3.4 Characterization Results

Beyond the tests mentioned above, there will be discussion concerning the effects of CV coating parameters on probe performance and discussion of the longevity and linearity of the AgCl paste RE's, as mentioned in the chapter on material characterization, as well as discussion of the effect of probe surface area on LOD and sensitivity. Most tests performed in this section were on 1 mm^2 probes for ease of use.

Typical results for the 1 mm^2 probes follow the trend of the real time test shown in Figure 43. Results were highly repeatable and stable; with sensitivities in the 69-71 mV/pH range and of LOD ~0.040 pH. In fact, even very poor coatings typically resulted in at least ~65 mV/pH. The high degree of linearity of the probe is largely proven by the R^2 values of the linear regressions

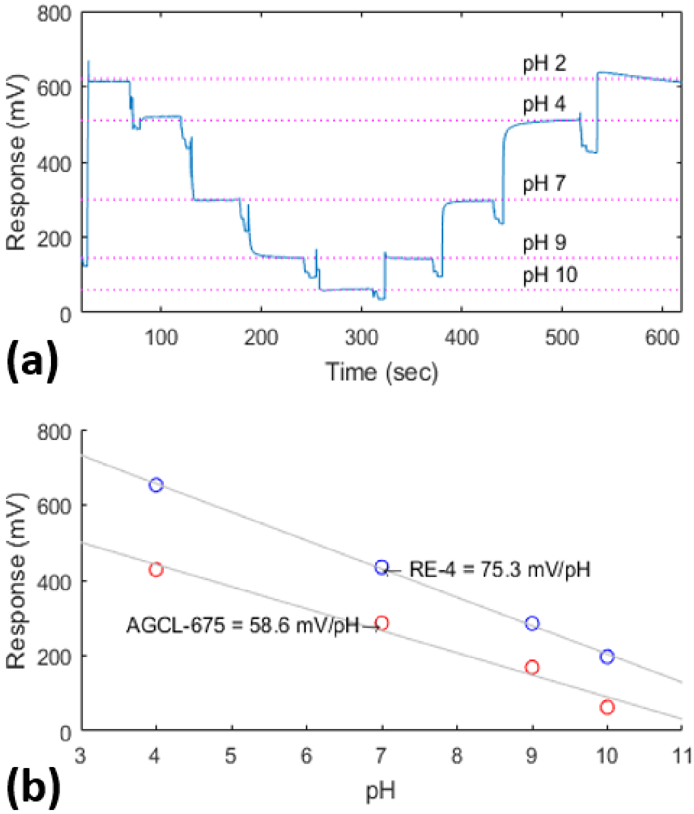

Figure 43- Example performance of 1 mm^2 *IrOx/Au probe. (a) Raw data for a 5pt buffer test, with offset subtracted and gain removed. (b) Example least squares linear regressions for 1 mm*^{2} *IrOx/Au probes versus commercial (RE-4) and fabricated (AGCL-675) reference electrodes. The slope of this regression indicates probe pair sensitivity. Figure from [8].*

performed, typically in the range of that shown in Figure 44. Instead, linearity becomes largely dependent on the RE, as discussed later.

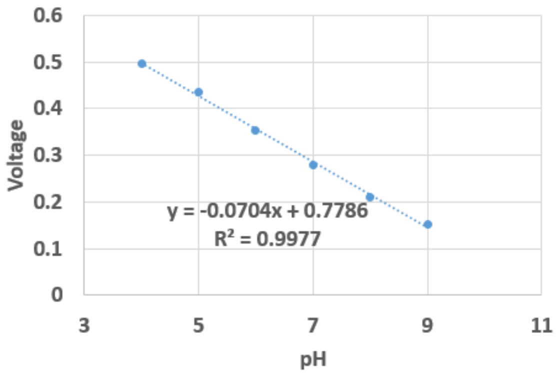

Figure 44- 6pt buffer calibration for 1 mm^2 *IrOx/Au probe produced by WNF Evatec sputtering. Note high degree of linearity.*

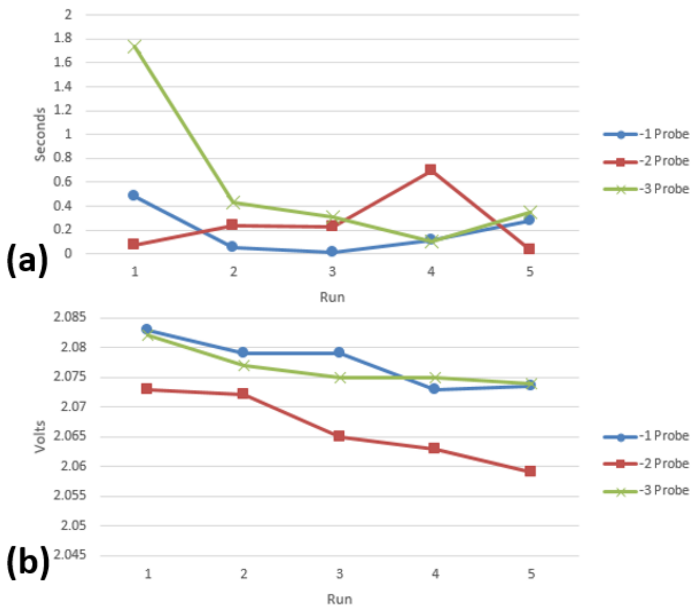

Figure 46- pH 7 response time tests. All 3 probes taken from same sputtering and CV coating batch. (a) time to 90% stabilization potential. (b) final stabilization potential.

Response time test results are shown in Figure 46. Stabilization time saw little variability,

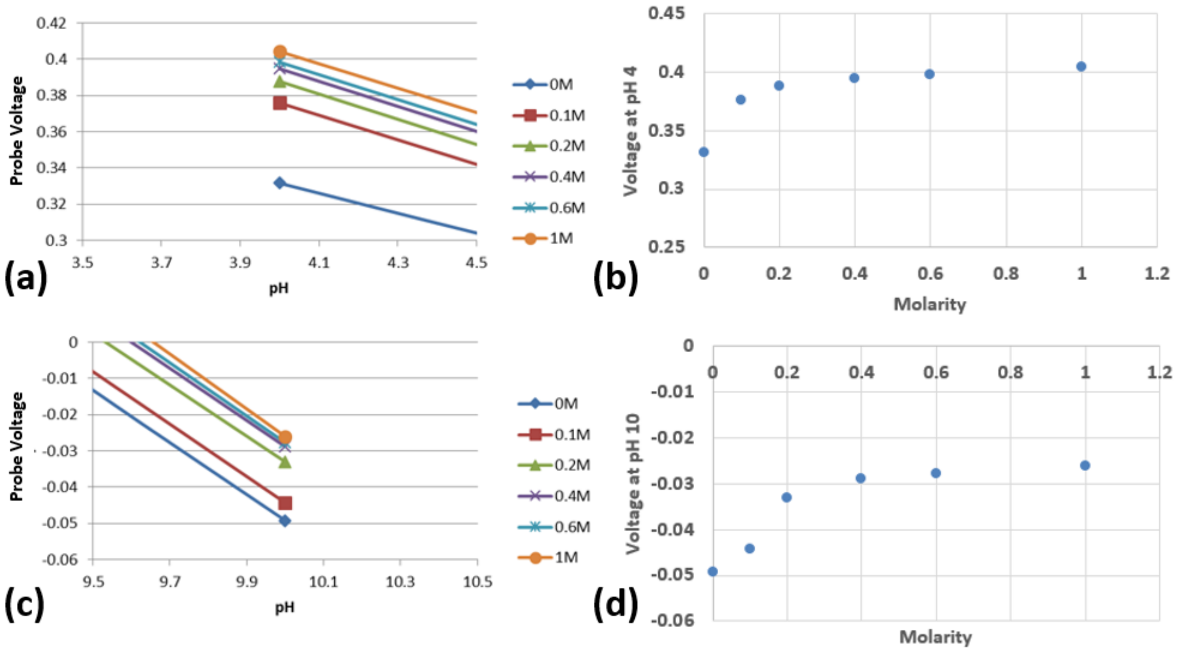

Figure 45- Selectivity of 1 mm^2 probes in various molarities of Na+ solutions. (a) output potential view at pH 4 and (b) arranged by molarity. (c) output potential view at pH 10 and (d) arranged by molarity. The relationship is logarithmic and is less consistent in basic conditions.

and averaged out to ~350 ms. As will be noted, however, stabilization voltages dropped slowly during the test period.

Per Figure 43(a) and Figure 46, as well as other tests, output variations between pH ramping and pH decrease were in the 2-15 mV range, with stabilized signals having variation of ~1 mV. Hysteresis was lower any time the 6pt bath test was used, the theory being that the HCl in the pH 2 buffer strongly reduced the IrOx thin film. As can be noted in the second pH 2 run of Figure 43(a), this buffer often produced a continuously decreasing potential as the probe was submerged in it.

Some selectivity testing results are shown in Figure 45. Both 1 mm^2 and 500 μm^2 probes were tested in pH 4, 7, and 10 baths with Na^+ molarities of 0, 0.1, 0.2, 0.4, 0.6, and 1M. At pH 4,

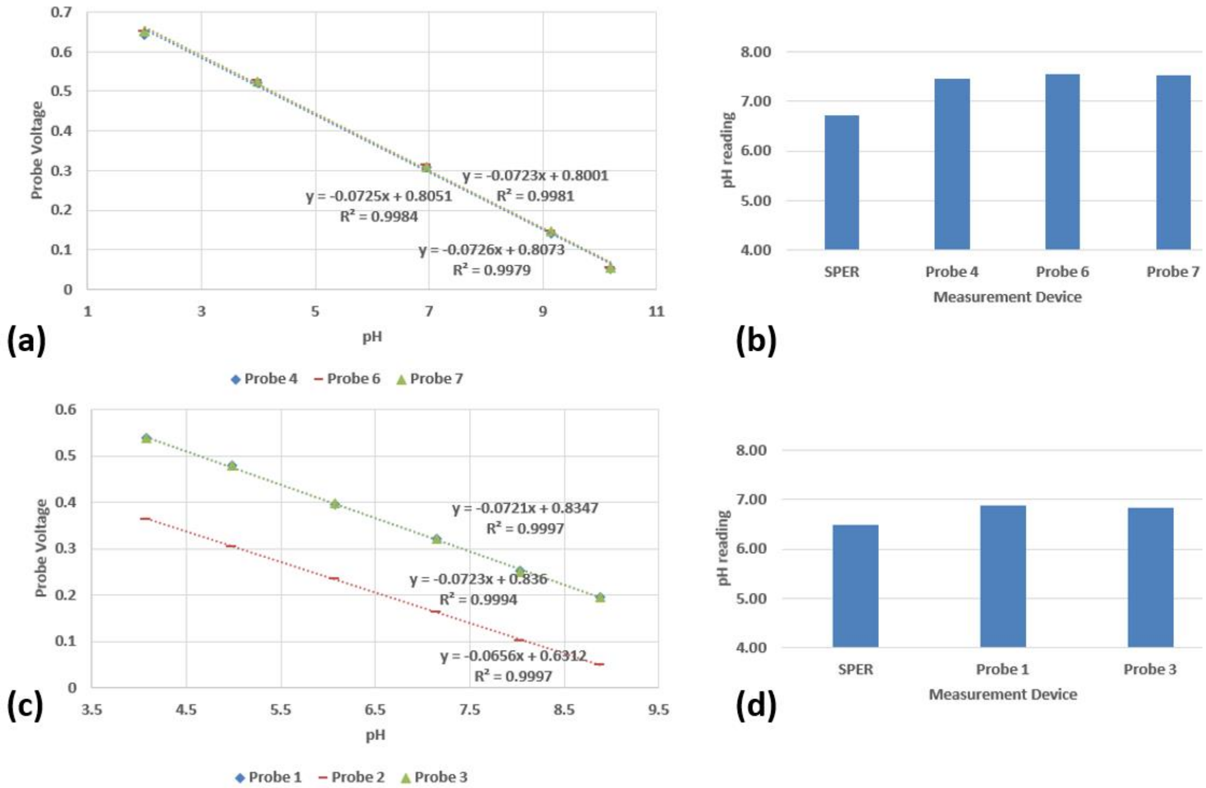

Figure 47- Bio-equivalency "sweat" test results. (a) calibration curves for probes 4, 6, and 7 and (b) their readings. (c) calibration curves for probes 1, 2, and 3 and (d) their readings. Probe 2 was excluded due to concerns about its coating.

probes typically saw a ~73 mV offset between 0M and 1M, while the offset was closer to ~25-30 mV at pH 10. It is worth noting that the relationship between cationic molarity and probe voltage is closer to logarithmic than linear, and that voltage offsets were not strictly symmetric about pH 7. It is also worth noting that the 500 µm^2 probes fared the same as the 1 mm^2 probes, thus why only the 1 mm^2 data is shown.

This test was followed up by the bio-equivalency test, also known as the "sweat" test. For this test, a commercial pH probe was used to measure the "sweat" solution's pH level, then calibrated probes were used to measure the solution pH, and the commercial and IrOx probe readings were compared. Results for this are shown in Figure 47. Depending on test batch, their reading differed by roughly 0.3 to 0.7 pH (roughly 22 to 50 mV), similar to deltas seen during the main selectivity test.

By and large, the flexibility test proved that deflection had a minor, if not negligible, affect

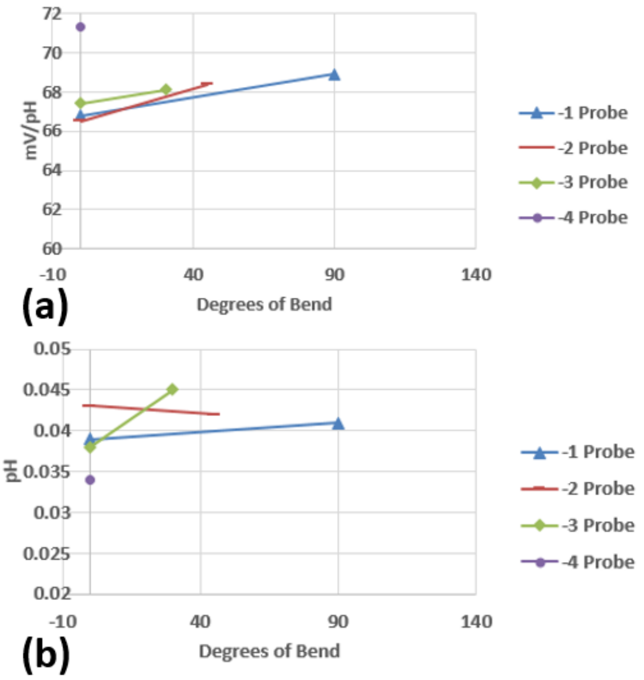

Figure 48- Probe performance with curvature. (a) sensitivity under bending conditions. (b) LOD under bending conditions. Only the -4 went through a single test, all others tested at zero degrees and at some curvature.

on the performance of the probes. As shown in Figure 48, the sensitivity and LOD of each probe were within normal variability, no matter what curvature angle they were given.

Probe surface area appeared to have an outsized effect on probe performance. As can be seen in Figure 49, while larger surfaces provide better sensitivity and LOD, an electrode size of ~300 µm2 still achieved Nernstian sensitivity. This potentially allows for significant miniaturization of the overall sensor.

Deposition parameter test results are shown in Figure 8. Altering sweep number caused the maximum cathodic and anodic current densities to vary with some proportionality; charge density rates held at between 0.9 to 1.0 µA per sweep. A nearly linear relationship was seen between cathodic activation voltage for these max currents and sweep number, varying at a rate of roughly -0.4 mV per sweep. Anodic activation voltage saw a less linear relationship, though stepping from 100 to 200 sweeps saw an increase of 0.3 mV per sweep. These parameters are shown as constants in Table I.

Sweep speed proved to have a less pronounced and/or linear effect on both current densities

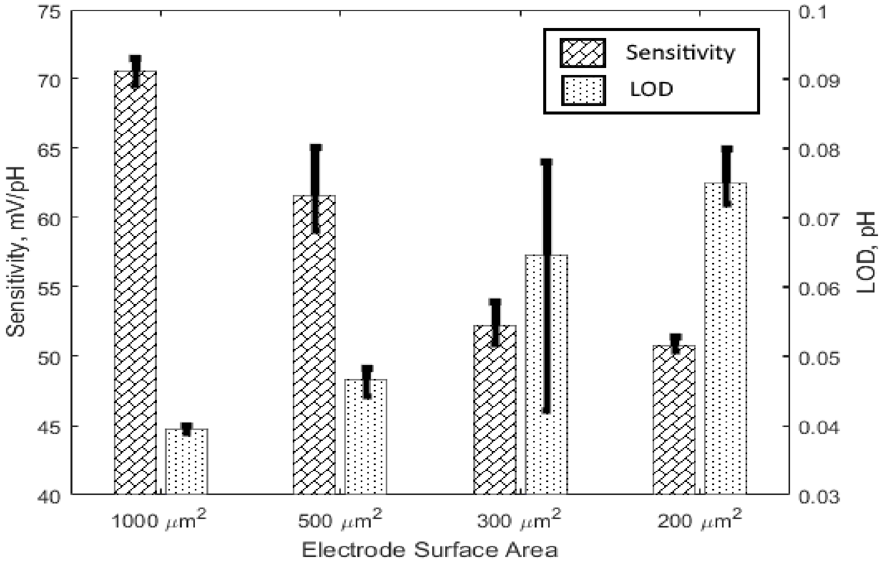

Figure 49- Sensitivity and LOD for different probe surface areas. Figure from [8].

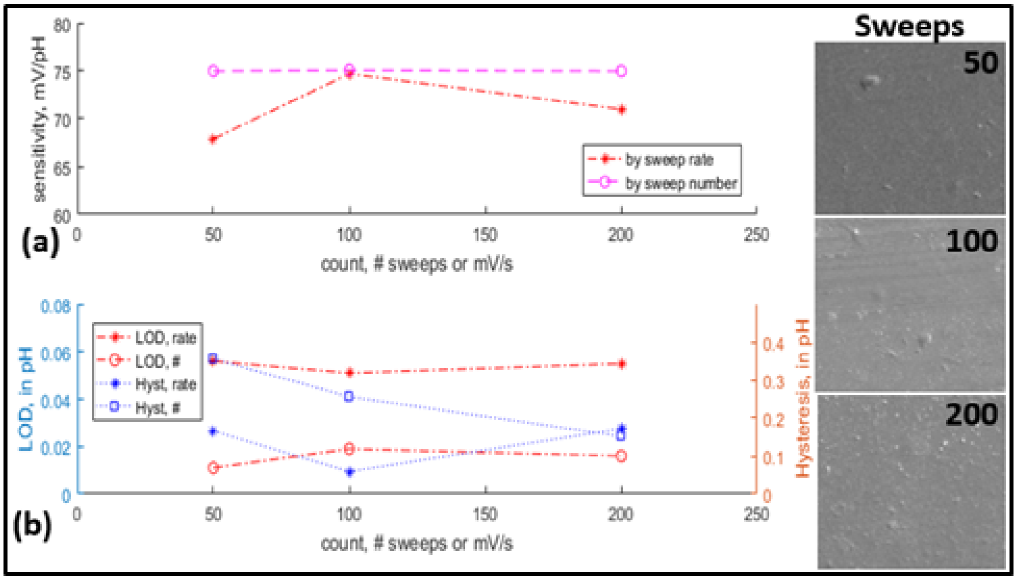

Figure 50- Performance changes in sensitivity/LOD/hysteresis as related to changes in deposition parameters. (a) sensitivity, within a single batch, as compared to varying sweep rates or sweep numbers; sweep number had no effect on sensitivity. (b) LOD and hysteresis, within a single batch, as compared to varying sweep rates or sweep numbers. Right panel shows SEM images with reference to sweep number; increases in sweep number made smoother surfaces.

and activation voltages. Activation voltages barely changed, and current density varied between 0.6 to 1.5 µA per sweep.

Pairs of electrodes were produced during each parameter sweep number test, while single electrodes were prepared from the deposition rate tests. One probe from each sweep number test pair was subjected to the pH bath calibration procedure as described previously, while another was run through SEM/EDS analysis to observe surface morphology.

As can be seen in Figure 50, calibration sensitivity was not at all related to sweep count; probes were equal to within 1 mV/pH of each other when tested together. The inset panel demonstrates that increasing sweep counts did smooth the surface substantially, however.

Sweep rate did cause a change in sensitivity but the change is non-linear. Further testing of a more discrete selection of sweep rates to determine the fit relationship may be necessary.

Both LOD and hysteresis fared differently. The standard 100 mV/s sweep rate as used by prior authors appeared, at least in this test, to be the best value for both LOD and hysteresis, providing 0.05 and 0.06 pH, respectively. While number of sweeps appeared to have little effect on LOD beyond a certain count, hysteresis saw a near-linear decrease. It is worth noting that that LOD and hysteresis of this sensor batch, while having normal sensitivity, suffered twofold increases despite matched parameters.

Clearly, significant variability can be induced in probe performance through modified deposition parameters. It appears that the best performance can be had when using a median electrodeposition rate (100 mV/s) with high numbers of sweeps (in our case, a maximum of 200 sweeps). It is possible that this 100 mV/s sweep rate is ideal due to a decrease in redox reaction rates when thicker films inhibit electron movement [35].

Improvements in LOD and hysteresis given higher sweep numbers would seem to indicate that there is a surface morphology relationship at play. Hidalgo-Acosta et. al. had previously theorized that there might be Ir oxide stoichiometry changes with changes in acid-base equilibria at the metallic film surface [36] (as discussed previously), which is supportive of our above experience in super-Nernstian behavior seen in large probe sizes. A similar mechanism may be at work in the variability of our LOD/hysteresis with respect to sweep count, as we may be seeing minor surface area changes with the decreasing roughness seen with increasing numbers of deposited film layers. It is possible that these roughness changes are altering the sensitivity along with the LOD and hysteresis, just to a much smaller degree than changes in pad size (and, therefore, possibly to a smaller degree than is detectable by our acquisition setup); further study is warranted here. Regardless, it is clear that reasonably sensitive and repeatable probes can be made in ~10-20 minute deposition cycles.

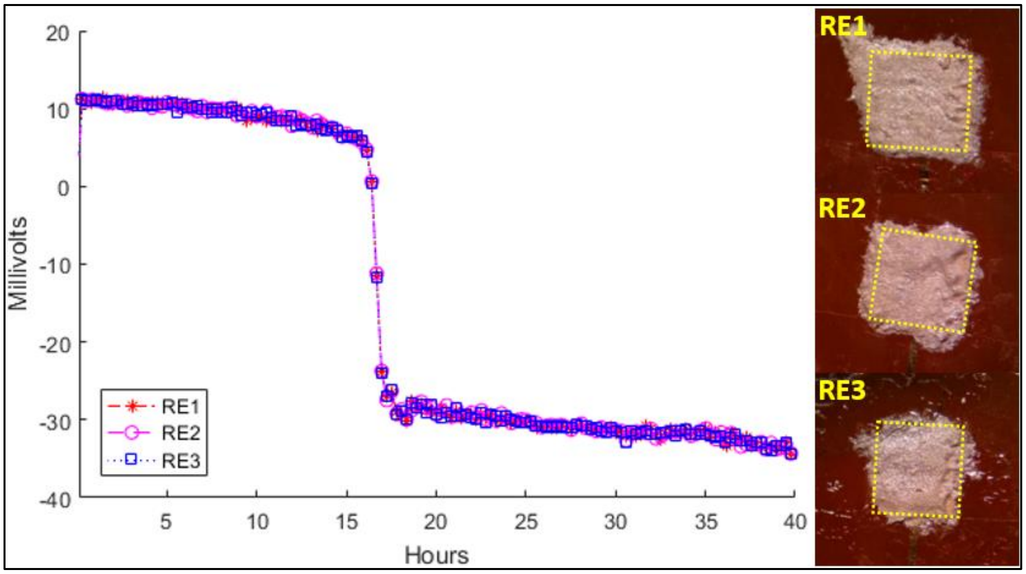

Figure 51- Custom AgCl RE Stability. Hydration response (millivolt potential change as measured against commercial RE) during approximately 40 hours of immersion in KCl solution, for three 1 mm^2 probes. Right panels shows images of three custom RE probes used to gather this data, taken after stability tests.

Lastly, custom RE's were studied in order to validate their usefulness as device references. Besides standard calibration runs, custom RE's were also studied for drift. Reference probe stability was tested by immersing fabricated probes into a potassium chloride (KCl) solution and monitoring their potential against the commercial reference electrodes mentioned previously. Electrodes were monitored at 1 Hz for up to 5 days using the same logging setup as in pH bath calibration tests. Once data was gathered, it was lowpass filtered with a cutoff of 1.5 Hz and passed

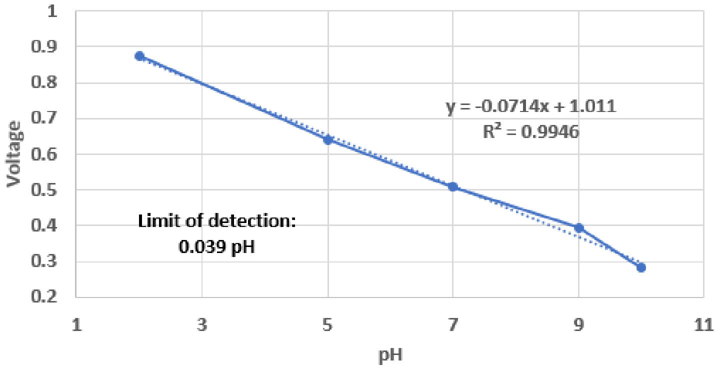

Figure 52- IrOx/Au vs AgCl-675 RE performance.

through a moving average filter with a window of 60 samples.

As shown in Figure 51, each probe tested in this fashion encountered a large potential swing (approximately 40 mV); these particular probes experienced this swing at ~17 hours after immersion. After this, the probes saw a potential variation of no more than +/-3 mV, though some linear reduction did continue. In physical inspection of the probes after testing (see inset), locations were found where the AgCl paste had completely separated from the Au substrate, leaving exposed Au. Given the time coincident nature of the hydration swing of all probes, physical apparatus agitation most likely caused the event. Similar swings were seen in other probe batches which did not experience agitation, though not in groups.

As shown in previously reported conference results, however, paste RE's tended not to feature the same linearity or sensitivity as commercial RE's. As in Figure 43(b), custom-made AgCl RE's tended to lower the probe pair sensitivity to near 59 mV/pH and cause a slight decrease in linearity. That being said, some high sensitivity results were achieved with custom RE's if applied exceptionally carefully, as shown in Figure 52.

3.5 Noise Removal

Some attempts were made to remove probe/wire motion and ambient electrical noise. Figure 53 shows some signal noise and its associated Fourier transform. Most immediately obvious is the 60 Hz noise; notably, this is only down 15 dB from the primary signal. This 60 Hz signal and its harmonics, as well as a shifted peak with 60 Hz harmonic gaps, are the most evident noise sources. In looking closer, however, there are other sources which are less well defined. Figure 54 shows other frequency components which may be "true" noise sources, or could be a combination of ADC quantization error and Fourier transform windowing methods (in other words, mathematic

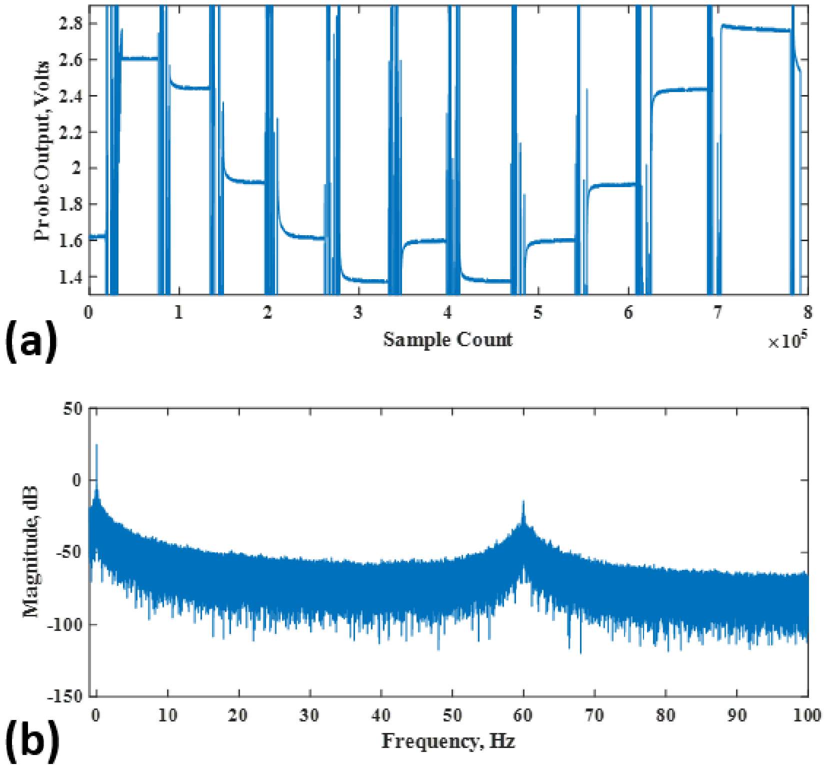

Figure 53- Analysis of noise in signals. (a) example raw data, 1 mm^2 IrOx/Au probe, 5pt test, 1kHz logging. (b) Fourier transform of raw signal, only shown from 0 Hz to 100 Hz.

artifacts).

At first, attempts were made to clean these using INA and subtraction circuits, with no

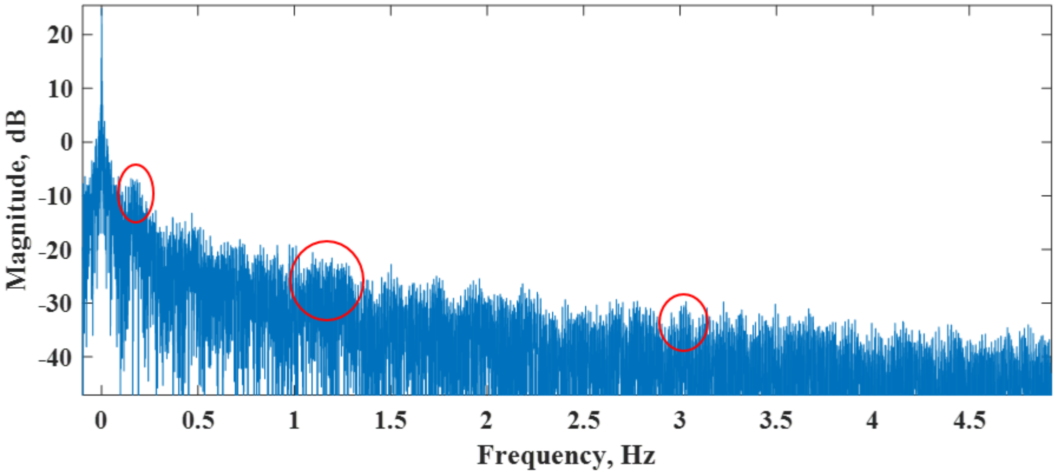

Figure 54- Highlight of potential other noise sources in test data. It is unclear whether these, and others shown, are a result of ADC quantization error and the transform windowing method or if these are "true" noise sources.

success. Most of the “noise channel” electrodes used produced signals which were significantly phased shifted and featured different spectral components, so simple subtraction produced signals of equal or worse quality (as typically measured visually by time series standard deviation) than the original inputs.

A decision was made to attempt digital means of signal cleaning. To perform component analysis, a secondary “noise” channel had to be sampled, using the circuit shown in Figure 55. This should appear to be similar to Figure 39, as it is simply the replication of the initial signal path. The only difference here is that now a secondary probe would be sampled.

At first, an AgCl probe was used as the second channel and raw data similar to Figure 56 was generated. However, the statistical coherence (as shown in Figure 58) showed little overlap between spectral densities, so this physical arrangement did not allow adaptive least mean square filters or components analysis to actually may a meaningful difference in signal cleaning.

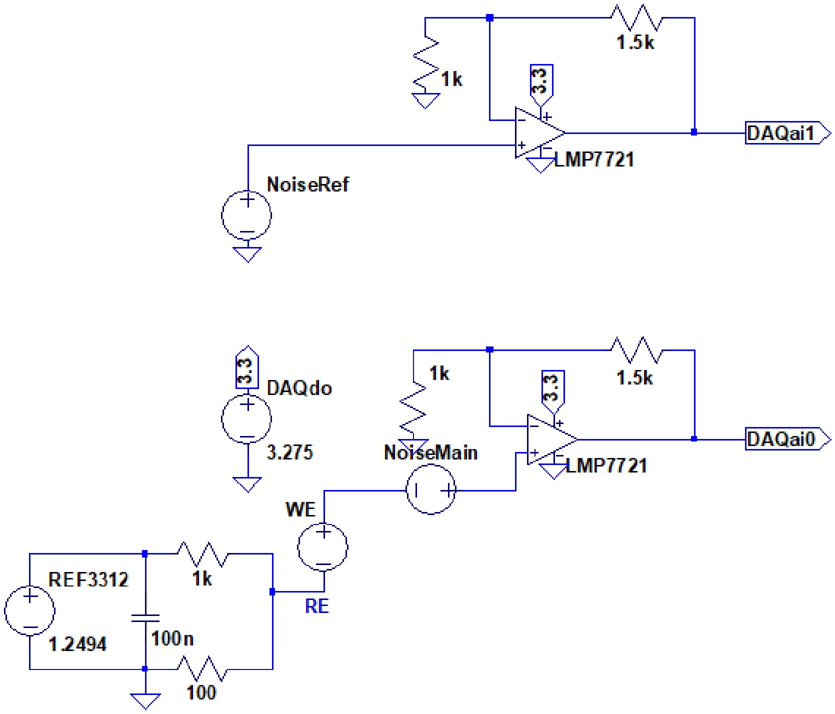

Figure 55- Dual channel "noise measurement" circuit schematic.

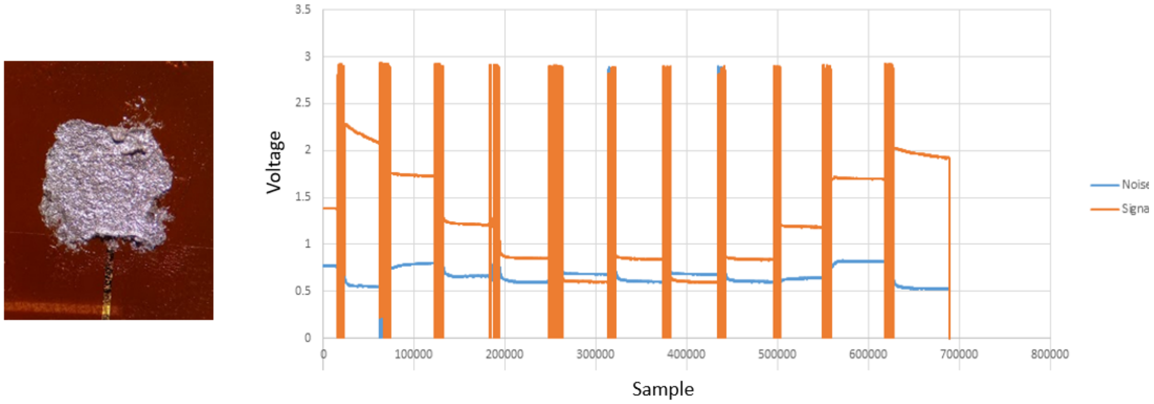

Figure 56- Example raw data from dual channel cycling, using a secondary AgCl-675 RE as a "noise" channel. Note the seemingly similar DC potential swings and consistent high frequency noise.

For reference, the magnitude squared coherence is found as

$$C_{xy}(f) = \frac{|P_{xy}(f)|^2}{P_{xx}(f)P_{yy}(f)} \qquad \textit{Eq. 11}$$

Where $P_{xy}(f)$ is the cross-spectral density of signals x and y, and $P_{xx}(f)$ and $P_{yy}(f)$ are the power spectral densities of signals x and y, respectively. This was implemented using the *mscohere()* function in Matlab (The Mathworks, Inc., Natick, MA).

In changing the secondary RE for a secondary IrOx probe, a secondary signal with more closely magnitude and phase matched noise was realized. After attempting a few other methods, the most promise was realized when using independent component analysis, a form of blind source separation. In brief, this functions by finding the "mixing matrix" between a set of input signals and an unknown source by maximizing statistical independence [49]. The package of algorithms used for this work is known as FastICA (Helsinki University of Technology).

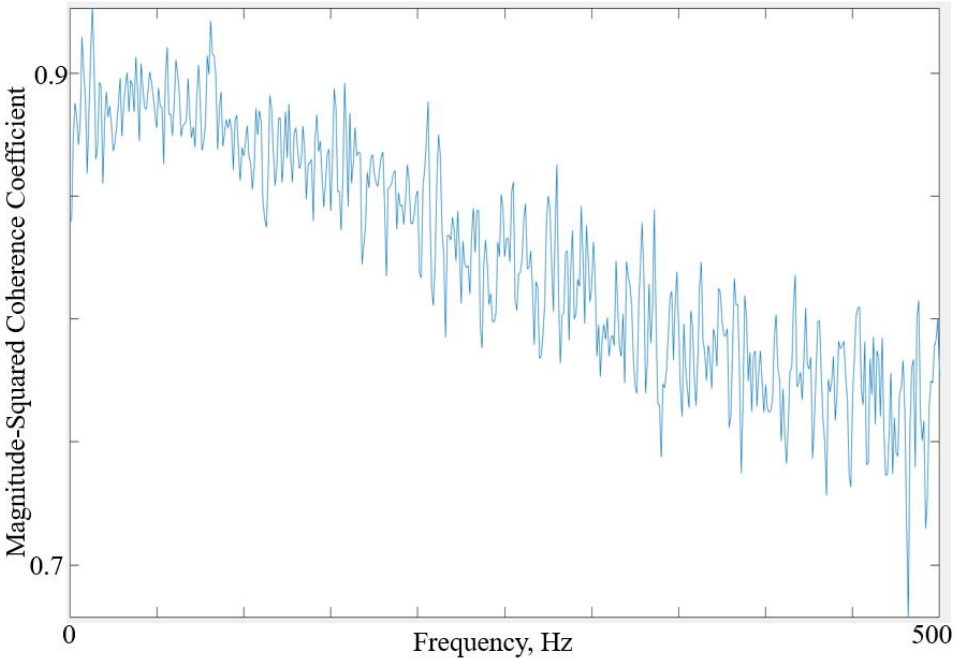

Figure 58- Statistical magnitude-squared coherence across the frequency spectrum 0 - 500 Hz, as calculated between the main signal and the "noise" signal originiating from an AgCl-675 RE. No obvious coherence exists between their spectral densities.

The FastICA algorithms were able to operate successfully and display independent source components. However, despite being able to visually see some noise removal occurring in the signal (see Figure 57), the standard deviation of the main signal channel was largely unaffected by the process (see Figure 59); there didn't appear to be a large change, so SNR and associated statistics were not calculated. The failure here most likely stems from the fact that ICA algorithms

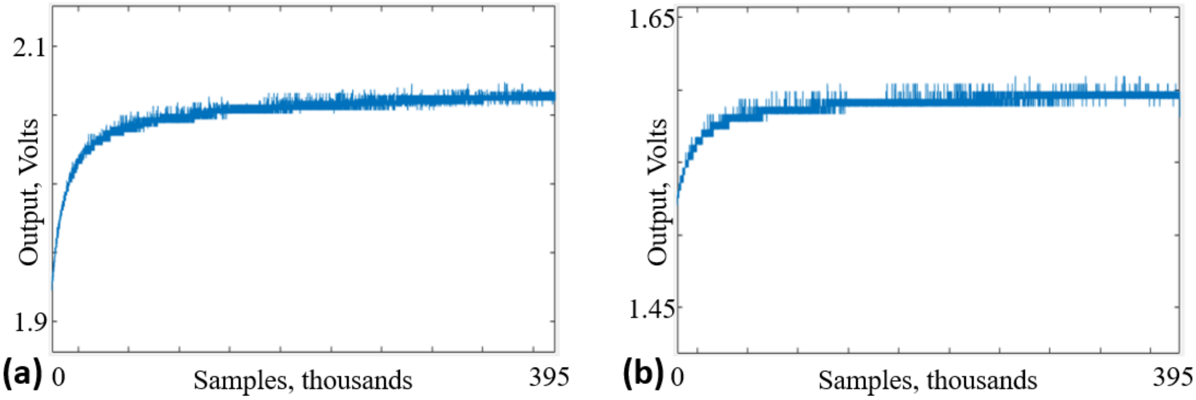

Figure 57- Signal channel before (a) and (b) removal of noise by independent component analysis using the FastICA package. "Cleaned" signal is equal to or worse than original.

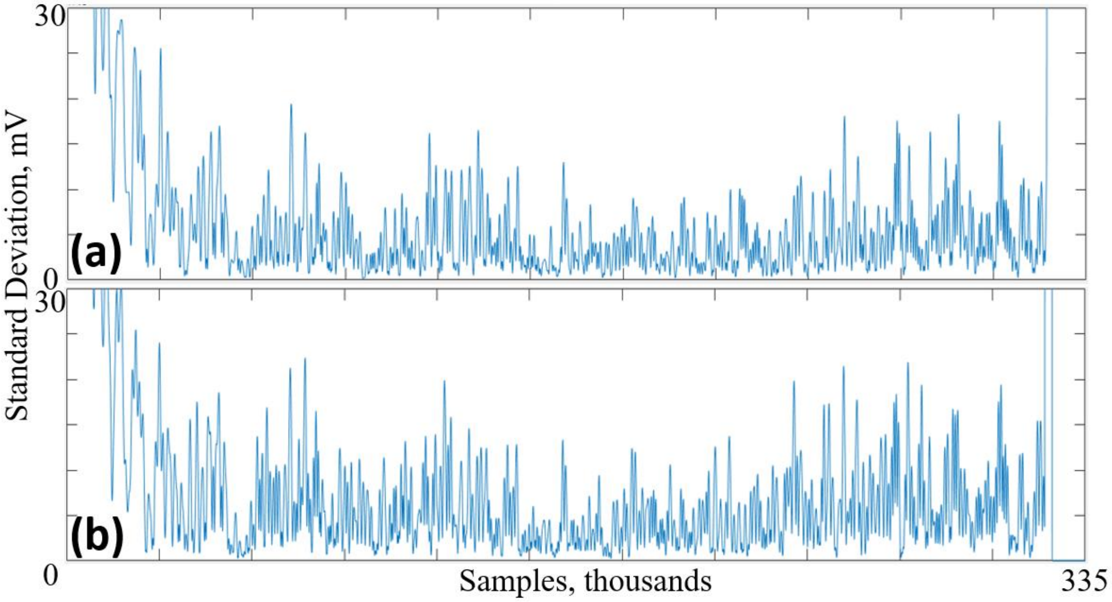

Figure 59- time series standard deviation of the signal channel, over time, before (a) and after (b) signal cleaning by ICA.

assumes that the input sources are linear and independent [49]. It is unclear if this is the case, as the combined power supplies between each channel's buffer, as well as the complex electrochemical kinetics inside the cell, threaten their independence. Indeed, Pearson correlation coefficients between the two input channels, even in the IrOx vs IrOx vs AgCl configuration, was typically no better than ~0.85; initial datasets came to ~0.57. A simple low pass filter is likely all that will be effective with these signals, given their largely DC nature.

3.6 Automatic Characterization

Short Matlab scripts were written to speed the process of analyzing buffer test data, given the large amounts of it being generated. The script operates in the following order:

- The raw data's standard deviation is calculated over a user defined window size, typically no less than 3 samples when sampling at 10 Hz
- Raw data is filtered by a standard deviation threshold as defined by the user, typically

slightly larger than the DAQ’s ADC quantization limit

- Sections of data are given pH level labels by segmenting data around “dropouts” (periods where the signal is 0 for a user defined time length) and iterated over by a user supplied vector of test points
- The data’s first derivative towards the end of its data window is used to indicate data stabilization, and an average value is taken over several seconds
- The slope of a linear least squares regression of the observed output vector yields the probe sensitivity
- Data windows which were averaged to produce the output levels above are now used to calculate LOD and hysteresis as defined earlier in this chapter
- All values are displayed to the user in graphical form

Some manual tuning is required at the moment, as raw data can vary widely based on the

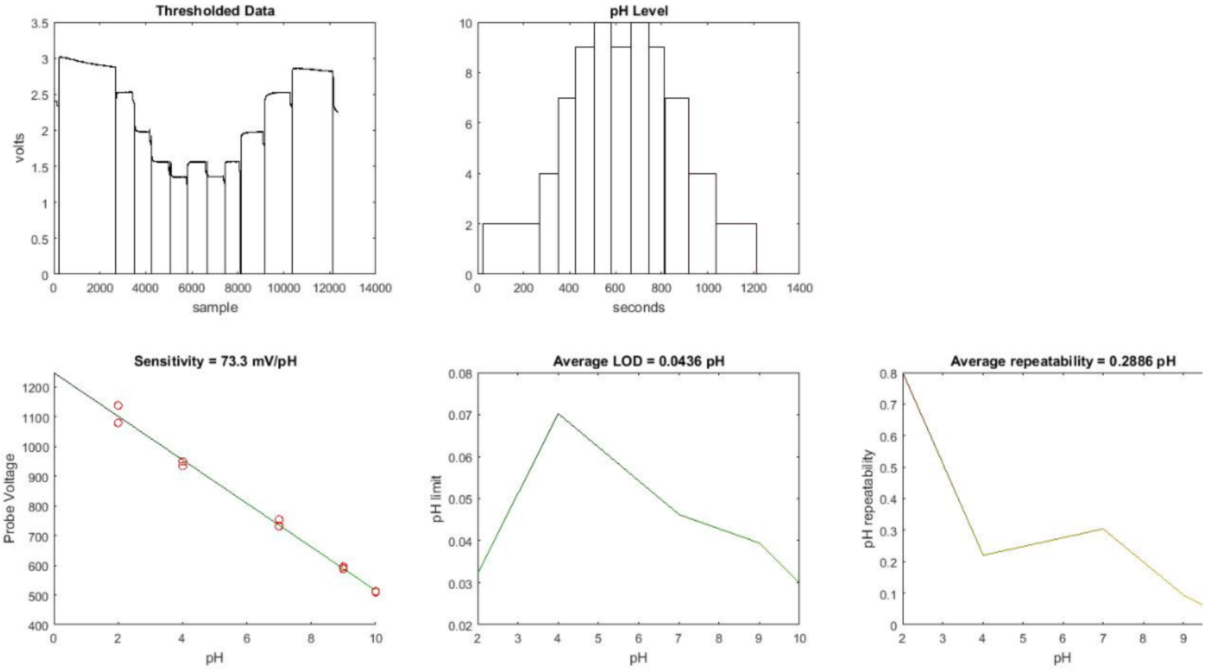

Figure 60- Graphical output from Matlab scripts. Note that thresholded raw data and pH level binning is shown alongside output parameters.

cadence of testing, the circuit configuration, and the logging rate. An example output is shown in Figure 60 and the code is supplied in an appendix.

4. Integration and Manufacturing

This chapter focuses on the work done to integrate the main work, Iridium Oxide and Silver Chloride electrodes, into complete devices which can meet real world sensing requirements.

4.1 Low-Temperature Co-fired Ceramic (LTCC) Circuits

This work sprang from research lead by a previous grad student [5]. In it, an LTCC-based wireless pH sensing system was designed for use in environmental and food-safety monitoring. As in this work, the working electrode was fabricated by electrodeposition of IrOx. In contrast, the

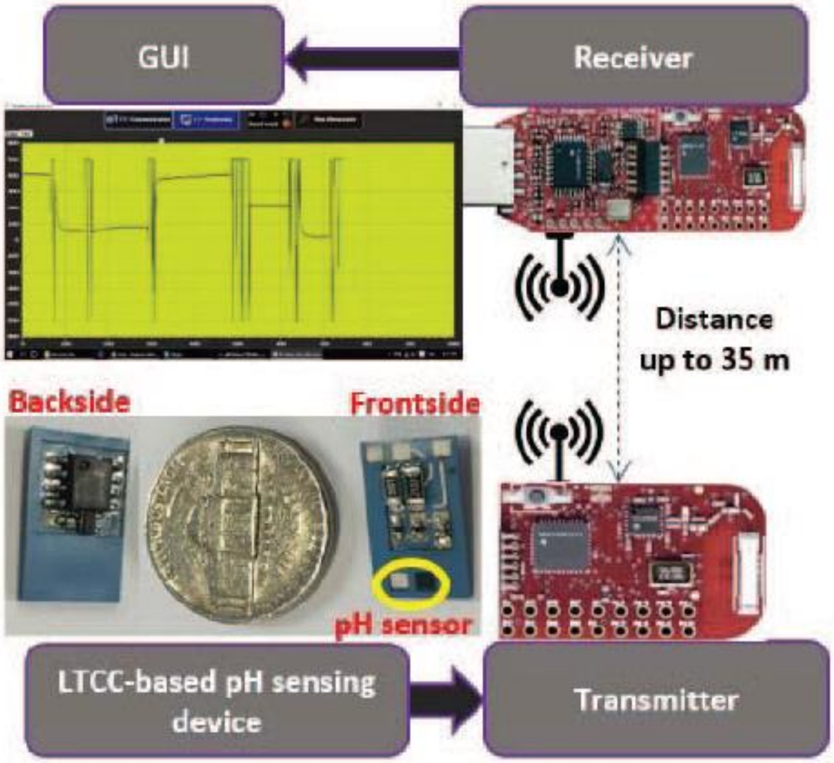

Figure 61- LTCC-based wireless pH system as demonstrated in [5]. Note commercial wireless transmission in concert with custom GUI's and electrodes.

reference electrode formed directly onto an Ag surface during the LTCC fabrication. As this system was also intended to be wireless, a proof-of concept system made use of the wireless module EZ430-RF2500 from Texas Instruments. The pH data was transmitted to a PC-based receiver. The system is shown in Figure 61. The main intention here was miniaturization and package integration, rather than biocompatibility and conformability.

The forming process for the LTCC base used four 951AT ceramic layers (DuPont, Omaha, NE) as a substrate, with a standard LTCC fabrication process following as shown in Figure 62. This process will not be discussed in detail here; it will suffice to say that stacked circuit traces could be encapsulated within a protective ceramic shell, thereby only exposing component pads (which would later be covered in protective polymers) and sensing locations.

As mentioned prior, the RE in these devices was printed with Ag/AgCl paste during the serigraphy process. Initially, this method was chosen to increase AgCl paste thickness relative to Ag layer chlorinating methods in solution. This increased thickness was expected to increase durability, though the materials chapter of this report indicates that that may not have been the case.

The wireless module chosen, the EZ430-RF2500, was chosen for its low power usage, its inclusion of a common MSP430 microcontroller, and a CC2500 2.4 GHz wireless transceiver. The manufacturer reported RF transmission ranges of up to 35m in nominal conditions. The previous

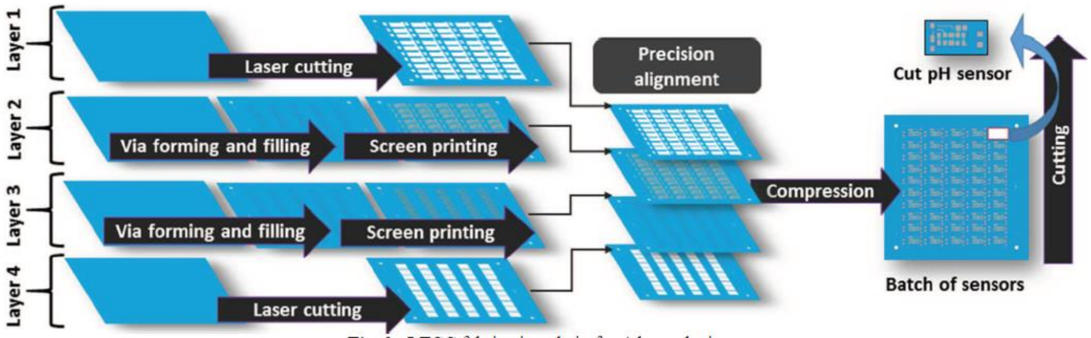

Figure 62- Standard LTCC fabrication process. Taken from [5].

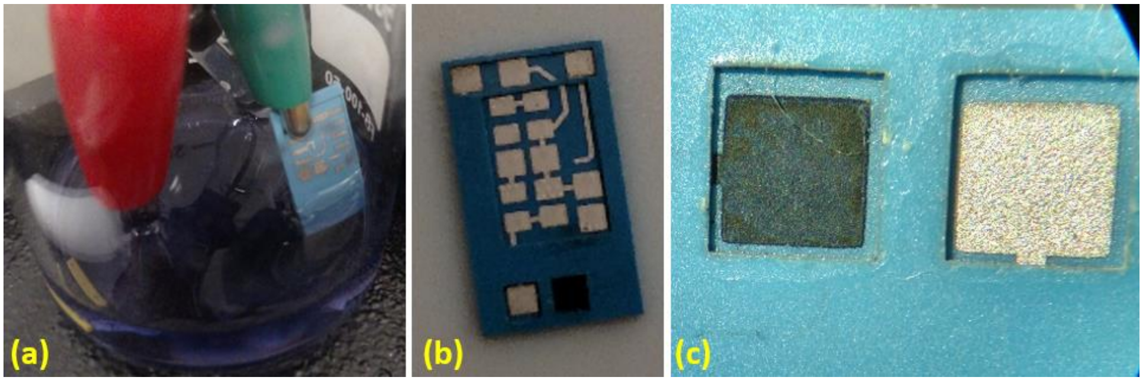

Figure 63- IrOx electrodeposition as applied to LTCC-based devices. (a) clamp attachment method in solution. (b) IrOx applied to "bare" LTCC circuit. (c) closeup of deposited IrOx (left) and original AgCl paste RE (right).

research lead developed a graphical user interface using Visual Studio (Microsoft, Redmond, WA) to display and store data. Code for this application is not included here and should be sourced from the relevant author's thesis.

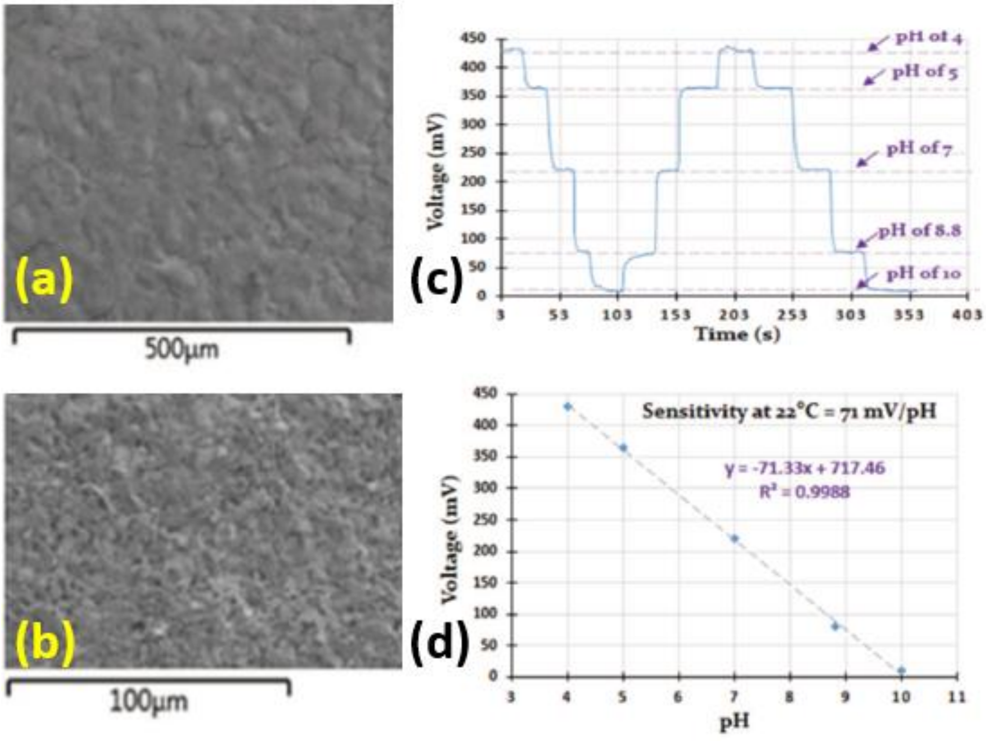

Figure 64- LTCC probe surface and performance. (a) IrOx electrodeposited surface SEM image. (b) AgCl ink surface, SEM image. (c) raw pH test data as recorded across the wireless link. (d) sensitivity calculation from raw data; note sensitivity of ~71 mV/pH.

Electrodeposition typically took place as shown in Figure 63(a). The attachment method benefited from simplicity but connection strength tended to be variable.

Once deposited, the IrOx film was characterized using scanning electron microscopy (SEM) and energy dispersive spectroscopy (EDS). EDS results showed highly uniform material distributions; SEM images are shown in Figure 64. The results here confirm earlier findings: namely, that cell linearity was mainly dependent on the quality of AgCl paste application and that sensitivity is largely independent of substrate. This is a highly positive result, as it suggests that this manufacturing method and oxide layer can be applied to any sufficiently conductive material.

Wireless test results are also shown in Figure 64; performance is super-Nernstian, at ~71 mV/pH. The LOD came to ~0.054 pH. While this is lower than the typical LOD of the polyimide samples prepared, there is almost certainly some signal loss and decrease in SNR due to wireless transmission. This was not quantified.

4.2 Wireless Sensing

Several different wireless signal transmission methods were attempted. First, a load-based amplitude modulation (AM) scheme was attempted with wireless power transfer. Second, in an attempt reduce current flow through the pH sensor, a buffered load-based frequency modulation scheme was attempt with wireless power transfer. Finally, a locally-powered ADC-to-Bluetooth transmission was used to provide a proof-of-concept demonstration.

4.2.1 Amplitude Modulation Scheme

The amplitude modulation scheme was produced by earlier researchers [9], themselves following earlier work [50], and was intended to function as simple load modulation reflection of the input wave. In the paper detailing its design, testing of the circuit's efficiency is discussed

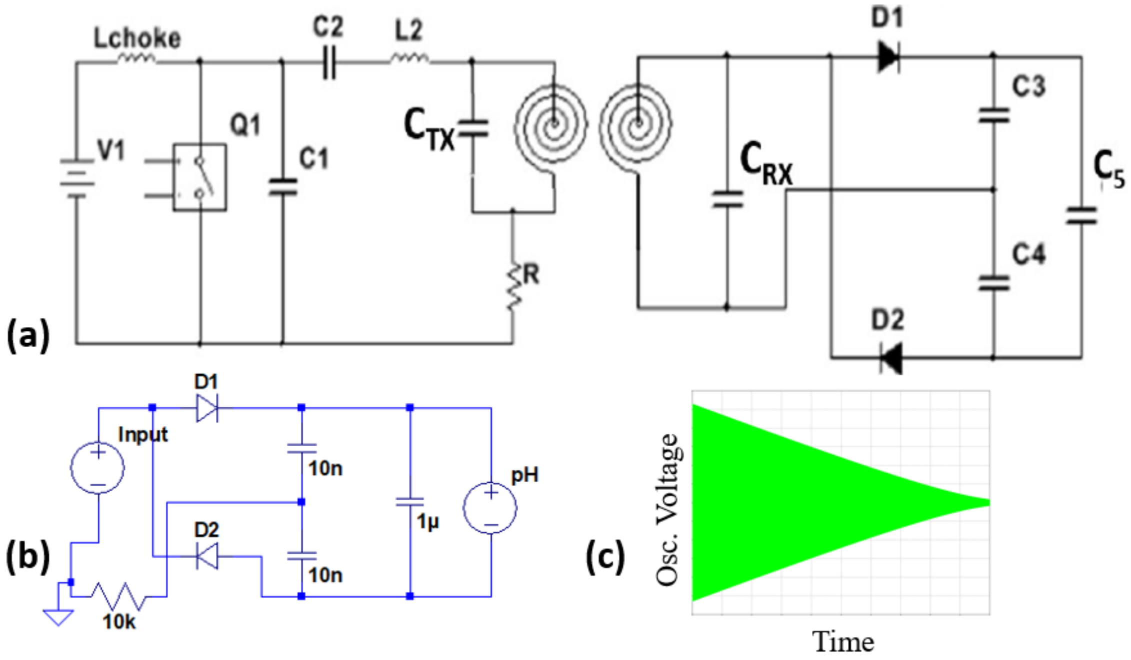

Figure 65- Analog amplitude modulation scheme. (a) Rx and Tx design as taken from [9]. (b) simplified Rx side for demonstrative purposes. In this layout, supply "Input" replaces signal coming from Rx planar coil in (a) and 10kΩ resistor exists only to act as a load for simulation probing purposes. (c) simulation output at 10kΩ resistor given a 1 MHz sine wave at "Input" and rising DC voltage at "pH". Note the amplitude change in the returned signal.

thoroughly and will not be reproduced here. Instead a brief discussion of the overall design and results will follow.

In the configuration shown in Figure 65, our load is assumed to be placed across C5. However, the load in this case, the pH probe pair placed in solution, actually functions as a voltage source. In this way, the load's changing potential alters the amplitude of the returned wave being passed between the 10nF capacitors. This works for simulation purposes but, in practice, the scheme allowed for significant current passage through the pH probe pair; during this event, IrOx films were entirely removed from the Au layer. It is unclear exactly how much current passed, but CV results from earlier chapters indicate that 10's of µA and/or voltages exceeding +/-0.7V may be enough to reduce the oxidized layer.

Also, as mentioned in the chapter on probe characterization, the Randles cell approximation of the electrochemical cell tells us that the cell carries resistance and capacitance of its own. Based on the parameters assumed from [15], capacitance of the cell may be 100nF or more. This means that, even if the probes had survived, unforeseen kinematics could be produced. Only electrochemical impedance spectroscopy could have determined these effects, which was not performed.

4.2.2 Frequency Modulation Scheme

Next, an FM scheme was attempted in order to take advantage of the voltage controlled oscillators (VCO) which are typically a part of these designs. As a note, the designs attempted herein do modify the *amplitude* of the incoming signal but do so in a frequency-dependent manner. Since the amplitude of the returned signal is not the parameter of interest, but the frequency of the modulation, this was still termed an FM scheme.

The FM scheme was used so that the probe pair output would be buffered and converted to another analog signal type. As an added benefit, FM transmission means that the signal does not need to be calibrated for antenna gap, as frequency count is not dependent on signal transmission efficiency.

An example of a full FM scheme is shown in Figure 66. In this configuration, an RF signal is transmitted across inductively coupled coils and rectified, similar to the AM scheme except that the probe will modulate the amplitude of the retransmitted wave by a fixed amount but variable frequencies. This is typically done by including an oscillator in the signal path whose frequency is controlled by the transducer. In our application, a voltage controlled oscillator (VCO) is the modulator of choice.

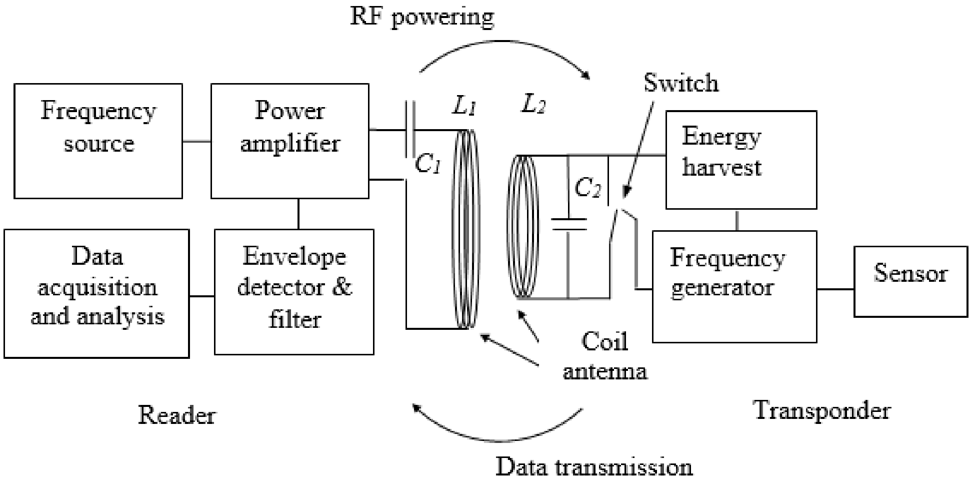

Figure 66- FM power and communication screen, as taken from [11].

An early version of this, as designed in [3], featured the LTC6900 (Analog Devices, Norwood, MA) VCO IC. It was also initially set up in a current controlled fashion (Figure 67(a)), which was not immediately realized. Therefore, testing took place while the VCO was drawing current through the IrOx probes. A combination of this fact and possible contamination of one of the pH buffers meant that a highly nonlinear result was achieved across the inductive link, as

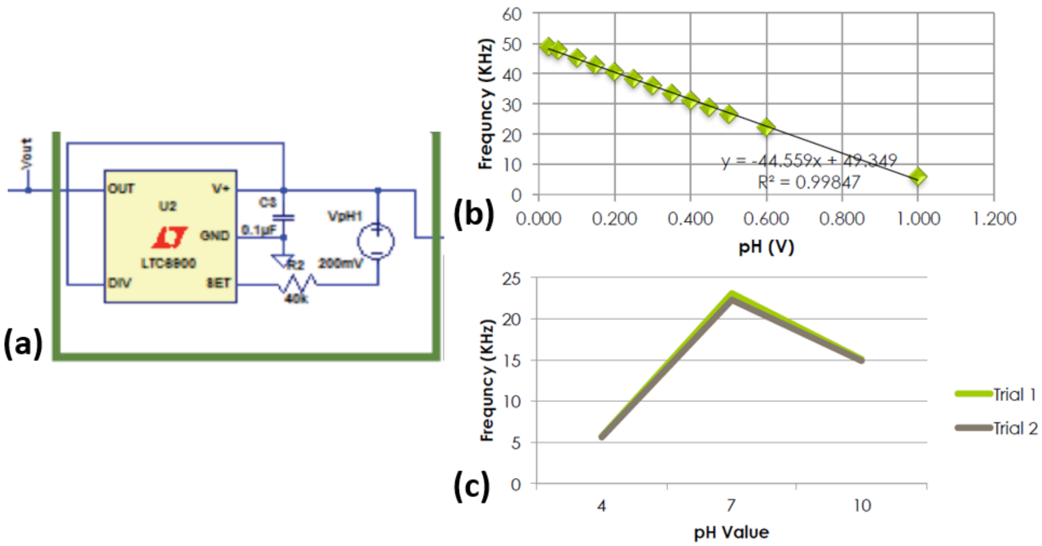

Figure 67- Early VCO design and results, as taken from [3]. (a) VCO layout; VpH1 = pH probe pair. In this case, the pair was fabricated on top of PCBs. (b) VCO output as tested on a breadboard using a variable power supply. (c) actual modulated envelope readings on Tx side during 3pt (pH 4, 7, and 10) probe calibration. Note the highly nonlinear relationship.

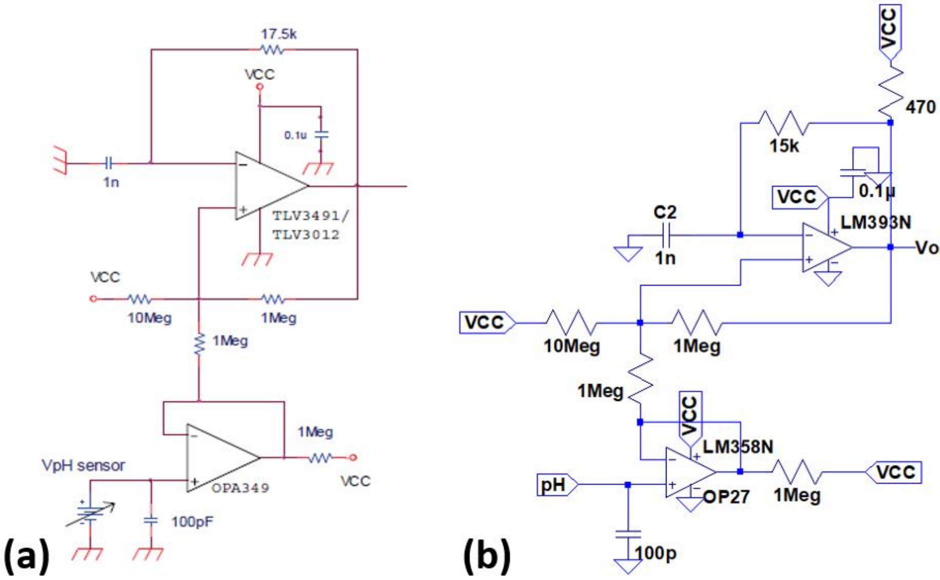

Figure 68- Buffered relaxation oscillator design. (a) original design from [1]. (b) design modified to make use of other op amps and pull-up resistor.

shown in Figure 67(c). In later testing with different planar antenna sets, the choke inductor was burned and some damage was caused to the class E amplifier, so the opportunity was taken to experiment further with the circuit design.

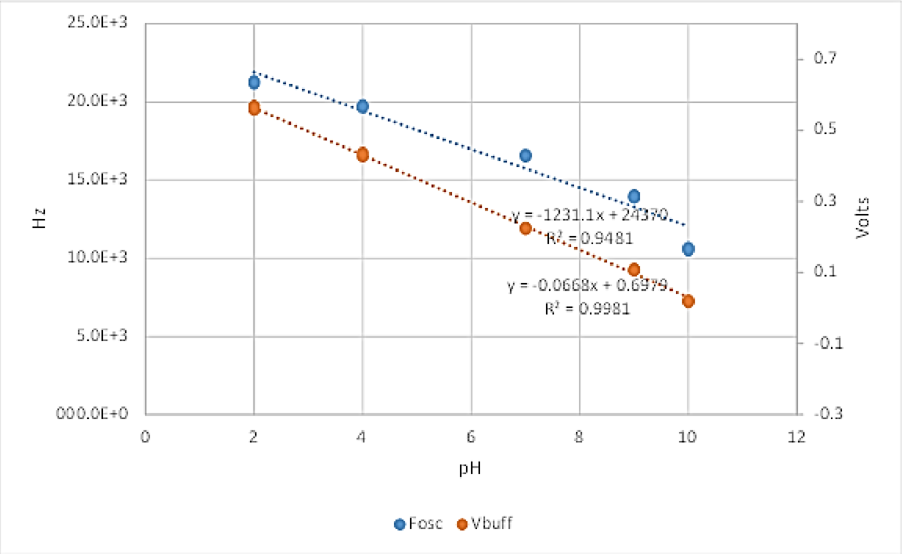

Figure 69- Buffered relaxation oscillator results of 5pt pH buffer test with IrOx electrode vs a commercial AgCl RE. Fosc = frequency of oscillation resulting from relaxation oscillator, Vbuff = probe voltage being transmitted into the buffer, as measured by the NI DAQ mentioned in previous chapters.

Another VCO-style design was attempted based on a buffered relaxation oscillator. The base design, as taken from [1], is shown in Figure 68(a). Given the op-amps available at the time, a pull-up was required at the output of the oscillation stage to initiate oscillation.

This circuit showed promise, as shown in Figure 69. Unfortunately, the oscillation frequency featured a nonlinearity that the probe voltage did not. It was unclear what caused this nonlinearity, as the circuit was being provided with a highly stable power supply from a benchtop unit and the oscillation waveform itself appeared to be well formed (i.e. did not have significant ringing, overshoot, or other artifacts).

In an effort to make use of the circuit anyways, it was rebuilt on a prototyping board to interact with a 1 MHz Tx board; in its second iteration, it was supplied by power across the inductive link and the output frequency was lowered to attempt to improve automatic oscilloscope frequency identification. Results from that test, transmitted back across to the Tx side, are shown in Figure 70. As will be noted, the signal was nonlinear beginning directly at the buffer output.

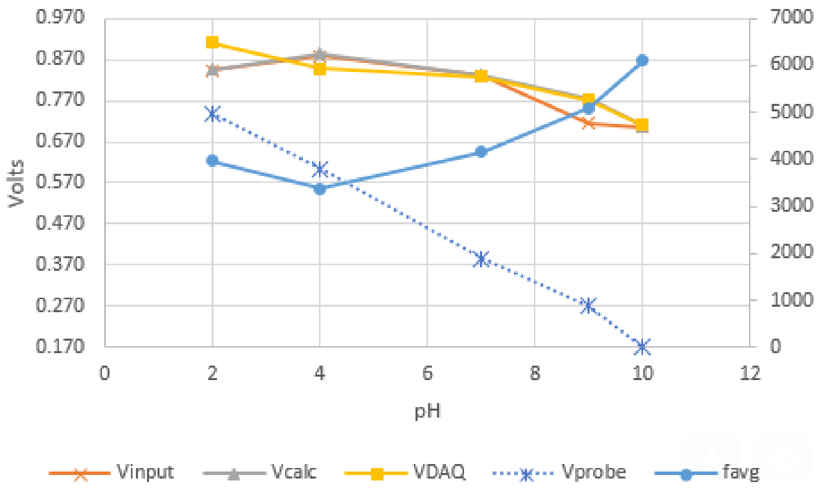

Figure 70- Buffered relaxation oscillator v2 results, received back at the Tx side. Vinput = probe voltage as measured by DMM, prior to VCO. VDAQ = same voltage, as measured by NI DAQ; simply used as a reference. favg = frequency resulting from the VCO, given those input voltages. Vcalc = probe voltage as calculated from output frequency. Vprobe = the same 1 mm^2 IrOx probe voltage, vs a commercial Ag/AgCl RE, as measured afterward by the standard testing buffer circuit.

Not only this, but the frequency output was nearly parabolic in nature. It is likely that there was a misconfiguration somewhere, given previous successes with this design, but they were not determined in this case. The only bright spot here was that the pH probes were truly buffered; negligible current flowed and no sensor damage was observed.

In an attempt to simplify the circuit and stabilize the probe buffer, a decision was made to rebuild the circuit using discrete IC's. The modulation section of this new version is shown in Figure 71. The IC labeled as "LT" is Analog Devices' LTC6990 VCO; this device accepts a range of input voltages at the "SET" pin to oscillate at a variety of frequencies at the "OUT" pin, the ratio between the two being adjusted by resistor pairs at the "DIV" (or Divider) pin and "SET" pin. This oscillatory output is then used to drive a MOSFET attached to the wireless sinusoid, varying the amplitude of the transceived sinusoid at a calibrated frequency.

This circuit provided the first successful results for this scheme; these results can be seen in Figure 72.

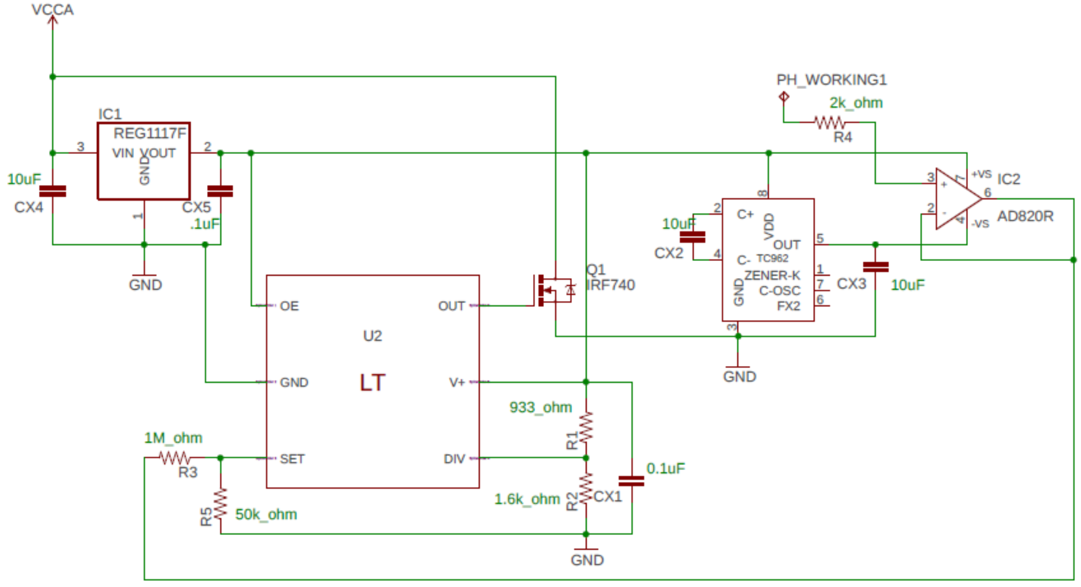

Figure 71- FM circuit, modulation portion only, built around the use of the Analog Devices LTC6990 VCO (labeled as "LT" above). Schematic courtesy Miguel Huerta.

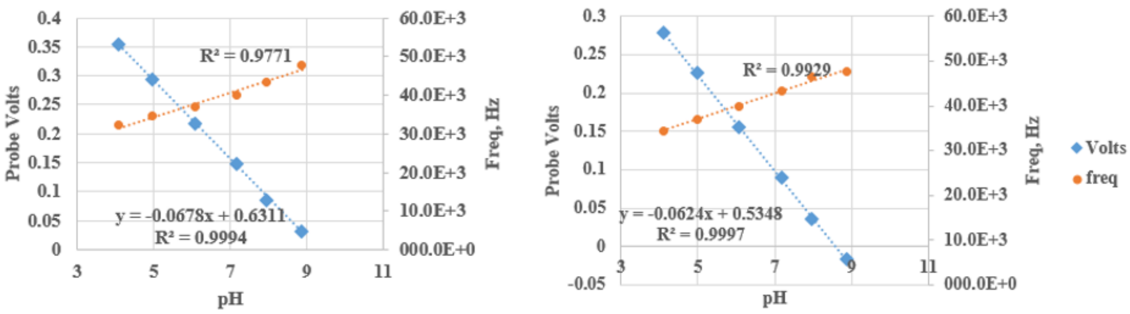

Figure 72- Example of two different probe calibrations as performed over an FM-style wireless link. Shown also are least squares linear regressions for both probe voltage and circuit output frequency, as well as the sensitivity curves for the voltages recorded and the regression statistic for all fits. Volts were measured by DMM during each bath test.

4.2.3 Bluetooth Scheme

For ease of use, and to fully demonstrate a proof-of-concept, a commercial Bluetooth-Low-Energy (BLE) board was used as an input stage and wireless link. The nRF51 development board (Nordic Semiconductor, Trondheim, Norway) was chosen mostly due to its popularity and support.

To make use of this board, MCU code (for timing and interrupts based on a single ADC input) and an Android application were written by another researcher. For testing purposes, the

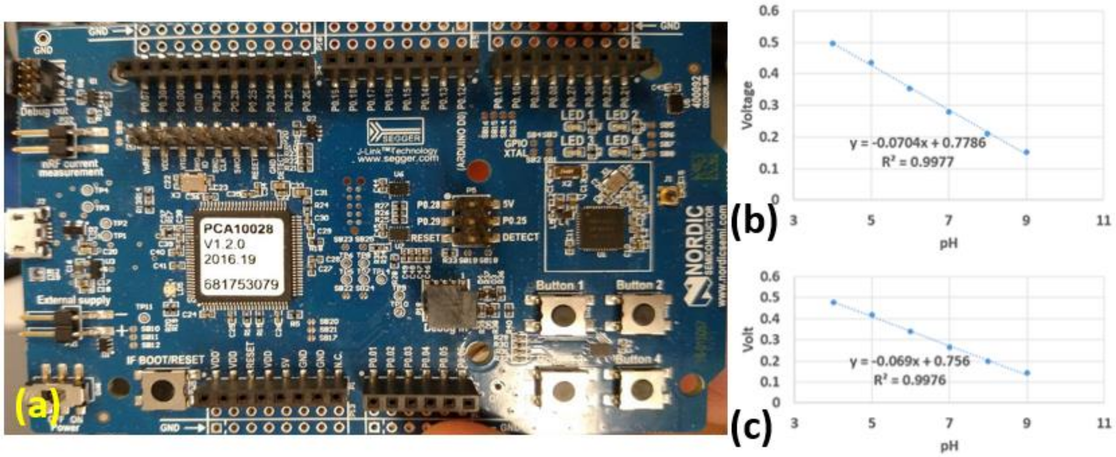

Figure 73- BLE board and performance. (a) image of Nordic nRF51 board. (b) IrOx probe as measured by traditional wired system. (c) the same IrOx probe, measured immediately afterward, via 2.4GHz BLE link to Android smartphone application.

Nordic board was supplied with wired 5V power via USB; its 5V output was then used to power the buffer/amplifier as shown in the testing section of the probe characterization chapter, whose analog output was then fed back to the ADC input on the BLE board. This was done to prove that, given a power supply, this and similar systems could be entirely self-contained.

The development board and transmission results are shown in Figure 73. Linearity and sensitivity saw almost no change, the delta most likely being up to measurement error. Interestingly, the regression’s intercept value changed; this may or may not have been due to wireless transmission, as wear on the probes could reduce thickness and IrOx film capacitance, which could in turn lower the intercept. If this method is used in the future, this effect will be of interest.

5. Future Work

5.1 Wireless Patch Design

As the original intention of this thesis was to have a fully functioning wireless device adhered to a flexible substrate, completing this will be the first task taken up after completion of this thesis. Although the Bluetooth scheme as shown previously was simple to implement for demonstration purposes, attachment of an IC to a flexible substrate is quite difficult to accomplish in practice; instead, the design will strive to operate with a minimum of passive or discrete components. In this way, the required footprint of each component and the circuit as a whole can be reduced, thus reducing the likelihood of local mechanical peeling of the adhesive under bending stress. An example of a PCB layout for the FM scheme is shown in Figure 75.

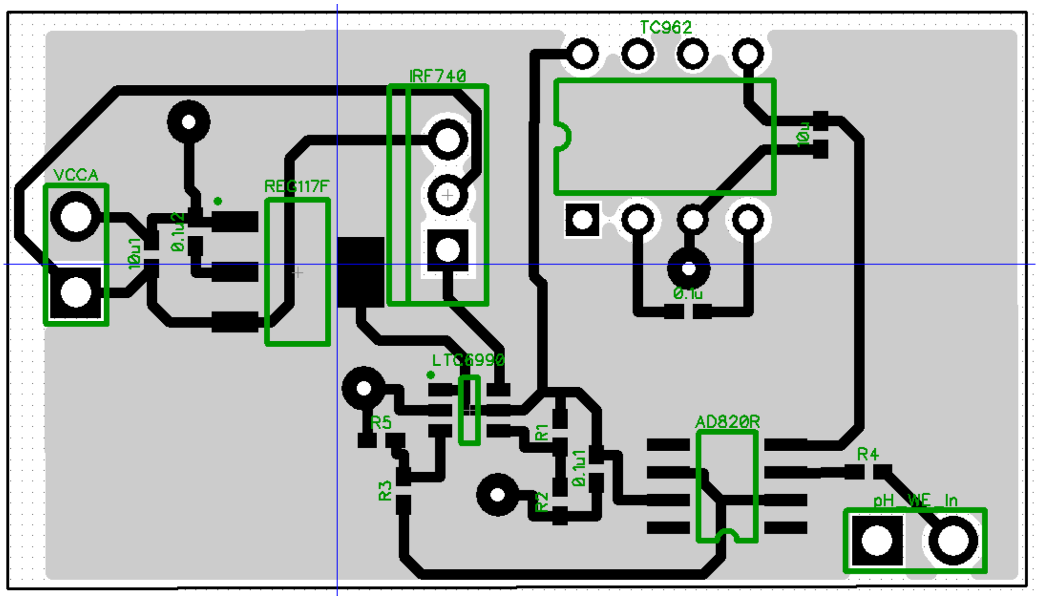

Figure 75- First iteration of potential PCB layout for FM wireless circuit. Will need ground plane adaptation to apply to flexible substrate.

Some adhesive failure testing (such as a standard single lap joint adhesive peel test) and calculation/simulation may be required, and CTE taken into account. Outside of the polyimide already in use, attempts will also be made to use other flexible substrates which can be produced within existing labs and to thinner specifications, such as poly-p-xylylene. An added benefit of such a polymer is that, while requiring energy to produce, does not actually require solvent or

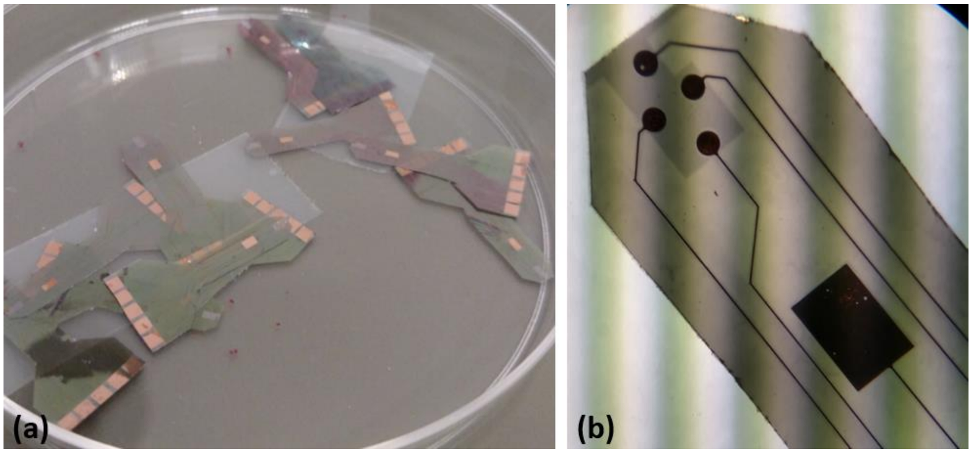

Figure 74- Examples of electrocardiography electrodes produced on poly-p-xylylene. (a) a batch of trimmed probes. (b) single probe when viewed under a microscope.

catalysts to initiate polymerization. An example of probes for electrocardiography (ECG) produced, by chemical vapor deposition (CVD), from poly-p-xylylene is shown in Figure 74.

Ideally, the patch would contain its own flexible antenna so that the entire device could be conformed to the interior wall of, for example, a municipal water pipe to monitor water quality or the inside of a milk jug to monitor food freshness. To promote extreme levels of conformability, investigation has already begun on fabrication of fluidic antennas encased in polymer. Specifically, the first iteration is expected to be a Gallium-Indium-Tin alloy in liquid phase, known for its low viscosity and nontoxic nature, encased in a polydimethylsiloxane (PDMS) housing, known for its toughness and high elasticity (and is also nontoxic). This antenna, combined with a flexible sensor package, could then be adhered to surfaces which themselves flex regularly. Demonstrations of manufacturing principles have already begun with SU-8 negative photoresist (Microchem, Westborough, MA) templates, produced by lithography upon Si wafer substrates, used for PDMS forming. These are shown in Figure 76.

5.2 Surface Modifications

Several surface modifications are of interest. Given the size-based sensitivity

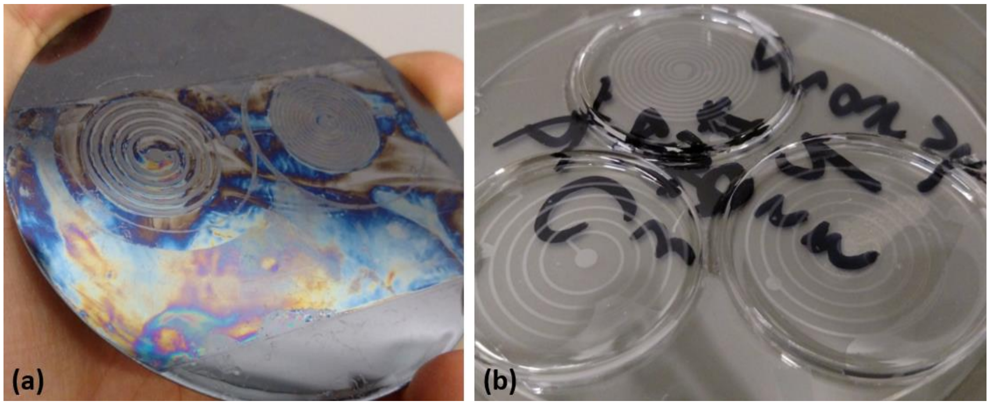

Figure 76- Beginnings of flexible antenna fabrication process. (a) SU-8 mold atop Si wafer after lithography process. (b) A few samples of the PDMS antenna halves produced atop the SU-8 molds.

improvements demonstrated in the probe characterization chapter but keeping in mind the roughness limits imposed by Elsen *et al.* [12], nanocolloids attached to the IrOx plating surface are being investigated.

Also, given the extended service times that are hoped for in the final product, surface modifications which extend the lifetime of the thin film are of interest. One such coating which would allow ion movement but provide a physical barrier between IrOx and solution is Nafion (*DuPont, Omaha, NE*), a sulfonated tetrafluoroethylene (TFE), which will be discussed below.

5.2.1 Au Nanocolloid Particles

As it is not yet known which, if any, size of Au Nanocolloid would improve probe sensitivity, multiple spherical sizes were chosen; specifically, 5, 20, and 40 nm diameter spheres (#741965, #741981, #741949, Sigma Aldrich, St. Louis, MO).

These particles were concentrated, applied, and dried per procedures available in literature [51] but significant testing has yet to take place.

5.2.2 Nafion Coating

The main purpose of Nafion, as mentioned above, is to allow only some ions to pass to the electrode surface without letting larger, possibly damaging molecules, to reach it. It’s termed a “permselective membrane separator,” and was initially used to allow, for example, Na+ ions to pass while disallowing OH- ions [52].

Following an earlier cure profile, the Nafion was distributed upon Au and cured at 170°C for 5 minutes. Unfortunately, this produced the burned polymer as shown in Figure 77. When tested, the output was found to be floating, indicating that the Nafion had become impermeable.

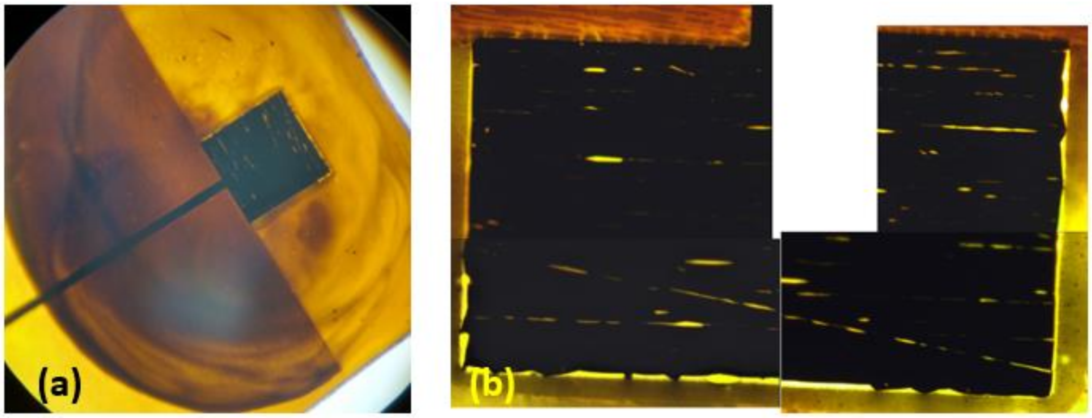

Figure 77- Nafion applied by hand and cured to 170°C for 5 minutes. (a) the Nafion drop as seen through a microscope. (b) a composite image of four digital microscope views showing the Nafion surface directly over the sensing pad.

Based on manufacturer suggestions as listed in [53], the cure temp was lowered to 95°C and cure time extended to 10 minutes. Unfortunately, visual and test results were the same. The damage to the Nafion appeared to be even worse this time, resulting in bubbling and cracking. It is thought that, in the future, deposits of controlled thickness may aid this process and allow other results to be reproduced.

5.3 Package Improvements

Anticipatory steps have begun to improve the size and attachment methods for the final design. On the attachment side, connectors for flexible electronics are being investigated. In terms of sizing, reproduction of microelectrode arrays is planned for the future.

5.3.1 ZIF FPC Connectors

A popular method of connecting modern flexible circuits is through what are known as zero insertion force (ZIF) flexible printed circuit (FPC) connectors. The idea behind these is that the contact pad is lowered into position (thus zero insertion force) and the contact thickness window is sufficiently narrow to allow for common cable thicknesses in flexible printed circuit

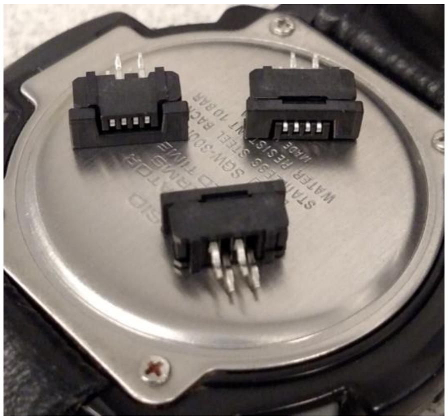

Figure 78- ZIF FPC connectors as made by Amphenol ICC (Wallingford, CT). Shown are the SLW4S-1C7LF, which can accept 300 µm thick cables. The 127 µm thick polyimide used will need a backing layer attached to it.

boards. Examples of commercial ZIF FPC connectors currently being experimented with are shown in Figure 78.

With the probe attached, about 5Ω of resistance is added to prior probe measurements. In theory, this small series resistance should not affect the coating process. As of now, some probes coated with these devices have turned out well, so perhaps some mask redesign to make use of the SLW4S is in order. The use of these is shown in Figure 79.

5.3.2 Electrode Arrays

To potentially allow for various noise reduction, signal averaging, probe redundancy, and

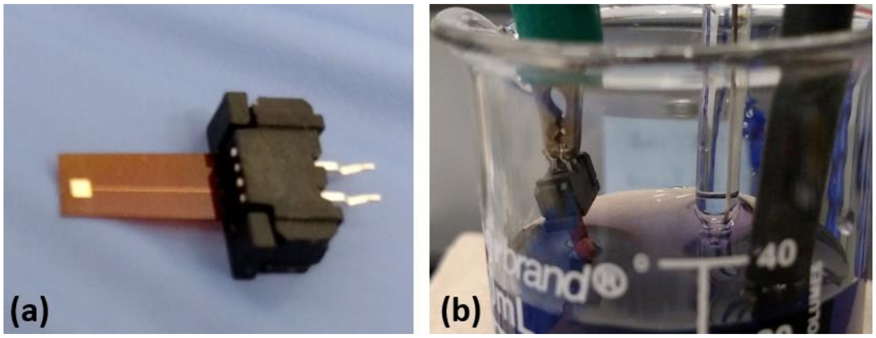

Figure 79- Use of FPC connectors. (a) attachment to 1 mm^2 Au probe. (b) coating process with same probe.

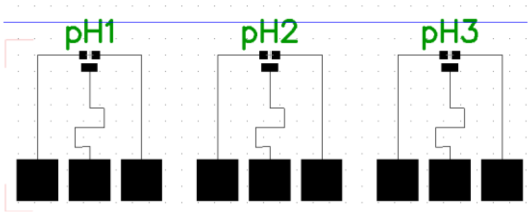

Figure 80- Simple 3-point microelectrode array; sensing pad sizes are 200 µm, reference pad is 200 × 400 µm^2. Note nonlinear path for reference electrode to equalize trace length.

signal mapping strategies, upcoming electrode packages are intended to be arrays, rather than individual probes. A preliminary design concept is shown in Figure 80. In this scheme these 3-point arrays feature 200 µm^2 sensing pads and one 200 × 400 µm reference pad; these would be matched end to end with another probe set, providing four sensing pads and two references in a small area. This could be scaled up to any number of electrodes in any geometric configuration, assuming trace lengths and matched surface areas are taken into account.

5.4 Autonomous Surface Vehicles

One possible application of these sensors is being applied to a spool system or the outer hull of some kind of autonomous surface vehicle (ASV). The following information, excerpted from an Amazon Catalyst competition submission written by this author and Dr. Hung Cao, is written below. In this section, the potential recipients were expected to produce a hypothetical press release detailing their product launch:

‘*Their solution is comprised of a fully-integrated drone ship which can sense pH and various heavy metals, in nominated depths and locations, with real-time communication with a smart device. Moreover, it can be programmed to follow designated GPS paths and carry out analyses at each point automatically, then continuously upload data to the cloud…Our system is capable of providing a data map of water quality for everyone from doctors in the Niger delta to EPA personnel in UW’s hometown of Seattle…*’

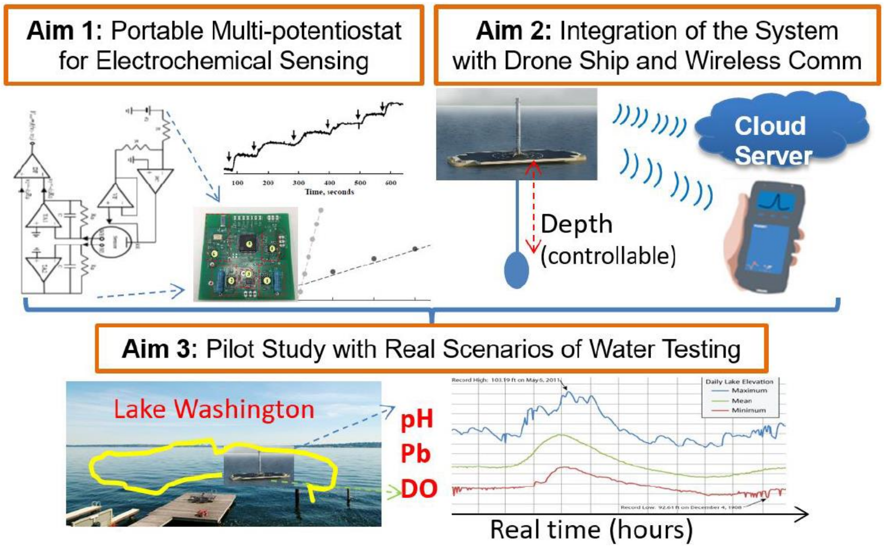

Figure 81- Idealized ASV operation, as originally proposed for Amazon Catalyst competition in October of 2016. Image courtesy Dr. Hung Cao.

A visual layout of the described system is shown in Figure 81.

6. Conclusion

In the thesis presented prior, a complete system for the measurement of pH was proposed for both varying biological applications and in water quality detection; its development, manufacturing, and usability in limited real world circumstances was demonstrated. The novelty of the device lies in its combination of electrodeposited iridium oxide (IrOx) films, flexible and biocompatible substrates, and wireless connectivity. The device shown combines the stability and performance of those films with the applicability of polyimide and the real time communication provided by both Bluetooth-low-energy (BLE) and frequency-based load modulation (FM) circuits. The FM scheme featured the added benefit of being powered over inductive link.

On the manufacturing side, it was determined that large sensing surface areas (1 mm2) and long deposition times (~50 minutes) achieved the highest performing and most stable probes, but usable devices could be produced from 200 µm2 of exposed area or 1 mm2 probes that were coated for just over 6 minutes. It became clear that other CV and lithography factors affected morphology but their performance-related effects were not determined. Reference electrodes (RE’s) were shown to be easily fabricated by hand. All materials tended to degrade in strong acids, through IrOx failed mainly by grain shrinkage and a possibly strain-induced peeling mechanism, whereas both phase separated solids in AgCl tended to lose their bond with the conductive layer. It was also determined that copper is a currently unusable conductive layer due to surface oxidation, most likely occurring during both cyclic voltammetry (CV) and testing.

Characterized probes tended to perform well above Nernstian sensitivity and feature stable and fast response, even in the presence of mechanical bending, but did see offsets when tested in cationic solutions of various kinds. Using a simple buffer with gain and a virtual ground, it was determined that IrOx working electrodes (WE’s) versus commercial RE’s tended to be near 70 mV/pH and have a limit of detection (LOD) of 0.04 pH, with linearity of R2 = 0.996 or better; custom RE’s tended to lower the sensitivity and linearity slightly and these AgCl RE’s show ~30-40 mV of drift over several days of submersion but the devices still feature super-Nernstian sensitivity and linearity above R2 = 0.96. Response time was typically less than 2 seconds.

Final performance parameters differed in their causal relationships with CV parameters. Confirming other literature, sensitivity depended only upon a minimum number of sweeps at an indeterminate sweep rate but the best compromise in LOD and hysteresis was found with the original deposition recipe. Interestingly, surface area increases had a proportional effect on increases in sensitivity and decreases in LOD, possibly up to differences in proton diffusion area and IrOx layer capacitance. Heavily cationic baths tended to boost sensitivity by several mV/pH but lower linearity, and readings of bio-equivalent sweat solution were high by ~0.4-0.8 pH when compared to a commercial probe. Mechanical bending had negligible effects on performance.

Attempts were made to and code is included for the automatic removal of noise in results and characterization of those results. Automatic characterization requires multiple manual inputs and noise removal performance is poor, so both are considered to be ongoing projects. At this time, only lowpass filtering is performed for automatic characterization; if manual characterization is done, no filtering is applied.

Multiple integrated pH sensing devices were demonstrated, ranging from layered low temperature co-fired ceramic circuits (LTCC) to commercial BLE and discrete AM and FM schemes. Both BLE and FM schemes produced nearly identical results to wired calibrations, in terms of sensitivity and linearity; FM schemes did not require battery or external power. All are candidates for future miniaturization and simplification.

To convert this to commercial style packages, multiple future works are in progress. These range from surface and substrate material experimentation to conformable antennas to scalable integration into fully autonomous sensing vehicles. It is hoped that the end product will be a modular package, inexpensively produced, able to sense a multitude of solution chemical factors.

7. References

[1] W.-D. Huang, *A ph sensor based on a flexible substrate*: The University of Texas at Arlington, 2010.

[2] D. A. Brownson and C. E. Banks, *The handbook of graphene electrochemistry*: Springer, 2014.

[3] H. Jones, N. El Zarif, A. Brockett, K. Martin, W. Kimura, and H. Cao, "Passive Wireless pH Sensing System," University of Washington Bothell Electrical Engineering, Capstone Project Report2016.

[4] D. C. Bellinger, "Lead contamination in Flint—an abject failure to protect public health," *New England Journal of Medicine*, vol. 374, pp. 1101-1103, 2016.

[5] H. E. Amor, A. B. Kouki, P. Marsh, K. T. Kim, and H. Cao, "Development of a novel miniaturized LTCC-based wireless pH sensing system," in *SENSORS, 2016 IEEE*, 2016, pp. 1-3.

[6] W.-D. Huang, H. Cao, S. Deb, M. Chiao, and J.-C. Chiao, "A flexible pH sensor based on the iridium oxide sensing film," *Sensors and Actuators A: Physical,* vol. 169, pp. 1-11, 2011.

[7] G. Hammer, "XPS Analysis of Iridium Oxide Films," P. Marsh, Ed., Personal communication; reporting of analysis results of four samples: Cu/Cr/Kapton before and after pH buffers and Au/Cr/Kapton before and after pH buffers. ed: Molecular Analysis Facilty, University of Washington, 2017.

[8] P. Marsh, W. Moore, M. Clucas, L. Huynh, K.-T. Kim, S. Yi, *et al.*, "Characterization of Flexible pH micro-Sensors Based on Electrodeposited IrOx Thin Film," in *IEEE Sensors*, Glasgow, Scotland, 2017.

[9] P. Ritchie, M. Huerta, T. L. Lau, J. Agee, and H. Cao, "Passive Continuous Electrocardiogram Monitoring of Firemen Using Non-Contact Electrodes," presented at the IEEE SENSORS 2017, Glasgow, Scotland, 2017.

[10] C. Callewaert, B. Buysschaert, E. Vossen, V. Fievez, T. Van de Wiele, and N. Boon, "Artificial sweat composition to grow and sustain a mixed human axillary microbiome," *Journal of microbiological methods,* vol. 103, pp. 6-8, 2014.

[11] L.-C. Hsu, "Physiological Telemetric Sensing Systems For Medical Applications," University at Texas Arlington Libraries, online2012-04-11 2012.

[12] H. A. Elsen, C. F. Monson, and M. Majda, "Effects of electrodeposition conditions and protocol on the properties of iridium oxide pH sensor electrodes," *Journal of The Electrochemical Society,* vol. 156, pp. F1-F6, 2009.

[13] S. Chotpantarat, S. K. Ong, C. Sutthirat, and K. Osathaphan, "Effect of pH on transport of Pb2+, Mn2+, Zn2+ and Ni2+ through lateritic soil: column experiments and transport modeling," *Journal of Environmental Sciences,* vol. 23, pp. 640-648, 2011.

[14] R. Smallteacher, "Formosa plastics admits Vietnam steel plant caused massive fish kill, 4 July 2016, CorpWatch," ed, 2016.

[15] A. van Ooyen, V. Zagolla, C. Ulrich, and U. Schnakenberg, "SIROF stimulation electrode evaluation using the pulse–clamp method," *Procedia Chemistry,* vol. 1, pp. 269-272, 2009.

[16] M. Harada, "Minamata disease: methylmercury poisoning in Japan caused by environmental pollution," *Critical reviews in toxicology,* vol. 25, pp. 1-24, 1995.

[17] R. Smith, R. Knight, J. Chen, J. Reeves, H. Zebker, T. Farr, *et al.*, "Estimating the permanent loss of groundwater storage in the southern San Joaquin Valley, California," *Water Resources Research,* vol. 53, pp. 2133-2148, 2017.

[18] C. Welch. (2018, 28-Mar-2018). Why Cape Town Is Running Out of Water, and Who’s Next. *National Geographic*. Available: https://news.nationalgeographic.com/2018/02/cape-town-running-out-of-water-drought-taps-shutoff-other-cities/

[19] T. Veldkamp, Y. Wada, J. Aerts, P. Döll, S. Gosling, J. Liu, *et al.*, "Water scarcity hotspots travel downstream due to human interventions in the 20th and 21st century," *Nature communications,* vol. 8, p. 15697, 2017.

[20] Staff, "Water - Overview," World Bank, Online, Report20-Sep-2017 2016.

[21] Staff. (2015, 28-Mar). *Water Instrumentation Market to Reach $3.6 Billion by 2020*. Available: https://www.wwdmag.com/trends-forecasts/water-instrumentation-market-reach-36-billion-2020

[22] EPA. (2016, 1-March). *Fiscal Year 2016 - EPA* [Budget Report]. Available: https://www.epa.gov/sites/production/.../epa_fy_2016_congressional_justification.pdf

[23] NWQMC. (2014, 1-March). *Volunteer Monitoring*. Available: https://acwi.gov/monitoring/vm/

[24] United States Geographic Survey, "USGS Water-Quality Data for the Nation," United States Geographic Survey, Ed., ed. Online, 2018.

[25] L. A. Winslow, J. S. Read, P. C. Hanson, and E. H. Stanley, "Lake shoreline in the contiguous United States: quantity, distribution and sensitivity to observation resolution," *Freshwater Biology*, vol. 59, pp. 213-223, 2014.

[26] Staff. Lake Washington Monitoring Overview [Online]. Available: http://green2.kingcounty.gov/lakes/LakeWashington.aspx

[27] Staff. Cottage Lake Monitoring Overview [Online]. Available: http://green2.kingcounty.gov/SmallLakes/LakePage.aspx?SiteID=9

[28] EPA. (2017, 29-Mar). *Drinking Water Regulations and Contaminants*. Available: https://www.epa.gov/dwregdev/drinking-water-regulations-and-contaminants

[29] P. O. Fromm, "A review of some physiological and toxicological responses of freshwater fish to acid stress," *Environmental Biology of Fishes,* vol. 5, pp. 79-93, 1980.

[30] O. L. c. Gamborg, R. A. Miller, and K. Ojima, "Nutrient requirements of suspension cultures of soybean root cells," *Experimental cell research,* vol. 50, pp. 151-158, 1968.

[31] K. Sandvig and S. Olsnes, "Entry of the toxic proteins abrin, modeccin, ricin, and diphtheria toxin into cells. II. Effect of pH, metabolic inhibitors, and ionophores and evidence for toxin penetration from endocytotic vesicles," *Journal of Biological Chemistry,* vol. 257, pp. 7504-7513, 1982.

[32] J. B. Russell and D. Dombrowski, "Effect of pH on the efficiency of growth by pure cultures of rumen bacteria in continuous culture," *Applied and Environmental Microbiology,* vol. 39, pp. 604-610, 1980.

[33] A. S. Travis, H. G. Schröter, E. Homburg, and P. J. Morris, *Determinants in the Evolution of the European Chemical Industry, 1900–1939: New Technologies, Political Frameworks, Markets and Companies* vol. 16: Springer Science & Business Media, 1998.

[34] A. Fog and R. P. Buck, "Electronic semiconducting oxides as pH sensors," *Sensors and Actuators,* vol. 5, pp. 137-146, 1984.

[35] L. D. Burke and D. Whelan, "A voltammetric investigation of the charge storage reactions of hydrous iridium oxide layers," *Journal of electroanalytical chemistry and interfacial electrochemistry,* vol. 162, pp. 121-141, 1984.

[36] J. C. Hidalgo-Acosta, M. D. Scanlon, M. A. Méndez, V. Amstutz, H. Vrubel, M. Opallo, *et al.*, "Boosting water oxidation layer-by-layer," *Physical Chemistry Chemical Physics,* vol. 18, pp. 9295-9304, 2016.

[37] S. Yao, M. Wang, and M. Madou, "A pH electrode based on melt-oxidized iridium oxide," *Journal of the electrochemical society,* vol. 148, pp. H29-H36, 2001.

[38] T. Katsube, I. Lauks, and J. Zemel, "pH-sensitive sputtered iridium oxide films," *Sensors and Actuators,* vol. 2, pp. 399-410, 1981.

[39] K. Yamanaka, "Anodically electrodeposited iridium oxide films (AEIROF) from alkaline solutions for electrochromic display devices," *Japanese journal of applied physics,* vol. 28, p. 632, 1989.

[40] K. G. Kreider, M. J. Tarlov, and J. P. Cline, "Sputtered thin-film pH electrodes of platinum, palladium, ruthenium, and iridium oxides," *Sensors and Actuators B: Chemical,* vol. 28, pp. 167-172, 1995.

[41] K. Nishio and T. Tsuchiya, "Electrochromic thin films prepared by sol–gel process," *Solar energy materials and solar cells*, vol. 68, pp. 279-293, 2001.

[42] W.-D. Huang, S. Deb, Y.-S. Seo, S. Rao, M. Chiao, and J. Chiao, "A passive radio-frequency pH-sensing tag for wireless food-quality monitoring," *IEEE Sensors Journal*, vol. 12, pp. 487-495, 2012.

[43] I. A. Ges, B. L. Ivanov, D. K. Schaffer, E. A. Lima, A. A. Werdich, and F. J. Baudenbacher, "Thin-film IrO x pH microelectrode for microfluidic-based microsystems," *Biosensors and Bioelectronics*, vol. 21, pp. 248-256, 2005.

[44] J. Hu, M. Abdelsalam, P. Bartlett, R. Cole, Y. Sugawara, J. Baumberg, *et al.*, "Electrodeposition of highly ordered macroporous iridium oxide through self-assembled colloidal templates," *Journal of Materials Chemistry*, vol. 19, pp. 3855-3858, 2009.

[45] C. Iliescu, B. Chen, and J. Miao, "Deep wet etching-through 1mm pyrex glass wafer for microfluidic applications," in *Micro Electro Mechanical Systems, 2007. MEMS. IEEE 20th International Conference on*, 2007, pp. 393-396.

[46] N. Chatterjee, "Electron Microprobe Analysis Lecture Notes," in *Course 12.141 Notes*, ed. MIT Opencourseware Website: MIT Opencourseware, 2012.

[47] P. Kurzweil, "Metal oxides and ion-exchanging surfaces as pH sensors in liquids: State-of-the-art and outlook," *Sensors*, vol. 9, pp. 4955-4985, 2009.

[48] K. Cheng and D.-M. Zhu, "On calibration of pH meters," *Sensors*, vol. 5, pp. 209-219, 2005.

[49] J. Shlens, "A tutorial on independent component analysis," *arXiv preprint arXiv:1404.2986*, 2014.

[50] H. Cao, V. Landge, U. Tata, Y.-S. Seo, S. Rao, S.-J. Tang, *et al.*, "An implantable, batteryless, and wireless capsule with integrated impedance and pH sensors for gastroesophageal reflux monitoring," *IEEE Transactions on Biomedical Engineering*, vol. 59, pp. 3131-3139, 2012.

[51] H. Cao, C. Nguyen, and J. Chiao, "Fabrication and surface-modification of implantable microprobes for neuroscience studies," *Advances in Natural Sciences: Nanoscience and Nanotechnology*, vol. 3, p. 025003, 2012.

[52] K. A. Mauritz and R. B. Moore, "State of understanding of Nafion," *Chemical reviews*, vol. 104, pp. 4535-4586, 2004.

[53] M. Kim, M. Jia, and T. Kim, "Ion concentration polarization in a single and open microchannel induced by a surface-patterned perm-selective film," *Analyst*, vol. 138, pp. 1370-1378, 2013.

8. Appendix A – Code

Independent Component Analysis Code

```
%% Startup
clear
close all

%% Load Data
load('Noise-Signal2.mat');
```

```
%Clean NaN's since they break filters
Noise(isnan(Noise)) = [];
Signal(isnan(Signal)) = [];

%% Run ICA from FastICA project
data = [Noise';Signal']; %create inputs; one row per channel

pause(2); %without this, ICA calc does not converge sometimes

[icasig] = fastica(data); %their algorithm whitens and transforms
%approaches give no output difference, just change computation time
%default numOfIC is fine
%nonlinearities - couldn't see a difference with any
%step size- >1 causes stroke, 0.1<mu<1 shows no change, <0.1 takes forever
%to converge
%maybe could manipulate whitening?

%this ICA algorithm also seems to invert the signals sometimes
if mean(icasig(1,:)) < 0
    icasig(1,:) = -1 .* icasig(1,:);
end
if mean(icasig(2,:)) < 0
    icasig(2,:) = -1 .* icasig(2,:);
end

%plot vs original
figure('units','normalized','outerposition',[0 0 1 1])
subplot(221),plot(icasig(1,:))
xlabel('sample'),ylabel('volts'),title('Independent "Noise" Component')
subplot(222),plot(Noise)
xlabel('sample'),ylabel('volts'),title('Original "Noise" channel')
subplot(223),plot(icasig(2,:))
xlabel('sample'),ylabel('volts'),title('Independent "Signal" Component')
subplot(224),plot(Signal)
xlabel('sample'),ylabel('volts'),title('Original "Signal" channel')
```

Automatic Characterization Code

```
%% Basics
clear
close all

load('50sweep.mat');
%load('200umTest.mat');
```

```
%% Define input vector
pH = [2.2 4.37 5.4 6.9 8.8 9.87];
pH = [pH pH pH];
%pH = [2 4 7 9 10 9 7 4 2];

%% Function inputs
fs = 10; %Hz
gain = 2.65; %output side circuit gain
output = 1; %see graphs?
timeThresh = 7; %seconds for proper reading
SDthresh = 0.015; %Volts of std dev; write fitness function to find this for me!

%% Retrieve parameters
[ sens, LOD, repeat ] = pHparams(pH,Voltage,fs,gain,output,timeThresh,SDthresh);

%This whole thing is still unable to reliably match hand-calculated values. May need to include LPF to thresholded data before processing even begins
```

pHparams.m:

```
function [ sens, LOD, repeat ] = pHparams( pH, volts, fs, gain, output, timeThresh, SDthresh )
%[ sens, LOD, repeat ] = pHparams( pH, volts, fs, gain, output, timeThresh, SDthresh )
%
%    A not particularly clever script for calculating sensitivity, limit of
%    detection, and repeatability for a given pH bath test.
%    **NOTE** Some manual internal tuning may be required as more data is
%    run through this function
%
%    sens = sensitivity, in mV/pH
%    LOD = average limit of detection, in pH
%    repeat = average repeatability, in pH
%    pH = vector of pH baths run through
%    volts = vector containing circuit voltage output during testing
%    fs = DAQ sampling frequency, in Hz
%    gain = circuit gain; typically 2 to 2.65
%    output = flag determining whether or not graphs will be shown during
%        execution (1 == on, 0 == off)
%    timeThresh = minimum time, in seconds, to be considered a proper
%        reading
%    SDthresh = std dev of voltage used to gate data (account for ADC)

%% Set basic vars
winSize = round(fs/10);
if winSize < 3
    winSize = 3; %want to avg and such by at least 3 samples
end
SMSD = zeros((length(volts)),1); %moving standard deviation
startVec = zeros((length(pH)),1); %beginning of pH bath
endVec = zeros((length(pH)),1); %end of pH bath
outputV = zeros((length(pH)),1); %actual voltage in each range
outputSD = zeros((length(pH)),1); %voltage std dev in each range
startInd = 1; endInd = 1; nextpH = 0; %looping indices
uniquePh = unique(pH); %get unique pH levels
LOD = zeros((length(uniquePh)),1); %get LODs for all pH levels
```

```
repeat = zeros((length(uniquePh)),1); %get repeatabilities for all pH levels
dT = 1/fs; %time delta
COf = 1.5; %cutoff freq, in Hz
order = 50; %order of LPF

%% Filter Definition
filt = fir1(order,(2*COf)/fs,'low'); %center term is to convert COf from Hz to pi(rad/samp)
if output == 1
    figure;
    freqz(filt); %check filter
    title('Filter Output');
end

%% Prepare usable test vector
SMSD = movstd(volts,winSize); %calculate standard deviations
volts(SMSD > SDthresh) = 0; %remove noisy data

if output == 1
    figure
    plot(SMSD)
    title('Standard Deviations')
    figure
    plot(volts)
    title('Thresholded Data')
end

%% Break up data by pH list
trueData = 1 .* (volts > 0); %vector for when data hasn't been removed
j = 1;
for i = 2:(length(trueData)-1)
    if trueData(i) == 1
        if(nextpH == 1)
            startInd = i;
        end
        trueData(i) = (trueData(i-1) + trueData(i)); %increment for continued stints of data capture
        endInd = i;
        nextpH = 0;
    else
        nextpH = 1;
    end
    %make array of start and end times for pH data sections
    if (((endInd - startInd)/fs) > timeThresh) && (nextpH == 1)
        startVec(j) = startInd;
        endVec(j) = endInd;
        if (endInd - startInd) > 1
            startInd = endInd - 1;
        end
        j = j+1;
    end
end

trueData = trueData / fs; %convert to time vector

if output == 1
    figure
```

```
    plot(trueData)
    title('Stretches of Data')
    ylabel('seconds')
    figure
    plot(startVec)
    hold on
    plot(endVec,':m')
    title('Indexes for data sections')
end

%confirm pH sections
pHsec = zeros(length(volts),1);
for i = 1:length(pH)
    pHsec(startVec(i):endVec(i)) = pH(i);
end

if output == 1
    figure
    tempTime = (((1:length(pHsec))/fs))';
    plot(tempTime,pHsec)
    title('pH Level')
    xlabel('seconds')
end

%% Retrieve output values in each pH bath
for j = 1:length(pH)
    data = volts(startVec(j):endVec(j)); %get data
    deriv = diff(movmean(data,round(winSize*(length(data)/10))))/(dT); %find data's derivative
    smoothDeriv = abs(filter(filt,1,deriv)); %1 is denominator; remove any spikes with LPF
    [minD, index] = min(smoothDeriv((5*fs):length(smoothDeriv))); %determine minimum from 5 sec on, to avoid data intialization
    index = index + (5*fs); %adjust index to match data, not snippet

    %make window
    s = index-fs;
    if (index-fs) < 0
        s = 1;
    end
    e = index+fs;
    if (index+fs) > length(data)
        e = length(data);
    end

    tempData = data(s:e)./gain; %gather +/-1sec of data, or as much as possible, and get into probe voltage
    if output == 1
        figure; subplot(411),plot(data)
        title('raw data')
        subplot(412),plot(deriv)
        title('derivative')
        subplot(413),plot(smoothDeriv)
        title('LPFd derivative')
        subplot(414),plot(tempData)
        title('data taken for calcs')
    end
    tempData = tempData * 1000; %put in mV
```

```
    %catalogue outputs
    outputV(j) = mean(tempData);
    outputSD(j) = std(tempData);
end

%% Calculate sensitivity
figure, ax1 = scatter(pH,outputV,'r'); %put in mV

%least squares lines and slope calcs
hold on
h = lsline; %add least squares fit line
sens = ( h(1,1).YData(1,1) - h(1,1).YData(1,2) ) / ( h(1,1).XData(1,1) - ...
    h(1,1).XData(1,2) ); %simply take points from fit line
xlabel('pH')
ylabel('Probe Voltage')
title([ 'Sensitivity = ' sprintf('%.1f',abs(sens)) ' mV/pH'])

%calc and show r^2 of fit line

%% Calculate LOD and Repeatability
for p = 1:length(uniquePh)
    tempSD = outputSD(pH == uniquePh(p)); %get std dev's of each pH reading
    avgSD = mean(tempSD); %and average them
    LOD(p) = (3*avgSD)/abs(sens); %conc. LOD = (3 * std dev) / cal sens

    tempV = outputV(pH == uniquePh(p)); %get output voltages
    repeat(p) = (max(tempV) - min(tempV))/abs(sens); %actual repeatable range
end

avgLOD = mean(LOD);
avgRepeat = mean(repeat);

figure
plot(uniquePh,LOD)
xlabel('pH'),ylabel('pH limit')
title([ 'Average LOD = ' sprintf('%.4f',avgLOD) ' pH'])

figure
plot(uniquePh,repeat)
xlabel('pH'),ylabel('pH repeatability')
title([ 'Average repeatability = ' sprintf('%.4f',avgRepeat) ' pH'])

LOD = avgLOD; %output only one value from function, not array
repeat = avgRepeat; %output only one value from function, not array

end
```